UNIVERSITÀ DEGLI STUDI DI PADOVA

Dipartimento di Fisica e Astronomia "Galileo Galilei"

Master Degree in Physics

Final Dissertation

Development of an entangled photon source at 1550nm

Thesis supervisor:

Prof. Giuseppe Vallone

Candidate:

Andrea Pompermaier

Thesis co-supervisors:

Dr. Giulio Foletto

Dr. Lorenzo Coccia

Academic Year 2022/2023

Abstract

Entangled photon pairs play a key role in various technological applications, such as quantum communications, quantum optical computing, and quantum sensing, while also providing insights into the fundamental properties of entanglement in bipartite systems. This thesis focuses on designing, developing, and realizing a pulsed polarization-entangled photon-pair source operating at a wavelength of 1550 nm. The photons are generated through the collinear and degenerate type-II spontaneous parametric down-conversion (SPDC) process within a periodically poled potassium titanyl phosphate (PPKTP) crystal, with a Sagnac interferometer ensuring high-quality entanglement. The source has been implemented on the optical table and meticulously examined to enhance performance through a fine characterization of the optical elements while accounting for the constraints imposed by the system geometry. After the realization of the source, the focus shifted to the optimization of its performance in terms of brightness, heralding ratio, and visibility of the generated entangled states, which heavily depend on the specific optical setup configuration. To achieve this, a theoretical model of the collinear SPDC process is extended and then employed to estimate the impact of the lenses used to focus the pump beam within the crystal and to collect the 1550nm photons on the brightness and heralding ratio. Simulation results are compared with experimental data from four selected source configurations to validate the theoretical predictions.

Contents

List of Figures

List of Tables

Introduction

Entanglement remains one of the most intriguing and enigmatic aspects within the realm of quantum mechanics. This phenomenon, which emerges from the mathematical description of specific multipartite systems, gives rise to long-range correlations that cannot be classically explained without abandoning some fundamental concepts such as locality and realism. Notably, some scientists, including A. Einstein, B. Podolsky, and N. Rosen, opposed this interpretation of quantum mechanics, believing it to be incomplete. In an article of 1935 [1] they proposed a theory of quantum mechanics based on the existence of local hidden variables, able to explain the experimental results while retaining the principles of realism and locality. In 1964, J. Bell formulated Bell's theorem [2], which mathematically established the limits of theories of local hidden variables, demonstrating that certain predictions of quantum mechanics cannot be explained by any local-realistic theory. Subsequent experiments, such as those conducted by A. Aspect, J. Clauser, and A. Zeilinger in the 1980s, have provided evidence of the violation of Bell's inequalities [3,4] thus confirming the validity of quantum mechanics (for these discoveries they were awarded the 2022 Nobel Prize in Physics). Consequently, entanglement has progressively become an important research object, offering insights into the nature of quantum mechanics and also paving the way for innovative quantum technologies.

There exist several techniques to generate entangled states, each tailored to specific practical applications. One approach involves encoding quantum correlations in specific photon properties, such as their polarization state [5], the path they traverse in a medium [6], or the relationship between their energy and emission time [7]. Another avenue explores solid-state implementations in quantum hardware and quantum computers, harnessing entangled atomic energy states [8]. Polarization-entangled photon states offer wide-ranging utility across various domains, due to their compatibility with standard optical setups and ease of production. They play a pivotal role in diverse quantum communication scenarios, ranging from Quantum Key Distribution (QKD) [9–11] to teleportation [12]. These new technologies exploit the properties of entanglement to guarantee more secure communications and will be the basis for the development of the future quantum network. Furthermore, these kinds of sources assume a significant role in advancing optical quantum computers [13, 14], quantum sensors [15], and facilitating the exploration of fundamental properties of quantum mechanics.

In this thesis, I will describe the implementation of a 1550nm polarization-entangled photon source based on the collinear and degenerate type-II SPDC process in a PPKTP crystal. Specifically, I will carefully motivate the choices I made for the design of the experimental setup, the process of selecting the optical components, and I will provide an accurate description of the procedure I personally devised to assemble and characterize this source. This thesis work goes beyond the mere construction of a high-performance entangled photon source. In fact, it also includes an in-depth theoretical analysis of the SPDC process, aimed at evaluating the optimal conditions for the source. Starting from the existing literature, I have developed a comprehensive theoretical model to simulate the source's performance and compared the results with the experimental data. This enhanced comprehension of SPDC helps to optimize the source for practical applications. This work indeed marks the initial phase of a long-term research project funded by the Agenzia Spaziale Italiana (ASI) aimed at applying the source for the implementation of innovative entanglement-based protocols in quantum communications.

Although prebuilt commercial devices are available, a custom system offers greater versatility and performance. However, this requires a careful design phase to choose between various possible architectures and select items that are compatible with one another. The goals of the project allow some flexibility in the features of the source, but some are preferable, especially from the point of

view of interoperability with other components. First, the degree of freedom in which entanglement is expressed should be polarization, as it propagates very well in free space and is compatible with fiber channels. One of the most commonly employed physical processes for producing polarization-entangled photon pairs is Spontaneous Parametric Down-Conversion (SPDC). This mechanism involves the interaction of higher-energy photons, known as pump, with a nonlinear crystal possessing a strong second-order optical susceptibility $\chi^{(2)}$. The resulting photons, referred to as the signal and idler photons, exhibit distinct polarizations and are subsequently guided into an optical configuration based on Sagnac interferometer to establish entangled states. A second important consideration is the wavelength of operation. The choice is dictated by the availability (in nature and on the market) of suitable light emitters and absorbers, and by the transmittance in the optical medium used for communication. Hence, the most commonly used wavelengths in optical communications are in the 800-900 nm band, 1270-1340 nm band, and 1500-1600 nm band. For our uses, 1550 nm seems preferable as it offers the best transmittance in free-space and fibers, is less affected by solar background, and is compatible with the wealthiest selection of telecom components. Moreover, there are several devices that operate at this wavelength, motivating this choice. The third aspect is the temporal distribution of the light. Although continuous wave (CW) is a common choice especially because it allows a finer spectral distribution, pulsed operation straightforwardly provides a temporal reference which greatly simplifies the synchronization of remote devices and improves noise rejection.

In the literature, the characteristics of various sources of this kind are examined, primarily differing in terms of wavelength and the quality of the emitted entangled photon pairs, which can be achieved through diverse optical configurations. The setup that I have devised is robust and efficient, and it also allows for easy interchangeability of lens sets that determine the focusing of both the pump and emitted photon beams. This is crucial as it enhances the ability to better focus these beams within the crystal, approaching the optimal conditions as predicted by the theoretical model. The properties of the emitted entangled photons are influenced by multiple factors, including crystal type, phase-matching, momentum and energy conservation, and the configuration of the pump laser beam. All these parameters have been taken into account in the simulations I conducted to evaluate the properties of the SPDC process, which I utilized to identify the optimal source configurations.

The thesis is structured as follows. Chap. 1 provides an introduction to the essential concepts of quantum mechanics and quantum information, fundamental for the comprehension of the content of this work. In Chap. 2, the focus shifts to the SPDC process. This section aims to elucidate aspects of the source's performance, emphasizing the theoretical description of the model employed for simulating the source's behavior. Moving forward, Chap. 3 delves into the design considerations behind the source. This encompasses topics ranging from the choice of the optical setup to the selection and usage of the experimental instruments. Chap. 4 directs attention to the experimental realization of the source, detailing the methodologies employed to achieve precise alignment of the optical components. Finally, in Chap. 5, the experimental results for the chosen source configurations are presented and analyzed.

Chapter 1

Quantum Information

This chapter aims to introduce the theoretical preliminaries necessary to understand the basic working principles of the source and its applications. The theoretical framework is that of quantum information, which aims to exploit the properties of quantum mechanics to modify, store, and communicate information that is appropriately encoded in quantum states. The first concept which will be introduced is the quantum bit (qubit). In this work the quantum information is encoded in the polarization of photons. The information can be extracted with suitable quantum measurements. In particular, we will explain the experimental procedure to manipulate and measure the quantum states emitted by the source. Additionally, a general overview of the entanglement properties is presented together with an explanation of the experimental procedure employed to prove its existence in quantum states. Finally, we will present some useful methods to characterize the quality of the emitted states. The introductory concepts of quantum information presented in this chapter are taken from some textbooks of quantum mechanics and quantum optics [16–18].

1.1 Quantum States and Quantum Bits

Quantum states are described in terms of projective rays in a Hilbert space $\mathcal{H}$. In particular, using Dirac's notation, we can identify a state of the system as a ket $|\psi\rangle \in \mathcal{H}$ and its dual wavevector as a bra $\langle\psi| \in \mathcal{H}^*$. A quantum state is uniquely identified by a normalized vector in the Hilbert space, since the state $|\psi\rangle \sim c\,|\psi\rangle\ \forall c \in \mathbb{C}$. In the following, we focus on finite-dimensional systems. In particular, for any d-dimensional Hilbert space, we can define a basis $\{|0\rangle, ..., |d-1\rangle\}$ and rewrite the quantum state in terms of the basis vectors:

$$|\psi\rangle = \sum_{n=0}^{d-1} \psi_n |n\rangle \qquad\qquad \psi_n \in \mathbb{C} \tag{1.1}$$

While the dual wavevector is described as $\langle\psi| = \sum_{n=0}^{d-1} \psi_n^* \langle n|$ with ψ_n^* the complex conjugate of ψ_n. Any Hilbert space has a scalar product which is defined as follows:

$$\langle\phi|\psi\rangle = \sum_{m=0}^{d-1}\sum_{n=0}^{d-1} \phi_m^*\psi_n \langle m|n\rangle = \sum_{m=0}^{d-1}\sum_{n=0}^{d-1} \phi_m^*\psi_n\delta_{m,n} = \sum_{n=0}^{d-1} \phi_n^*\psi_n \tag{1.2}$$

A vector of unit length is usually chosen as representative of the ray $|\psi\rangle$, meaning that

$$||\psi||^2 = \langle\psi|\psi\rangle = \sum_{n=0}^{d-1} |\psi_n|^2 = 1 \tag{1.3}$$

The particular case of $d = 2$ corresponds to the two-level system also known as qubit:

$$|\psi\rangle = \alpha\,|0\rangle + \beta\,|1\rangle \qquad\qquad \alpha, \beta \in \mathbb{C} \tag{1.4}$$

Another important property of quantum mechanics is the *superposition principle* which derives from the linearity of the Hilbert space. Given two quantum states $|\psi_1\rangle$ and $|\psi_2\rangle$, any linear combination of these states is a quantum state:

$$|\Psi\rangle = c_1\,|\psi_1\rangle + c_2\,|\psi_2\rangle \in \mathcal{H} \tag{1.5}$$

1.1.1 Bloch Sphere Representation

Given a basis for a two-dimensional Hilbert space $\{|0\rangle, |1\rangle\}$, a qubit is completely represented by two complex coefficients α and β which must satisfy the normalization condition $|\alpha|^2 + |\beta|^2 = 1$. For this reason, a qubit can be parametrized in a more convenient way using only two real coefficients, satisfying the normalization condition and a relative phase factor $e^{i\phi}$ between the components $|0\rangle$ and $|1\rangle$. Another convenient parametrization for a qubit is the following:

$$|\psi\rangle = \cos\left(\frac{\theta}{2}\right)|0\rangle + e^{i\phi}\sin\left(\frac{\theta}{2}\right)|1\rangle \tag{1.6}$$

with $\theta \in [0, \pi]$ and $\phi \in [0, 2\pi]$. The qubit is represented as a point on the surface of a unit sphere called *Bloch sphere*. In this representation, a one-to-one correspondence emerges between a state $|\psi\rangle$ and the pair of angles $\{\theta, \phi\}$. Moreover, two points diametrically opposite on the surface of the Bloch sphere represent vectors that are orthogonal to each other.

In this thesis, the quantum particles are photons, and their state is encoded in their polarization. In this framework, one can arbitrarily choose two orthogonal polarization states as basis of the Hilbert space: they are conventionally denoted as $|0\rangle = |H\rangle$ and $|1\rangle = |V\rangle$. In general, a Hilbert space can be represented by an infinite number of orthonormal bases. However, given one of these bases $\{|e_j\rangle\}_{j=0,\dots,d-1}$ there exists only a finite number of orthonormal bases $\{|f_j\rangle\}_{k=0,\dots,d-1}$ which satisfy the following property:

$$|\langle e_j|f_k\rangle|^2 = \frac{1}{d} \qquad \forall j,k \in \{0,\dots,d-1\} \tag{1.7}$$

When this condition is satisfied, these bases are called *mutually unbiased*. The probability that a system is found in an element of a basis is the square of the coefficient that that element has in the state of the system (*Born rule*). When a system is prepared in one state of a mutually unbiased basis, then the measurement outcomes performed on the other bases are expected to occur with equal probability. In a two-dimension system, there exist three mutually unbiased bases, which correspond to the eigenvectors of the Pauli matrices listed below:

$$\hat{\sigma}_x = \begin{pmatrix} 0 & 1 \\ 1 & 0 \end{pmatrix} \tag{1.8}$$

$$\hat{\sigma}_y = \begin{pmatrix} 0 & -i \\ i & 0 \end{pmatrix} \tag{1.9}$$

$$\hat{\sigma}_z = \begin{pmatrix} 1 & 0 \\ 0 & -1 \end{pmatrix} \tag{1.10}$$

Conventionally, the basis of the eigenvector of $\hat{\sigma}_z$ is denoted as $\mathbb{Z} = \{|H\rangle, |V\rangle\}$, while the eigenvectors of $\hat{\sigma}_x$ and $\hat{\sigma}_y$ are denoted as $\mathbb{X} = \{|D\rangle, |A\rangle\}$ and $\mathbb{Y} = \{|R\rangle, |L\rangle\}$ [1]. These states can be represented in the $\mathbb{Z}$ basis as:

$$\begin{aligned} |D\rangle &= \frac{1}{\sqrt{2}}(|H\rangle + |V\rangle) \\ |A\rangle &= \frac{1}{\sqrt{2}}(|H\rangle - |V\rangle) \\ |R\rangle &= \frac{1}{\sqrt{2}}(|H\rangle + i|V\rangle) \\ |L\rangle &= \frac{1}{\sqrt{2}}(|H\rangle - i|V\rangle) \end{aligned} \tag{1.11}$$

[1] This notation stands for: horizontal ($|H\rangle$), vertical ($|V\rangle$), diagonal ($|D\rangle$), anti-diagonal ($|A\rangle$), right-handed ($|R\rangle$), left-handed ($|L\rangle$) polarizations.

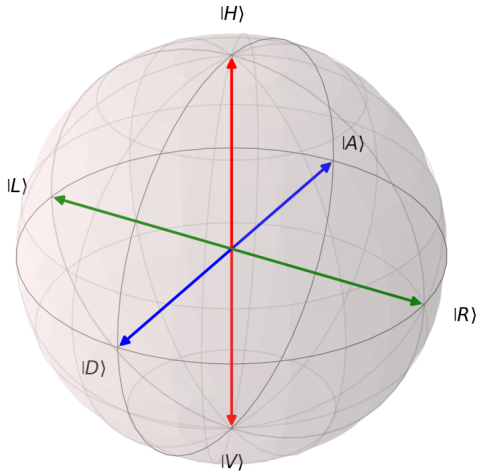

Figure 1.1: Representation on the Bloch sphere of the eigenvectors of the Pauli matrices.

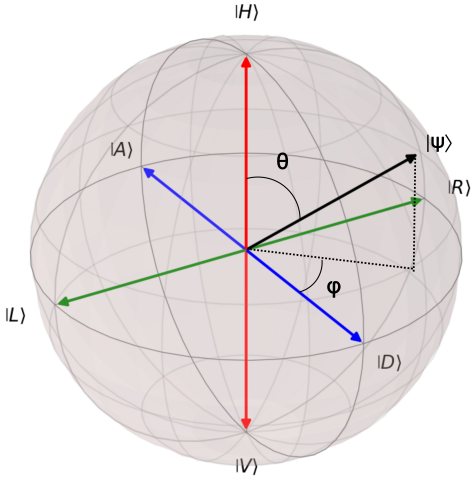

Figure 1.2: Bloch sphere representation of a qubit $|\psi\rangle$ as a function of angles θ and ϕ.

1.1.2 Density Matrix

There are situations, especially in the experimental context, where the knowledge of quantum states is incomplete. The formalism introduced to deal with these situations is that of *density matrix*. In this case, the experimentalist does not know the state of the system, but he knows that it comes from an ensemble of possible states $\{\psi_k\}_{k\in\{1,\dots,N\}}$ with probabilities $\{p_k\}_{k\in\{1,\dots,N\}}$. Thus the expression for the quantum state is the following:

$$\hat{\rho} = \sum_{k=1}^{N} p_k \left|\psi_k\right\rangle \left\langle\psi_k\right| \tag{1.12}$$

This density matrix representation of a quantum state satisfies the following three properties:

- **Hermiticity**: This property ensures that the eigenvalues of the matrix are real.

$$\hat{\rho}^\dagger = \sum_{k=1}^{N} p_k (\left|\psi_k\right\rangle \left\langle\psi_k\right|)^\dagger = \sum_{k=1}^{N} p_k \left|\psi_k\right\rangle \left\langle\psi_k\right| = \hat{\rho} \tag{1.13}$$

- **Normalization**: This condition guarantees the conservation of the total probability.

$$Tr(\hat{\rho}) = \sum_{i=0}^{d-1}\sum_{k=1}^{N} p_k \langle i|\psi_k\rangle\langle\psi_k|i\rangle = \sum_{k=1}^{N} p_k \sum_{i=0}^{d-1}\langle\psi_k|i\rangle\langle i|\psi_k\rangle = \sum_{k=1}^{N} p_k = 1 \tag{1.14}$$

  where we used the normalization condition of each state, namely $\sum_{i=0}^{d-1}\langle\psi_k|i\rangle\langle i|\psi_k\rangle = 1$ (Eq. (1.3)).

- **Non-negativity**: All eigenvalues of the density matrix are non-negative. This implies that the probabilities associated with the quantum states represented by the density matrix are always non-negative. For any state $|\psi\rangle$ we get:

$$\langle\psi|\,\hat{\rho}\,|\psi\rangle = \sum_{k=1}^{N} p_k \langle\psi|\psi_k\rangle\langle\psi_k|\psi\rangle = \sum_{k=1}^{N} p_k \Psi_k^* \Psi_k \geq 0 \tag{1.15}$$

  with $\Psi_k = \langle\psi_k|\psi\rangle \in \mathbb{C}$.

This representation of a quantum state is a generalization of that introduced in the previous section and it becomes crucial to treat the generalized evolution of a mixed state. The density matrix

formalism can be used also to describe a pure state. In this case, the whole definition of Eq. (1.12) reduces to a projector $\hat{\rho} = |\psi\rangle \langle\psi|$.

A general representation for the density matrix of a qubit system is given by:

$$\hat{\rho} = \frac{1}{2}(\mathbb{I} + \vec{r} \cdot \vec{\sigma}) = \frac{1}{2}(\mathbb{I} + r_x\hat{\sigma}_x + r_y\hat{\sigma}_y + r_z\hat{\sigma}_z) \tag{1.16}$$

with $\vec{r} \in \mathbb{R}^3$, $||\vec{r}|| \leq 1$. In the particular case of a pure state, this representation directly derives from the calculation of $\hat{\rho} = |\psi\rangle \langle\psi|$ using the representation of the qubit $|\psi\rangle$ in a Bloch sphere (Eq. (1.6)) with:

$$\vec{r} = \begin{pmatrix} \sin\theta\cos\phi \\ \sin\theta\sin\phi \\ \cos\theta \end{pmatrix} \tag{1.17}$$

We can see a correspondence between a point on the surface of the Bloch sphere, represented by the vector $\vec{r}$ and a pure state. For a mixed state the interpretation of Eq. (1.16) is the same: in this case, however, the state is represented as a vector $\vec{r}$ with $||\vec{r}|| \leq 1$ (inside the Bloch sphere).

$$\vec{r} = \begin{pmatrix} Tr(\hat{\rho}\hat{\sigma}_x) \\ Tr(\hat{\rho}\hat{\sigma}_y) \\ Tr(\hat{\rho}\hat{\sigma}_z) \end{pmatrix} \tag{1.18}$$

which directly comes from the definition of density matrix provided in Eq. (1.16), together with the properties of the Pauli matrices: $Tr(\hat{\sigma}_i^2) = 2$, $Tr(\hat{\sigma}_i) = Tr(\hat{\sigma}_i\hat{\sigma}_j) = 0$ with $i, j \in \{x, y, z\}$ and $i \neq j$. The state $\hat{\rho} = \frac{\mathbb{I}}{2}$ is called a maximally mixed state and it can be represented as a point at the center of the Bloch sphere.

1.2 Evolution of Quantum States

The quantum state of a system can evolve in time due to interactions with a potential, other systems or the environment. The evolution of a quantum state was firstly described by E. Schrödinger, with the famous equation [19]:

$$i\hbar\frac{\partial}{\partial t}|\psi(t)\rangle = \hat{H}|\psi(t)\rangle \tag{1.19}$$

where $\hat{H}$ is the Hamiltonian describing the interaction of the system. This equation predicts the time evolution of a pure state:

$$|\psi(t)\rangle = e^{-\frac{i}{\hbar}\hat{H}t}|\psi(0)\rangle \tag{1.20}$$

More generally, in quantum mechanics the evolution of pure states is described in terms of *unitary operators* $\hat{U}$: $|\psi\rangle \longrightarrow \hat{U}|\psi\rangle = |\psi'\rangle$. This kind of transformations, indeed, maps quantum states to other quantum states, preserving the scalar product:

$$\langle\phi'|\psi'\rangle = \langle\phi|\hat{U}^\dagger\hat{U}|\psi\rangle = \langle\phi|\psi\rangle \tag{1.21}$$

Using the density matrix formalism, we have a wider scenario of possible transformations. A unitary transformation can be applied to all the states of the ensemble:

$$\hat{\rho} = \sum_{k=1}^{N} p_k |\psi_k\rangle \langle\psi_k| \longrightarrow \hat{\rho}' = \sum_{k=1}^{N} p_k\hat{U}|\psi_k\rangle \langle\psi_k|\hat{U}^\dagger = \hat{U}\hat{\rho}\hat{U}^\dagger \tag{1.22}$$

This formalism has the advantage of treating more general kind of state evolution, including non-isolated systems that can interact with the environment. In this case, we need to introduce some new operators called *superoperators* $\mathcal{E}$ which represent a transformation between operators:

$$\hat{\rho} \longrightarrow \hat{\rho}' = \mathcal{E}(\hat{\rho}) \tag{1.23}$$

which satisfy the following properties:

- **Linearity**: Superoperators are linear maps, meaning the linear combination of density matrices is mapped to the linear combination of their transformed $\mathcal{E}(\alpha\hat{\rho}_1 + \beta\hat{\rho}_2) = \alpha\mathcal{E}(\hat{\rho}_1) + \beta\mathcal{E}(\hat{\rho}_2)$, $\alpha, \beta \in \mathbb{C}$;
- **Preserve trace**: A trace-preserving superoperator preserves the trace of a density matrix. This is necessary because density matrices have unit trace. $Tr[\hat{\rho}] = Tr[\mathcal{E}(\hat{\rho})]$;
- **Preserve hermiticity**: They preserve the hermiticity of a density matrix, thus allowing to map a density matrix to another density matrix. If $\hat{\rho} = \hat{\rho}^\dagger \longrightarrow \mathcal{E}(\hat{\rho}) = \mathcal{E}(\hat{\rho})^\dagger$;
- **Completely positive**: This includes the case of positivity if $\hat{\rho} \geq 0$ then $\mathcal{E}(\hat{\rho}) \geq 0$. Moreover, a completely positive superoperator ensures that when applied to a composite system consisting of a principal system $\mathcal{H}$ and an ancillary system $\mathcal{H}_{env}$, such that the map acts locally on the system leaving unchanged the state of the environment, this is a positive map: if $\hat{\rho} \geq 0$ is defined in $\mathcal{H}$, then the map $(\mathcal{E} \otimes \mathbb{I})(\hat{\rho}) \geq 0$.

It is possible to show that every superoperator which satisfies the properties listed above can be written in Kraus representation [20] as a sum of N terms:

$$\mathcal{E} : \hat{\rho} \to \hat{\rho}' = \mathcal{E}(\hat{\rho}) = \sum_{n=1}^{N} \hat{K}_n \hat{\rho} \hat{K}_n^\dagger \tag{1.24}$$

with the condition $\sum_{n=1}^{N} \hat{K}_n^\dagger \hat{K}_n = \mathbb{I}$. The operators $\{\hat{K}_n\}_{n=1,\dots,N}$ are called Kraus operators. These kinds of transformations are called *generalized evolutions*. The particular case in which there is only one Kraus operator corresponds to the unitary transformation (indeed in this case it must satisfy the condition $\hat{K}^\dagger \hat{K} = \mathbb{I}$).

From an experimental point of view, we need to manipulate the quantum state of a photon, through rotations on the Bloch sphere (which are unitary transformations). However, the experimental setups are not ideal and can introduce distortions and losses of the produced states: such transformations can be effectively treated as generalized evolutions.

1.3 Quantum Measurements

Quantum measurements are fundamental operations in quantum mechanics that allow us to extract information about a quantum system. A quantum measurement involves interacting with a quantum system and obtaining a result. In quantum mechanics, a measurement is described by a collection of operators $\{\hat{M}_i\}$, which map the state of the system $|\psi\rangle$ into various possible states $|\psi_i\rangle$. When a measure is performed the probability of each outcome is given by:

$$p_i = \langle\psi|\hat{M}_i^\dagger \hat{M}_i|\psi\rangle = Tr(\hat{M}_i^\dagger \hat{M}_i \hat{\rho}) \tag{1.25}$$

It is important to note that quantum measurements are inherently probabilistic. In general, the outcome of a measurement cannot be predicted with certainty and the probabilities of obtaining different outcomes are determined by the quantum state of the system prior to the measurement. For probability conservation we need to impose also the condition:

$$\sum_{n=1}^{N} p_n = 1 \longleftrightarrow \sum_{n=1}^{N} \hat{M}_n^\dagger \hat{M}_n = \mathbb{I} \tag{1.26}$$

After the measurement, the state of the system collapses to the i-th outcome obtaining

$$\hat{\rho} \to \hat{\rho}' = \frac{\hat{M}_i \hat{\rho} \hat{M}_i^\dagger}{pi} \tag{1.27}$$

In the particular case in which the operators $\{\hat{M}_i\}$ are projectors $\{\hat{\Pi}_i\}$, namely self-adjoint ($\hat{\Pi}_i = \hat{\Pi}_i^\dagger$), idempotent ($\hat{\Pi}_i^2 = \hat{\Pi}_i$), and orthogonal[2] we find the so called *projective measurements*. In this case,

[2]Two projectors are orthogonal when the subspaces onto which they project are mutually perpendicular.

the measurement is described with a hermitian operator $\hat{O}$, called *observable*. We can think of this operator, at least for finite dimension systems, as a matrix. To better understand how it works, we can rewrite it in terms of its spectral decomposition (which is always admitted since it is assumed to be hermitian).

$$\hat{O} = \sum_{i=0}^{d-1} \lambda_i |\lambda_i\rangle \langle\lambda_i| = \sum_{i=0}^{d-1} \lambda_i \hat{\Pi}_i \tag{1.28}$$

where $\lambda_i \in \mathbb{R}$ is the i-th eigenvalue corresponding to the eigenvector $|\lambda_i\rangle$. The eigenvalues are the possible outcomes of the measurements. The probability of getting the outcome λ_i is given by:

$$p_i = \langle\psi|\hat{\Pi}_i|\psi\rangle \tag{1.29}$$

or, using the density matrix formalism,

$$p_i = Tr(\hat{\Pi}_i\hat{\rho}) \tag{1.30}$$

Another important quantity, strictly related to the experimental measurement, is the expectation value of an observable evaluated for a state $|\psi\rangle$:

$$\langle\hat{O}\rangle = \langle\psi|\hat{O}|\psi\rangle = \sum_{n=0}^{d-1} \lambda_n \langle\psi|\lambda_n\rangle\langle\lambda_n|\psi\rangle \tag{1.31}$$

More in general, with the formalism of density matrix, we have

$$\langle\hat{O}\rangle = Tr(\hat{\rho}\hat{O}) \tag{1.32}$$

The role of the measurements is that of extracting information from a system. The state of a system living in a Hilbert space $\mathcal{H}$ can be fully characterized by certain observables. In the two-dimensional case, a qubit can be always written in terms of the eigenvectors of one of three Pauli matrices. Typically, a qubit is written in terms of the states $|H\rangle$ and $|V\rangle$ (eigenstates of $\hat{\sigma}_z$). Moreover, every observable in a two-dimensional Hilbert space $\mathcal{H}$ can be written in terms of the Pauli matrices:

$$\hat{O} = \gamma_0\mathbb{I} + \vec{\gamma}\cdot\vec{\sigma} \qquad\qquad \gamma_0, \gamma_1, \gamma_2, \gamma_3 \in \mathbb{R} \tag{1.33}$$

Each Pauli matrix represents an observable, which can be decomposed using their spectral decomposition (see Eq. (1.28)) as follows:

$$\begin{aligned} \hat{\sigma}_x &= |D\rangle\langle D| - |A\rangle\langle A| = \hat{\Pi}_D - \hat{\Pi}_A \\ \hat{\sigma}_y &= |R\rangle\langle R| - |L\rangle\langle L| = \hat{\Pi}_R - \hat{\Pi}_L \\ \hat{\sigma}_z &= |H\rangle\langle H| - |V\rangle\langle V| = \hat{\Pi}_H - \hat{\Pi}_V \end{aligned} \tag{1.34}$$

with the definitions of the states $\{|H\rangle, |V\rangle, |D\rangle, |A\rangle, |R\rangle, |L\rangle\}$ given in Eq. (1.11). From now on, we will indicate as measurements on bases $\{\mathbb{X}, \mathbb{Y}, \mathbb{Z}\}$ the measurements performed on the relative observables[3], represented by the corresponding Pauli matrices $\{\hat{\sigma}_x, \hat{\sigma}_y, \hat{\sigma}_z\}$.

1.3.1 Experimental Polarization Projective Measurements

Projective measurements of polarization are widely used in quantum optics because they provide a direct and simple way to extract information about the polarization state of a quantum system. A common instrument employed to perform projective measurements of the polarization of a photon is the polarizing beam splitter (PBS), which is an optical device that separates a beam of light into two components with different polarizations: the transmitted light is horizontally polarized, while the reflected is vertically polarized. This instrument provides a projective measurement on the $\mathbb{Z}$-basis. Given a quantum state $|\psi\rangle = \alpha|H\rangle + \beta|V\rangle$, if the photon is transmitted, it is projected in the state

[3] In quantum information, we often refer to measurement on a basis as a measurement on the corresponding observable. This correspondence is valid when the observable has fixed eigenvalues and all the projectors in the spectral decomposition have rank 1. This is the case of the Pauli matrices.

$|H\rangle$, while in the case of reflection, the final state is $|V\rangle$: the corresponding probabilities are $|\alpha|^2$ and $|\beta|^2$ respectively.

Two fundamental instruments employed for manipulating the polarization state of photons are the quarter-wave plate (QWP) and half-wave plate (HWP) which both belong to a category of optical devices known as retardation plates. These devices are designed to alter the polarization state of light by introducing a phase delay between two orthogonal polarization components. A QWP is designed to introduce a phase difference of one-quarter wavelength between the two orthogonal polarization components of the incident light, while for the HWP this retardation is of half a wavelength.

The action of a retardation waveplate can be described in terms of a unitary operator. Assuming the fast axis to be parallel to the $|H\rangle$ component (which now corresponds to the zero of the waveplate), the matrix describing the effect of the waveplate, using Jones calculus, becomes:

$$\hat{\mathcal{S}}_{\mathcal{WP}}(\delta) = \begin{pmatrix} 1 & 0 \\ 0 & e^{-i\delta} \end{pmatrix} \tag{1.35}$$

In the case of a quarter-wave plate (QWP) $\delta = \frac{\pi}{2}$, while for a half-wave plate (HWP) it becomes $\delta = \pi$. If the fast axis is rotated of an angle θ the action of the waveplate can be derived by applying the rotation matrix:

$$\hat{R}(\theta) = \begin{pmatrix} \cos\theta & -\sin\theta \\ \sin\theta & \cos\theta \end{pmatrix} \tag{1.36}$$

And the corresponding waveplate acts on the state with a transformation described by the unitary operator:

$$\hat{\mathcal{U}}_{\mathcal{WP}}(\theta,\delta) = \hat{R}(\theta)\hat{\mathcal{S}}_{\mathcal{WP}}(\delta)\hat{R}^T(\theta) = \begin{pmatrix} \cos^2\theta + e^{-i\delta}\sin^2\theta & (1-e^{-i\delta})\cos\theta\sin\theta \\ (1-e^{-i\delta})\cos\theta\sin\theta & e^{-i\delta}\cos^2\theta + \sin^2\theta \end{pmatrix} \tag{1.37}$$

With a proper combination of the retardation waveplates and a PBS it is possible to perform projective measurements in the bases $\{\mathbb{X}, \mathbb{Y}, \mathbb{Z}\}$.

Measure in $\mathbb{Z}$-basis

A PBS can be used as a device that projects the state of the photon on $|H\rangle$ or $|V\rangle$. If we place two detectors at the output branches of the PBS we are able to understand what the outcome of the measurement is depending on which of the two detectors has revealed the photon.

Mathematically, a projection on the state $|H\rangle$ is described by

$$\hat{\Pi}_H = |H\rangle\langle H| = \begin{pmatrix} 1 & 0 \\ 0 & 0 \end{pmatrix} \tag{1.38}$$

which corresponds to the transformation induced by the PBS on the transmitted branch. Equivalently, one can place a detector on the reflected path. In this case, the quantum state of the system is projected on $|V\rangle$. The corresponding transformation is given by the projector

$$\hat{\Pi}_V = |V\rangle\langle V| = \begin{pmatrix} 0 & 0 \\ 0 & 1 \end{pmatrix} \tag{1.39}$$

Alternatively, it is possible to use only one detector positioned, for example, on the transmitted path of the PBS. The same projection on $|V\rangle$ is achieved by positioning before the PBS a HWP rotated of $\theta = \frac{\pi}{4}$, indeed the corresponding transformation is:

$$\hat{\mathcal{S}}_V = \hat{\Pi}_H\hat{\mathcal{U}}_{\mathcal{WP}}(\frac{\pi}{4},\pi) = \begin{pmatrix} 0 & 1 \\ 0 & 0 \end{pmatrix} \tag{1.40}$$

The probability of detecting a photon following this transformation is the same that would be obtained by applying the projector $\hat{\Pi}_V$, since $Tr(\hat{\mathcal{S}}_V\hat{\rho}\hat{\mathcal{S}}_V^\dagger) = Tr(\hat{\Pi}_V\hat{\rho})$.

Measure in $\mathbb{X}$-basis

The sole PBS allows to perform measurements in the $\mathbb{Z}$-basis. However, with a HWP positioned before the PBS, it is possible to perform projective measurements also in the $\mathbb{X}$-basis. The projectors of this basis are:

$$\hat{\Pi}_D = |D\rangle\langle D| = \frac{1}{2}\begin{pmatrix}1 & 1\\ 1 & 1\end{pmatrix} \tag{1.41}$$

$$\hat{\Pi}_A = |A\rangle\langle A| = \frac{1}{2}\begin{pmatrix}1 & -1\\ -1 & 1\end{pmatrix} \tag{1.42}$$

These transformations can be achieved by setting the HWP at $\theta = \frac{\pi}{8}$ and using two detectors. The transformation induced on the transmitted path is:

$$\hat{\mathcal{S}}_D = \hat{\Pi}_H \hat{\mathcal{U}}_{\mathcal{WP}}(\frac{\pi}{8}, \pi) = \frac{1}{\sqrt{2}}\begin{pmatrix}1 & 1\\ 0 & 0\end{pmatrix} \tag{1.43}$$

and on the reflected one is

$$\hat{\mathcal{S}}_A = \hat{\Pi}_V \hat{\mathcal{U}}_{\mathcal{WP}}(\frac{\pi}{8}, \pi) = \frac{1}{\sqrt{2}}\begin{pmatrix}0 & 0\\ 1 & -1\end{pmatrix} \tag{1.44}$$

In this case we have that $Tr(\hat{\mathcal{S}}_D\hat{\rho}\hat{\mathcal{S}}_D^\dagger) = Tr(\hat{\Pi}_D\hat{\rho})$ and $Tr(\hat{\mathcal{S}}_A\hat{\rho}\hat{\mathcal{S}}_A^\dagger) = Tr(\hat{\Pi}_A\hat{\rho})$. In a similar way, if we use only one detector we need to set two angles for the HWP. For $\theta = \frac{\pi}{8}$ we get the projection on $|D\rangle$, while the projection on $|A\rangle$ in this case is obtained setting $\theta = \frac{3\pi}{8}$:

$$\hat{\mathcal{S}}'_A = \hat{\Pi}_H \hat{\mathcal{U}}_{\mathcal{WP}}(\frac{3\pi}{8}, \pi) = \frac{1}{\sqrt{2}}\begin{pmatrix}-1 & 1\\ 0 & 0\end{pmatrix} \tag{1.45}$$

with $Tr(\hat{\mathcal{S}}'_A\hat{\rho}\hat{\mathcal{S}}'^\dagger_A) = Tr(\hat{\Pi}_A\hat{\rho})$.

Measure in $\mathbb{Y}$-basis

To perform measurements in the $\mathbb{Y}$-basis we need to add a QWP before the HWP of the previous configuration. In this case, the two projectors are:

$$\hat{\Pi}_R = |R\rangle\langle R| = \frac{1}{2}\begin{pmatrix}1 & -i\\ i & 1\end{pmatrix} \tag{1.46}$$

$$\hat{\Pi}_L = |L\rangle\langle L| = \frac{1}{2}\begin{pmatrix}1 & i\\ -i & 1\end{pmatrix} \tag{1.47}$$

If we have two detectors it is sufficient to set the angle of the HWP to $\theta = \frac{\pi}{4}$ and the angle of the QWP to $\phi = \frac{\pi}{4}$. We obtain the following transformations for the transmitted and reflected paths respectively:

$$\hat{\mathcal{S}}_R = \hat{\Pi}_H \hat{\mathcal{U}}_{\mathcal{WP}}(\frac{\pi}{4}, \pi)\hat{\mathcal{U}}_{\mathcal{WP}}(\frac{\pi}{4}, \frac{\pi}{2}) = \frac{1}{2}\begin{pmatrix}1+i & 1-i\\ 0 & 0\end{pmatrix} \tag{1.48}$$

$$\hat{\mathcal{S}}_L = \hat{\Pi}_V \hat{\mathcal{U}}_{\mathcal{WP}}(\frac{\pi}{4}, \pi)\hat{\mathcal{U}}_{\mathcal{WP}}(\frac{\pi}{4}, \frac{\pi}{2}) = \frac{1}{2}\begin{pmatrix}0 & 0\\ 1-i & 1+i\end{pmatrix} \tag{1.49}$$

In this case we have that $Tr(\hat{\mathcal{S}}_R\hat{\rho}\hat{\mathcal{S}}_R^\dagger) = Tr(\hat{\Pi}_R\hat{\rho})$ and $Tr(\hat{\mathcal{S}}_L\hat{\rho}\hat{\mathcal{S}}_L^\dagger) = Tr(\hat{\Pi}_L\hat{\rho})$. Equivalently, we can use just one detector positioned on the transmitted path. In this case, the projection on the state $|L\rangle$ is achieved by setting the angle of the QWP to $\phi = \frac{3\pi}{4}$:

$$\hat{\mathcal{S}}'_L = \hat{\Pi}_H \hat{\mathcal{U}}_{\mathcal{WP}}(\frac{\pi}{4}, \pi)\hat{\mathcal{U}}_{\mathcal{WP}}(\frac{3\pi}{4}, \frac{\pi}{2}) = \frac{1}{2}\begin{pmatrix}-1-i & 1-i\\ 0 & 0\end{pmatrix} \tag{1.50}$$

with $Tr(\hat{\mathcal{S}}'_L\hat{\rho}\hat{\mathcal{S}}'^\dagger_L) = Tr(\hat{\Pi}_L\hat{\rho})$.

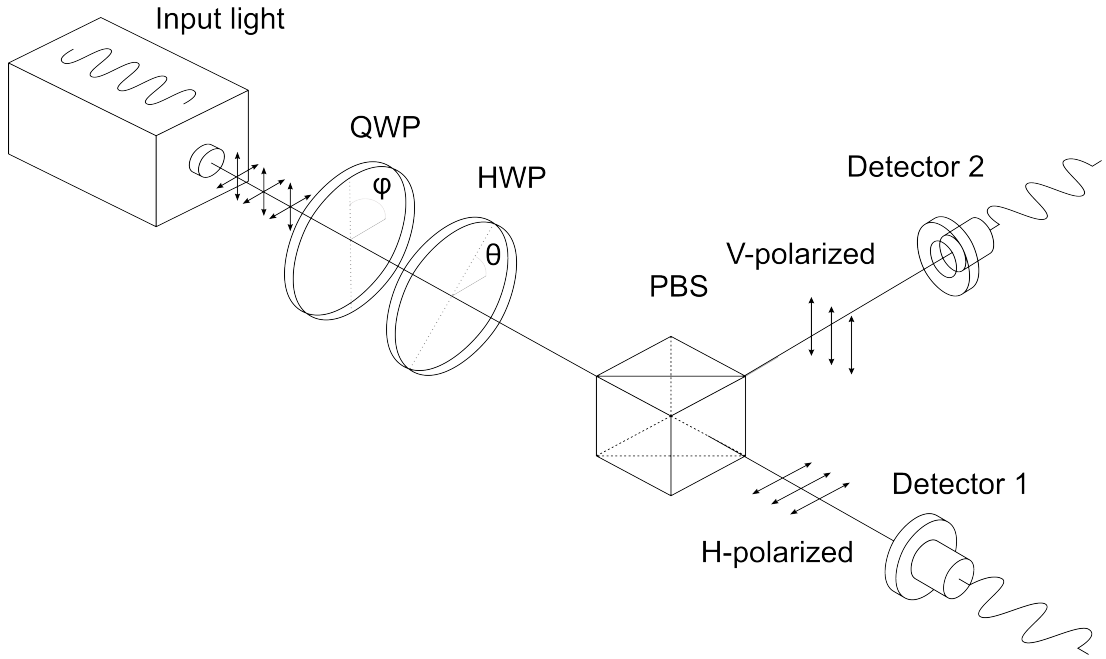

Figure 1.3: Scheme of the measurement of a photon polarization [21].

1.4 Entanglement

So far, we have considered only the case of an isolated system defined on a given Hilbert space $\mathcal{H}$. We can generalize the previous formalism to multipartite systems. The simplest case is a bipartite system, composed of two spaces $\mathcal{H}_A$ and $\mathcal{H}_B$. We choose the orthonormal bases $\{|0\rangle_A, |1\rangle_A, ..., |d_A - 1\rangle_A\}$ for $\mathcal{H}_A$ and $\{|0\rangle_B, |1\rangle_B, ..., |d_B - 1\rangle_B\}$ for $\mathcal{H}_B$. The Hilbert space of the bipartite system is given by the tensor product of the two subsystems $\mathcal{H} = \mathcal{H}_A \otimes \mathcal{H}_B$ and a pure state can be defined on this space as

$$|\psi\rangle_{AB} = \sum_{a=0}^{d_A-1} \sum_{b=0}^{d_B-1} \psi_{ab} |a\rangle_A \otimes |b\rangle_B \tag{1.51}$$

with ψ_{ab} complex coefficients. In the following, we will equivalently denote the tensor product of two states as $|a\rangle_A \otimes |b\rangle_B = |a\rangle_A |b\rangle_B = |ab\rangle_{AB}$.

In the composite Hilbert space, we have operators defined on $\mathcal{H}$. Local operators acting on the two subsystems are written in terms of $\hat{O} = \hat{A} \otimes \hat{B}$. If these operators act as $\hat{A} |a\rangle_A = |\alpha\rangle_A$ and $\hat{B} |b\rangle_B = |\beta\rangle_B$, the action of $\hat{O}$ on the state $|\psi\rangle_{AB}$ of Eq. (1.51) becomes:

$$\hat{O} |\psi\rangle_{AB} = \sum_{a=0}^{d_A-1} \sum_{b=0}^{d_B-1} \psi_{ab} \hat{A} |a\rangle_A \otimes \hat{B} |b\rangle_B = \sum_{a=0}^{d_A-1} \sum_{b=0}^{d_B-1} \psi_{ab} |\alpha\rangle_A \otimes |\beta\rangle_B \tag{1.52}$$

Pure states defined in a composite Hilbert space $\mathcal{H}$ that can be written as the tensor product of two states $|\psi_a\rangle_A$ and $|\psi_b\rangle_B$ defined in $\mathcal{H}_A$ and $\mathcal{H}_B$ respectively are said to be *separable states*. Mathematically, a pure separable state is expressed as $|\phi\rangle_{AB} = |\psi_a\rangle_A \otimes |\psi_b\rangle_B$. In this case, a local operator acting on one of the two subsystems doesn't affect the other subsystem.

However, most of the states defined on $\mathcal{H}$ do not satisfy this property: these states are said to be *entangled*. These states behave differently from the separable states since local operations can change the state of the whole system giving long-range correlations that cannot be classically explained. A crucial point is to distinguish the separable states from the entangled ones. In bipartite systems, we

can employ the *Schmidt decomposition*. Let $\mathcal{H}_A$ and $\mathcal{H}_B$ two Hilbert spaces of dimension d_A and d_B respectively. For any state $|\psi\rangle_{AB}$ defined on the composite Hilbert space $\mathcal{H}_A \otimes \mathcal{H}_B$ there exist a set of orthonormal bases $\{|v_1\rangle_A, ..., |v_{d_A}\rangle_A\} \in \mathcal{H}_A$ and $\{|w_1\rangle_B, ..., |w_{d_B}\rangle_B\} \in \mathcal{H}_B$ such that

$$|\psi\rangle_{AB} = \sum_{i=1}^{k} \sqrt{\lambda_i} |v_i\rangle_A |w_i\rangle_B \qquad \sum_{i=1}^{k} \lambda_i = 1 \tag{1.53}$$

where $k \leq \min\{d_A, d_B\}$ is called *Schmidt rank*. If $k = 1$ the state is separable, otherwise it is entangled. The scalars λ_i are positive and unique up to re-ordering and they correspond to the eigenvalues of the reduced density matrix, obtained by the partial trace of the state $\hat{\rho}_{AB} = |\psi\rangle \langle\psi|_{AB}$:

$$\begin{aligned} \hat{\rho}_A &= Tr_B \hat{\rho}_{AB} = \sum_{i=1}^{k} \lambda_i |v_i\rangle \langle v_i| \\ \hat{\rho}_B &= Tr_A \hat{\rho}_{AB} = \sum_{i=1}^{k} \lambda_i |w_i\rangle \langle w_i| \end{aligned} \tag{1.54}$$

Given a quantum state $|\psi\rangle_{AB}$ one can evaluate the eigenvalues of the reduced density matrix of one of the two subsystems. In this way, it is possible to distinguish a separable state from an entangled one.

If we have an entangled state, it means that we have a non-separable superposition of multipartite states in such a way that their states become interdependent. The interesting aspect is that once entangled, the state of one particle is correlated with the state of the others in such a way that if an observer measures one particle, the state with which that observer describes the other particles changes instantaneously. For instance, if a system is described by $|\psi\rangle_{AB}$ like in Eq. (1.53), and Alice measures it to find her subsystem in $|v_i\rangle_A$, she instantly knows that Bob's state will be found in $|w_i\rangle_B$.

1.4.1 Bell Inequalities

The fact that a measurement of a system can instantaneously change the state of a remote one has been subject of debate. Some scientists, including Einstein, Podolsky, and Rosen, found this interpretation of quantum mechanics unacceptable, considering the theory to be incomplete: the famous Einstein-Podolsky-Rosen (EPR) paradox [1]. They suggest the existence of additional, unknown properties or variables that determine the outcomes of quantum measurements. These hidden variables would provide a more complete description of the quantum state and its behavior than what is allowed by the standard formalism of quantum mechanics. Besides the different interpretations of the entanglement, the main problem was the experimental verification of these theories. In 1964, J. Bell introduced an inequality, famously known as *Bell's inequality*, which relates the results of specific measurements conducted on an entangled state. Bell's inequality allows to distinguish the predictions of quantum mechanics from those of any hidden-variables theory. In the experiment proposed by Bell, two particles are prepared in an entangled state and then separated, such that each particle is sent to a different observer who can perform measurements on their respective particles. Bell's inequality examines the statistical correlations between the measurement outcomes of the two observers. It compares the correlations predicted by quantum mechanics with those that would be expected from hidden-variable theories. If the experimental results violate Bell's inequality, the observed correlations between the entangled particles cannot be explained by classical theories that obey the principles of locality and realism. These violations, which have been observed in numerous experiments, manifest the property known as quantum nonlocality, which shows the failure of classical theories to explain quantum phenomena and provides strong evidence for the existence of entanglement.

A famous formulation of Bell's inequality is that provided by J.F. Clauser, M.A. Horne, A. Shimony, and R.A. Holt in 1969, known as CHSH inequality [22], valid in the case of bipartite systems. The objective is to define a quantity, experimentally accessible, that assumes different values depending if the system is classical or quantistic. Now we provide a description of this experiment. We have a two-particle system and we send each particle to a different experimentalist physically separated, let's call them Alice and Bob. We assume that Alice and Bob can perform only two possible measurements,

denoted as $x, y \in \{0, 1\}$ with outcomes that can assume the values $a, b \in \{-1, +1\}$, We define the following experimental quantity:

$$S = \langle a_0 b_0 \rangle + \langle a_0 b_1 \rangle + \langle a_1 b_0 \rangle - \langle a_1 b_1 \rangle \tag{1.55}$$

with $\langle a_x b_y \rangle = \sum_{a,b} abp(ab|xy)$. The prediction of quantum mechanics can be different from that predicted by the hidden variable theory. Now we provide more details about the different predictions of the two theories, which is the key point to verify the non-locality of quantum mechanics.

The principle of locality suggests that we should be capable of identifying a specific collection of past factors, represented by variables λ, that have a combined causal impact on both outcomes, a and b [23].

$$p(ab|xy, \lambda) = p(a|x, \lambda)p(b|y, \lambda) \tag{1.56}$$

With this condition, we state that the probability of the outcome a depends only on the past variable λ but not on long-distance measurements. The hidden variable λ may change from one experiment to another, and we can write it in terms of a distribution probability $q(\lambda)$:

$$p(ab|xy) = \int_\Lambda d\lambda q(\lambda) p(a|x, \lambda) p(b|y, \lambda) \tag{1.57}$$

If the probabilities $p(ab|xy)$ satisfy the locality condition stated in Eq. (1.57), then we have that $S \leq 2$, which is the CHSH inequality. This can be simply proved using the definition of local theory previously stated. Indeed, the expectation values of the possible measurements performed on the system become:

$$\begin{aligned} \langle a_x b_y \rangle &= \sum_{a,b} \int_\Lambda d\lambda q(\lambda) p(a|x, \lambda) p(b|y, \lambda) ab = \\ &= \int_\Lambda d\lambda q(\lambda) \sum_a a p(a|x, \lambda) \sum_b b p(b|y, \lambda) = \int_\Lambda d\lambda q(\lambda) \langle a_x \rangle_\lambda \langle b_y \rangle_\lambda \end{aligned} \tag{1.58}$$

We can write $S = \int_\Lambda d\lambda q(\lambda) S_\lambda$, where:

$$S_\lambda = \langle a_0 \rangle_\lambda \langle b_0 \rangle_\lambda + \langle a_0 \rangle_\lambda \langle b_1 \rangle_\lambda + \langle a_1 \rangle_\lambda \langle b_0 \rangle_\lambda - \langle a_1 \rangle_\lambda \langle b_1 \rangle_\lambda \tag{1.59}$$

Since $\langle a_0 \rangle_\lambda, \langle a_1 \rangle_\lambda \in [-1, +1]$, the following inequality is always satisfied:

$$S_\lambda \leq |\langle b_0 \rangle_\lambda + \langle b_1 \rangle_\lambda| + |\langle b_0 \rangle_\lambda - \langle b_1 \rangle_\lambda| \leq 2 \tag{1.60}$$

and finally we get that $S = \int_\Lambda d\lambda q(\lambda) S_\lambda \leq 2$ since for normalization $\int_\Lambda d\lambda q(\lambda) = 1$. The formalism of quantum mechanics predicts the existence of entangled states which violate the CHSH inequality providing a maximum value for S of $2\sqrt{2}$ (Cirel'son's bound [24]). There are only four states, in the bipartite scenario, which maximally violate the CHSH inequality and they are called Bell states:

$$\begin{aligned} \left|\Phi^+\right\rangle &= \frac{1}{\sqrt{2}}(|HH\rangle + |VV\rangle) \\ \left|\Phi^-\right\rangle &= \frac{1}{\sqrt{2}}(|HH\rangle - |VV\rangle) \\ \left|\Psi^+\right\rangle &= \frac{1}{\sqrt{2}}(|HV\rangle + |VH\rangle) \\ \left|\Psi^-\right\rangle &= \frac{1}{\sqrt{2}}(|HV\rangle - |VH\rangle) \end{aligned} \tag{1.61}$$

To verify this, we need to use the formalism of quantum mechanics to calculate S. In this case, the observables are written in terms of operators $\hat{A}_x$ and $\hat{B}_y$, which represent local measurements on the bipartite state. In this framework, S becomes an operator, expressed in the following way:

$$\hat{S} = (\hat{A}_0 + \hat{A}_1) \otimes \hat{B}_0 + (\hat{A}_0 - \hat{A}_1) \otimes \hat{B}_1 \tag{1.62}$$

The experimentally accessible value is the expectation value of $\hat{S}$:

$$S = \langle \hat{S} \rangle = \langle \hat{A}_0 \otimes \hat{B}_0 \rangle + \langle \hat{A}_1 \otimes \hat{B}_0 \rangle + \langle \hat{A}_0 \otimes \hat{B}_1 \rangle - \langle \hat{A}_1 \otimes \hat{B}_1 \rangle \tag{1.63}$$

To achieve the maximum violation we need to choose as local measurements certain anticommuting observables ($\{\hat{A}_0, \hat{A}_1\} = \{\hat{B}_0, \hat{B}_1\} = 0$). More specifically, a particular choice is:

$$\begin{aligned} \hat{A}_0 &= \hat{\sigma}_z \\ \hat{A}_1 &= \hat{\sigma}_x \\ \hat{B}_0 &= \frac{\hat{\sigma}_z + \hat{\sigma}_x}{\sqrt{2}} \\ \hat{B}_1 &= \frac{\hat{\sigma}_z - \hat{\sigma}_x}{\sqrt{2}} \end{aligned} \tag{1.64}$$

In this case, it is trivial to verify that the value of S for $|\phi^+\rangle$ is equal to $S = 2\sqrt{2}$. The operators acting on the composite system are:

$$\begin{aligned} \langle \hat{A}_0 \otimes \hat{B}_0 \rangle &= \frac{1}{\sqrt{2}} \begin{pmatrix} 1 & 1 & 0 & 0 \\ 1 & -1 & 0 & 0 \\ 0 & 0 & -1 & -1 \\ 0 & 0 & -1 & 1 \end{pmatrix} \\ \langle \hat{A}_0 \otimes \hat{B}_1 \rangle &= \frac{1}{\sqrt{2}} \begin{pmatrix} 1 & -1 & 0 & 0 \\ -1 & -1 & 0 & 0 \\ 0 & 0 & -1 & 1 \\ 0 & 0 & 1 & 1 \end{pmatrix} \\ \langle \hat{A}_1 \otimes \hat{B}_0 \rangle &= \frac{1}{\sqrt{2}} \begin{pmatrix} 0 & 0 & 1 & -1 \\ 0 & 0 & -1 & -1 \\ 1 & -1 & 0 & 0 \\ -1 & -1 & 0 & 0 \end{pmatrix} \\ \langle \hat{A}_1 \otimes \hat{B}_1 \rangle &= \frac{1}{\sqrt{2}} \begin{pmatrix} 0 & 0 & 1 & 1 \\ 0 & 0 & 1 & -1 \\ 1 & 1 & 0 & 0 \\ 1 & -1 & 0 & 0 \end{pmatrix} \end{aligned} \tag{1.65}$$

Then, in the case of $|\phi^+\rangle$, the expectation values become:

$$\langle \phi^+ | \hat{A}_0 \otimes \hat{B}_0 | \phi^+ \rangle = \langle \phi^+ | \hat{A}_0 \otimes \hat{B}_1 | \phi^+ \rangle = \langle \phi^+ | \hat{A}_1 \otimes \hat{B}_0 | \phi^+ \rangle = - \langle \phi^+ | \hat{A}_1 \otimes \hat{B}_1 | \phi^+ \rangle = \frac{1}{\sqrt{2}} \tag{1.66}$$

As a consequence, we get $S = \frac{4}{\sqrt{2}} = 2\sqrt{2}$. The result is the same for the other Bell states up to relabeling of the observables and sign changes. Now, one can be interested in verifying that this is the maximal violation (a proof is shown in [25]). We can apply the *sum of squares (SOS)* decomposition to the operator $2\sqrt{2}\mathbb{I} - \hat{S}$ and rewrite it as:

$$2\sqrt{2}\mathbb{I} - \hat{S} = \frac{1}{\sqrt{2}} \left[\left(\frac{\hat{A}_0 + \hat{A}_1}{\sqrt{2}} - \hat{B}_0 \right)^2 + \left(\frac{\hat{A}_0 - \hat{A}_1}{\sqrt{2}} - \hat{B}_1 \right)^2 \right] \tag{1.67}$$

In particular, it is easy to see that $2\sqrt{2}\mathbb{I} - \hat{S} \geq 0$ and, as a consequence the value of $S \leq 2\sqrt{2}$. The CHSH inequality is maximally violated when $2\sqrt{2}\mathbb{I} - \hat{S} = 0$, which is possible if:

$$\frac{\hat{A}_0 \pm \hat{A}_1}{\sqrt{2}} |\psi\rangle = \hat{B}_{0/1} |\psi\rangle \tag{1.68}$$

Moreover, one can prove that all the possible local measurements that maximally violate the CHSH inequality are equivalent to Eq. (1.67) up to a unitary transformation.

Experimentally, it is possible to evaluate S in terms of polarization measurements performed through an HWP and a PBS on the biphoton state (see also Sec. 1.3.1). Both parties, Alice and Bob, receive one of the two photons and they can perform a projective measurement on it. We denote as θ_1 and θ_1' the two possible settings on side A and, in a similar way, θ_2 and θ_2' on side B. Both parties can arbitrarily set one of the two possible measurement configurations and then perform a measurement on their part of the system getting as result ± 1. When the statistic is sufficiently large the two parties can compare the results obtained for each particular combination of the selected operators. The correlation of the particle pairs for any possible choice of the operators is denoted as $E(\theta_1^{(a)}, \theta_2^{(b)})$ (where a and b denote the possible choice of the measurement settings in each party) which is the expectation value of the product of the outcomes of the experiment for that choice of the operators. The CHSH inequality can be written as:

$$S = |E(\theta_1, \theta_2) + E(\theta_1, \theta_2') + E(\theta_1', \theta_2) - E(\theta_1', \theta_2')| \leq 2 \tag{1.69}$$

We can relate the operators in Eq. (1.64) to certain polarization projective measurements and then estimating the correlators $E(\theta_1^{(a)}, \theta_2^{(b)})$ for any choice of the angles $\theta_1^{(a)}$ and $\theta_1^{(b)}$ (see Appendix A for further details). For any configuration of the polarization measurement operators, we can evaluate the number of coincidences $N_c(\theta_1^{(a)}, \theta_1^{(b)})$ between the events recorded in each party which is proportional to the probability $p(ab|xy)$. After some manipulations, we get an expression for the correlators

$$E(\theta_1^{(a)}, \theta_1^{(b)}) = \frac{N_c(\theta_1^{(a)}, \theta_2^{(b)}) + N_c(\theta_1^{(a)\perp}, \theta_2^{(b)\perp}) - N_c(\theta_1^{(a)\perp}, \theta_2^{(b)}) - N_c(\theta_1^{(a)}, \theta_2^{(b)\perp})}{N_c(\theta_1^{(a)}, \theta_2^{(b)}) + N_c(\theta_1^{(a)\perp}, \theta_2^{(b)\perp}) + N_c(\theta_1^{(a)\perp}, \theta_2^{(b)}) + N_c(\theta_1^{(a)}, \theta_2^{(b)\perp})} \tag{1.70}$$

where $\theta^\perp = \theta + 90°$ and $N_c(\theta_1^{(a)}, \theta_2^{(b)})$ is the number of experimental coincidences measured in a unit of time for a certain choice of the polarization measurement $(\theta_1^{(a)}, \theta_2^{(b)})$. Consistently with the operators in Eq. (1.64) the choice of the polarization measurements which allow to maximally violate the CHSH inequalities are $(\theta_1, \theta_1', \theta_2, \theta_2') = (0, 45°, 22.5°, 157.5°)$ (see Fig. 1.4).

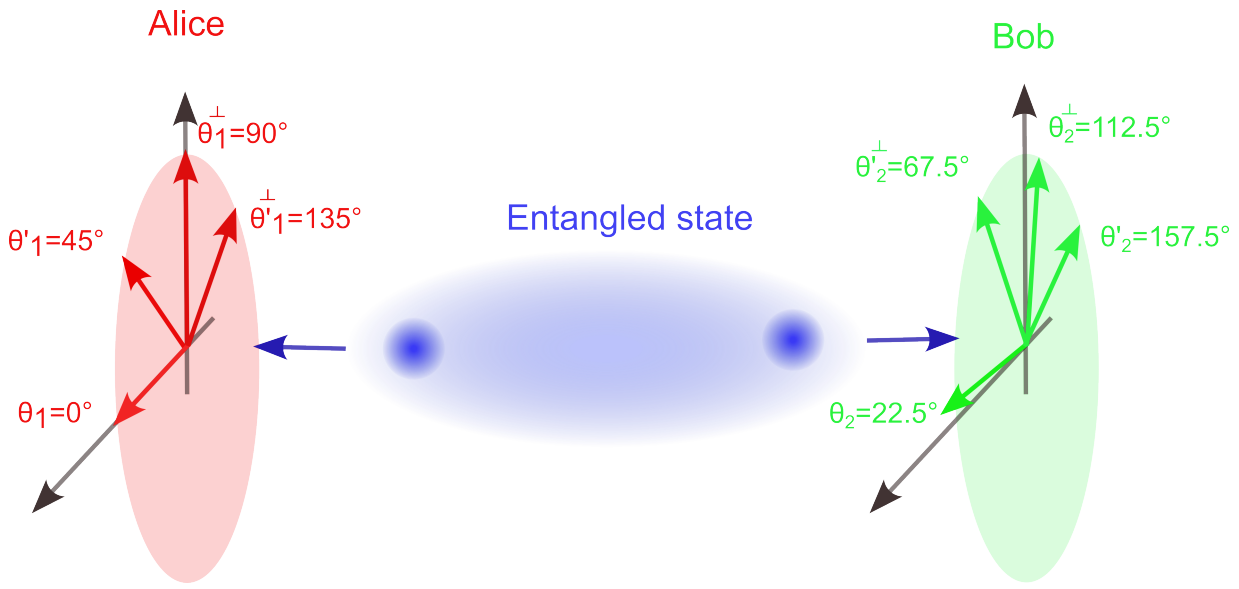

Figure 1.4: Scheme of the measurements for CHSH inequality.

1.5 Quality of Entangled States

Several methods are used to evaluate the quality of the entanglement of a two-qubit system. Here, we introduce some of the most significant quantities employed in this work, which are all related to the experimental measurement of visibility in different bases.

1.5.1 Polarization Correlation Visibility

When dealing with the features of a quantum system a suitable choice of projective measurements allows to characterize the presence of entanglement. The key point consists in performing measurements in different bases. Consider, for example, the maximally entangled state $|\Phi^+\rangle$. This state can be written in different bases as:

$$\left|\Phi^+\right\rangle = \frac{1}{\sqrt{2}}(|HH\rangle + |VV\rangle) = \frac{1}{\sqrt{2}}(|DD\rangle + |AA\rangle) = \frac{1}{\sqrt{2}}(|RR\rangle + |LL\rangle) \tag{1.71}$$

We observe that if we measure this state in the $\mathbb{Z}$-basis, the corresponding probabilities are $p_{HH} = p_{VV} = \frac{1}{2}$ and $p_{HV} = p_{VH} = 0$. Similarly, measuring in the $\mathbb{X}$ and $\mathbb{Y}$ bases we get $p_{DD} = p_{AA} = p_{RR} = p_{LL} = \frac{1}{2}$ and $p_{DA} = p_{AD} = p_{RL} = p_{LR} = 0$. The experimental count rates, which are proportional to the probabilities of the corresponding projective measurement, depend on the particular choice of projection performed on the system. In the $\mathbb{Z}$-basis we have that the maximum count rate is $N_{max} = N_{HH} = N_{VV}$ and $N_{min} = N_{HV} = N_{VH} = 0$. A similar approach can be applied for the measurements performed on the other two bases. The same procedure is valid also for the other Bell states, but in this case, the maxima and minima count rates can be found with different measurements.

A useful quantity, strictly related to the experimental results, is the polarization correlation visibility, defined as follows:

$$V = \frac{N_{max} - N_{min}}{N_{max} + N_{min}} \tag{1.72}$$

However, count rates may vary due to differences such as the presence of different optical elements, or misalignments in the optics and due to a non maximally entangled state. To address this, it is advisable to remove any bias in the measurement of visibility. We can redefine the visibility in a given basis $\{|a\rangle, |b\rangle\}$ as

$$V = \frac{|N_{aa} + N_{bb} - N_{ab} - N_{ba}|}{N_{aa} + N_{bb} + N_{ab} + N_{ba}} \tag{1.73}$$

The absolute value has been employed, as depending on the specific decomposition of the state in terms of $|a\rangle$ and $|b\rangle$, the numerator could be either positive or negative.

Measuring the visibility of a state in a set of mutually unbiased bases is crucial for assessing the presence of entanglement. Only a maximally entangled state exhibits a visibility equal to one in each of these bases. In practice, demonstrating a change in visibility in two distinct mutually unbiased bases is sufficient to indicate that we do not have a Bell state. For this purpose, we choose the $\mathbb{Z}$ and $\mathbb{X}$ bases, which are simpler to experimental measure, since it is sufficient the use of only an HWP and a PBS (as shown in Sec. 1.3.1).

With this parametrization, we can rewrite the state of a two-qubit system as

$$|\psi\rangle = \cos\phi\,|HH\rangle + \sin\phi\,|VV\rangle \tag{1.74}$$

In this way we can write the maximally entangled states $|\Phi^\pm\rangle$ setting $\phi = \pm\frac{\pi}{4}$ and the separable states $|HH\rangle$ (for $\phi = 0$) and $|VV\rangle$ (for $\phi = \frac{\pi}{2}$)[4] This approach allows to show how the visibilities on the $\mathbb{Z}$ ($V_{\mathbb{Z}}$) and $\mathbb{X}$ ($V_{\mathbb{X}}$) bases change varying the parameter ϕ. This goal is achieved, by evaluating the probability of each measurement: $p_i = \langle\psi|\,\hat{\Pi}_i\,|\psi\rangle$. The visibilities are related to these probabilities, once simplified by the common multiplicative constant, in the following way:

$$V_{\mathbb{Z}} = \frac{p_{HH} + p_{VV} - p_{HV} - p_{VH}}{p_{HH} + p_{VV} + p_{HV} + p_{VH}} \qquad V_{\mathbb{X}} = \frac{p_{DD} + p_{AA} - p_{DA} - p_{AD}}{p_{DD} + p_{AA} + p_{DA} + p_{AD}} \tag{1.75}$$

The probabilities of each measurement, as a function of ϕ are listed in Tab. 1.1 Therefore the visibilities as a function of ϕ, become:

$$V_{\mathbb{Z}} = 1 \qquad V_{\mathbb{X}} = \sin 2\phi \tag{1.76}$$

[4]With a similar approach one can also write $\left|\Psi^\pm\right\rangle$, with the parametrization $|\psi\rangle = \cos\phi\,|HV\rangle + \sin\phi\,|VH\rangle$. The following arguments are the same.

$\mathbb{Z}$	p	$\mathbb{X}$	p
HH	$\cos^2\phi$	DD	$[1+\sin(2\phi)]/4$
HV	0	DA	$[1-\sin(2\phi)]/4$
VH	0	AD	$[1-\sin(2\phi)]/4$
VV	$\sin^2\phi$	AA	$[1+\sin(2\phi)]/4$

Table 1.1: Measurement probability of a generic two-qubit state.

While the visibility $V_{\mathbb{Z}}$ is always equal to one, the visibility in the $\mathbb{X}$-basis changes depending on the value of ϕ. $V_{\mathbb{X}} = 1$ only in the case of a maximally entangled state ($\phi = \frac{\pi}{4}$) and it is equal to zero in the case of a separable state ($\phi = 0, \frac{\pi}{2}$). This argument shows the importance of the visibility measure, performed on two independent bases. This quantity is used to evaluate the quality of the entangled photons produced by the source.

1.5.2 Fidelity

The fidelity is a measure of the *closeness* of two quantum states [26]. It is defined as

$$F(\hat{\rho},\hat{\sigma}) = \left(Tr\sqrt{\sqrt{\hat{\sigma}}\hat{\rho}\sqrt{\hat{\sigma}}}\right)^2 \tag{1.77}$$

where $\hat{\rho}$ and $\hat{\sigma}$ are the density matrices of the two states. If they are pure, the fidelity can be written as

$$F(\hat{\rho},\hat{\sigma}) = |\langle\psi_\rho|\psi_\sigma\rangle|^2 \tag{1.78}$$

which represents the projection probability of the state $|\psi_\rho\rangle$ on $|\psi_\sigma\rangle$. One can simply observe that in the case of two identical states $F(\hat{\rho},\hat{\rho}) = 1$, and in the case they are orthogonal their fidelity is zero.

Some of the most important properties of quantum state fidelity are:

- **Limited values**: The values of the fidelity are $0 \leq F(\hat{\rho},\hat{\sigma}) \leq 1$ for any choice of the density matrices $\hat{\rho}$ and $\hat{\sigma}$. In particular $F(\hat{\rho},\hat{\sigma}) = 1$ if and only if $\hat{\rho} = \hat{\sigma}$;
- **Symmetry**: The fidelity of two quantum states is symmetric in its arguments $F(\hat{\rho},\hat{\sigma}) = F(\hat{\sigma},\hat{\rho})$;
- **Composite systems:** If we have a composite Hilbert space $\mathcal{H}_A \otimes \mathcal{H}_B$ and the density matrices $\hat{\rho}_1,\hat{\sigma}_1$ describe two states in $\mathcal{H}_A$, while $\hat{\rho}_2,\hat{\sigma}_2$ two states in $\mathcal{H}_B$ we get $F(\hat{\rho}_1\otimes\hat{\rho}_2,\hat{\sigma}_1\otimes\hat{\sigma}_2) = F(\hat{\rho}_1,\hat{\sigma}_1)F(\hat{\rho}_2,\hat{\sigma}_2)$;
- **Invariance under unitary transformations:** unitary transformations of the states don't change their fidelity $F(\hat{U}\hat{\rho}\hat{U}^\dagger,\hat{U}\hat{\sigma}\hat{U}^\dagger) = F(\hat{\rho},\hat{\sigma})$;

The fidelity is not a distance, as the triangle inequality does not apply. Moreover, we have seen that $F(\hat{\rho},\hat{\rho}) = 1$ instead of zero, as for a usual distance. However, fidelity remains one of the most commonly employed measures for quantifying the closeness of two quantum states. In this thesis, we will assess the fidelity between the states emitted by the source and a maximally entangled state. One can demonstrate that this quantity, also known as *Bell-state fidelity* can be estimated from the measure of the visibilities as follows [27,28]

$$F(\hat{\rho}) = \frac{1+V_{\mathbb{Z}}+V_{\mathbb{X}}+V_{\mathbb{Y}}}{4} \tag{1.79}$$

It is possible to bound the inferior limit of the fidelity, given an estimation of the visibility on the $\mathbb{Z}$ and $\mathbb{X}$ bases [26,29]. This result is important because these measurements typically provide more precise results since we can perform a lower number of measurements. Moreover, these two bases require only a HWP reducing the error due to the correct positioning of the QWP for the visibility $V_{\mathbb{Y}}$. The inferior limit of the Bell-state fidelity becomes

$$F(\hat{\rho}) \geq \frac{V_{\mathbb{Z}}+V_{\mathbb{X}}}{2} \tag{1.80}$$

1.5.3 Concurrence

Concurrence, introduced by Hill and Wootters [30], is a measure of entanglement for a two-qubit quantum system. It is defined as

$$C(\hat{\rho}) = \max\{0, \lambda_1 - \lambda_2 - \lambda_3 - \lambda_4\} \tag{1.81}$$

where $\{\lambda_1, \lambda_2, \lambda_3, \lambda_4\}$ are the eigenvalues of the matrix $\hat{R} = \sqrt{\sqrt{\hat{\rho}}\hat{\tilde{\rho}}\sqrt{\hat{\rho}}}$, taken in decreasing order. Given the state $\hat{\rho}$ the matrix $\hat{R}$ is defined in terms of :

$$\hat{\tilde{\rho}} = (\sigma_y \otimes \sigma_y)\hat{\rho}^*(\sigma_y \otimes \sigma_y) \tag{1.82}$$

This definition, which appears quite complicated, arises as a generalization of concurrence for pure states. Given a pure state $|\psi\rangle$, the concurrence is defined as:

$$C(|\psi\rangle) = \sqrt{2[1 - Tr(\hat{\rho}_A^2)]} \tag{1.83}$$

where $\hat{\rho}_A$ is the reduced state of $|\psi\rangle$ on one of the two subsyestems. The idea is that when the state is maximally entangled, $\hat{\rho}_A = \frac{1}{2}\mathbb{I}$ and the concurrence is one. In the opposite case, if the state is separable $Tr(\hat{\rho}_A^2) = Tr(\hat{\rho}_A) = 1$ and the concurrence is equal to zero.

The most important properties of this measure are:

- **Limited values**: For any bipartite state $0 \leq C(\hat{\rho}) \leq 1$. In particular, any separable state has a concurrence equal to zero, while for a maximally entangled state, it is equal to one.
- **Symmetry**: The concurrence is symmetric under the interchange of the two subsystems. In other words, if we swap the labels of the two qubits, the concurrence remains the same.
- **Monotonicity**: this measure is a monotonic function of entanglement. This means that any operation that does not increase the entanglement between two qubits also does not increase the concurrence.
- **Invariance under local unitary transformations**: Local unitary operations are transformations that only affect one of the subsystems and do not change the entanglement properties. Concurrence remains unchanged under local unitary operations applied independently to each subsystem.

Similarly to the fidelity, also the concurrence can be estimated via lower bound, using the results of the visibilities in the $\mathbb{Z}$ and $\mathbb{X}$ bases [26, 29]:

$$C(\hat{\rho}) \geq V_{\mathbb{Z}} + V_{\mathbb{X}} - 1 \tag{1.84}$$

1.6 Quantum State Tomography

The information carried by a quantum particle is encoded in its state and it's accessible through measurements. Quantum state tomography is a technique employed to fully reconstruct the quantum state of a system, obtaining a detailed and accurate description of its properties. The approach of quantum state tomography involves performing a series of measurements on the system in different ways, thus obtaining a set of experimental data. These data are then analyzed using specialized mathematical algorithms to extract information about the original quantum state.

For the purpose of this thesis, here we describe the quantum tomography of a two-qubit system. The general expression of a two-qubit system state is a 4×4 matrix density $\hat{\rho}$:

$$\hat{\rho} = \begin{pmatrix} \rho_{11} & \rho_{12} & \rho_{13} & \rho_{14} \\ \rho_{21} & \rho_{22} & \rho_{23} & \rho_{24} \\ \rho_{31} & \rho_{32} & \rho_{33} & \rho_{34} \\ \rho_{41} & \rho_{42} & \rho_{43} & \rho_{44} \end{pmatrix} \tag{1.85}$$

Quantum tomography aims at providing a way to relate the coefficients ρ_{ij} with experimental measurable quantities. A simple experimental approach consists in performing projective measurements on the bases $\{\mathbb{X}, \mathbb{Y}, \mathbb{Z}\}$. We need to relate these quantities with the coefficients of the density matrix in Eq. (1.85). A useful approach is the one described by James et. al [31], which consists of a parametrization of the density matrix through an auxiliary matrix $\hat{T}$:

$$\hat{T} = \begin{pmatrix} t_1 & 0 & 0 & 0 \\ t_5 + it_6 & t_2 & 0 & 0 \\ t_{11} + it_{12} & t_7 + it_8 & t_3 & 0 \\ t_{15} + it_{16} & t_{13} + it_{14} & t_9 + it_{10} & t_4 \end{pmatrix} \tag{1.86}$$

The density matrix can be written as:

$$\hat{\rho} = \frac{\hat{T}^\dagger \hat{T}}{Tr(\hat{T}^\dagger \hat{T})} \tag{1.87}$$

which can be easily proved to satisfy the properties of a density matrix:

- Positive definite: $\langle\psi| \frac{\hat{T}^\dagger \hat{T}}{Tr(\hat{T}^\dagger \hat{T})} |\psi\rangle \geq 0, \forall |\psi\rangle \in \mathcal{H}$;
- Normalization: $Tr \frac{\hat{T}^\dagger \hat{T}}{Tr(\hat{T}^\dagger \hat{T})} = 1$;
- Hermitian: $\frac{\hat{T}^\dagger \hat{T}}{Tr(\hat{T}^\dagger \hat{T})} = \frac{(\hat{T}^\dagger \hat{T})^\dagger}{Tr(\hat{T}^\dagger \hat{T})}$;

The density matrix is related to the parameters t_i with $i \in \{1, ..., 16\}$. This approach shows that any density matrix can be completely characterized by 16 real quantities. The object of quantum state tomography consists in finding the optimal set of parameters based on certain experimental measurements. Given the complete set of mutually unbiased bases $\{\mathbb{X}, \mathbb{Y}, \mathbb{Z}\}$, we can perform 6 projective measurements (two for each basis) along orthogonal vectors, which are: $\{|H\rangle, |V\rangle, |D\rangle, |A\rangle, |L\rangle, |R\rangle\}$. Therefore we can perform at most 36 measurements of the bipartite system, considering all the possible combinations. However, the system can be fully characterized by 16 measurements while the others are redundant. Each projective measurement, indeed, is represented by a 4×4 matrix: to fully characterize the state of the system it is sufficient to select a set of 16 linearly independent operators. The description of the projective operators, together with the experimental realization of these measurements, is discussed in Appendix B. Given the experimental results, we need to provide a method to reconstruct the quantum state of the system.

1.6.1 Maximum Likelihood Estimation

This method consists in the definition of a likelihood function containing the parameters which characterize the quantum state $\vec{t} = (t_1, ..., t_{16})$ and the experimental measurements: it estimates the agreement of a certain density matrix $\hat{\rho}(\vec{t})$ with the experimental measurements. The simpler approach to build this function consists in assuming Gaussian probability distributions of the experimental results.

$$P(\vec{t}) = \frac{1}{\mathcal{N}} \prod_{\nu=1}^{16} \exp\left\{ -\frac{[\bar{n}_\nu(\vec{t}) - n_\nu]^2}{2\hat{\sigma}_\nu(\vec{t})^2} \right\} \tag{1.88}$$

where $\mathcal{N}$ is a normalization constant, while the normalized ν-th measurement, performed by projecting the bipartite system in the state $|\psi_\nu\rangle$ is:

$$\bar{n}_\nu(\vec{t}) = Tr(\hat{\rho}(\vec{t})\hat{\Pi}_\nu) \tag{1.89}$$

where $\hat{\Pi}_\nu = |\psi_\nu\rangle \langle\psi_\nu|$ is the projector on the state $|\psi_\nu\rangle$. The experimental normalized results are n_ν which are obtained from the experimental coincidence counts N_ν as

$$n_\nu = \frac{N_\nu}{N_{norm}} \tag{1.90}$$

The normalization constant is experimentally obtained from all the counts obtained in a given basis, for example, the $\mathbb{Z}$-basis: $N_{norm} = N_{HH} + N_{VV} + N_{HV} + N_{VH}$. The uncertainty of the ν-th measurement is obtained assuming that the probability distribution of the counts is Poissonian $\hat{\sigma}_\nu(\vec{t}) = \sqrt{\bar{n}_\nu(\vec{t})}$[5]. The likelihood obtainable from the experimental values is:

$$P(\vec{t}) = \frac{1}{\mathcal{N}} \prod_{\nu=1}^{16} \exp\left\{ -\frac{\left[Tr(\hat{\rho}(\vec{t})\hat{\Pi}_\nu) - n_\nu\right]^2}{2Tr(\hat{\rho}(\vec{t})\hat{\Pi}_\nu)} \right\} \tag{1.91}$$

The maximization of the likelihood function allows us to determine the best estimation of the quantum state. Alternatively, this problem is equivalent to the minimization of $-\log(P(\vec{t}))$:

$$\mathcal{L}(t_1, ..., t_{16}) = \sum_{\nu=1}^{16} \frac{(Tr(\hat{\rho}(t_1, ..., t_{16})\hat{\Pi}_\nu) - n_\nu)^2}{2Tr(\hat{\rho}((t_1, ..., t_{16})\hat{\Pi}_\nu)} \tag{1.92}$$

Once the minimum is found for certain parameters $(t'_1, t'_2, ..., t'_{16})$, the density matrix of the state can be reconstructed.

Uncertainty Analysis

A non-trivial problem related to the maximum likelihood method is the error analysis. Every experiment inherently possesses finite accuracy, and it is essential for an experimenter to provide a report on this accuracy alongside the results. However, maximum likelihood tomography lacks an analytical solution for estimating the accuracy of the procedure and, more critically, the uncertainty in the derived parameters caused by experimental uncertainties due, for example, to the correct positioning of the waveplates and to the fluctuations of the experimental counts. In the literature, the prevailing approach to estimate these uncertainties consists in the use of Monte Carlo simulations. These techniques enable the simulation of the experiment multiple times, providing an estimate of the associated experimental uncertainties without the need to actually repeat the experiment hundreds of times. With this approach, we can effectively predict the uncertainties due to statistical fluctuations of the counts but we ignored that due to the positioning of the waveplates (that may be also systematic).

For each measurement, we get an estimated n_ν, which is assumed to be normally distributed with a standard deviation $\sqrt{n_\nu}$. Given the set of experimental results n_ν one can associate a Gaussian distribution with the experimental result as mean value and the standard deviation $\sqrt{n_\nu}$. Therefore, we can simulate many experiments repeating the quantum tomography many times using as input values the ones extracted in each run by the individual Gaussian distribution of each measurement. In this way, after many iterations, we can quantify the dispersion of the optimal parameters that characterized the reconstructed quantum state.

1.6.2 Experimental Effective Model

A complete quantum state tomography is typically difficult to perform due to the uncertainties related to this method. In Sec. 1.5 we stressed the importance of the visibilities in the $\mathbb{Z}$ and $\mathbb{X}$ bases to evaluate the quality of entangled states. Through these values, moreover, we are able to estimate a lower bound of the Bell-state fidelity and that of the concurrence. In this section, we will show that these two measurements can provide deeper information on the state of the photons emitted by the source. Consider the scenario where the source emits the Bell state $|\Phi^+\rangle$[6]. The ideal state emitted by the source should be described in the formalism of density matrices as $\hat{\rho} = |\Phi^+\rangle\langle\Phi^+|$. In practice, there are some contributions that ruin the degree of entanglement of the system. They are:

[5]The statistical distribution related to the detected counting rates is a Poissonian. Generally, for high statistic samples, this distribution converges to a Gaussian.

[6]The source can be configured to emit any Bell state. Specifically, in the experimental tests summarized in Sec. 5, the source was set up to emit the state $|\Phi^+\rangle$, which is why we will focus on this particular case. The others can be treated similarly.

- **Depolarization**: The optical elements of the source, the optical fibers, and the PBSs used for the polarization measurements partially depolarize the transmitted states, destroying quantum correlations. Mathematically, this process introduces a uniform noise in the density matrix, that can be represented as $\frac{p}{4}\mathbb{I}$. The parameter p is a measure of the strength of the depolarization process.
- **Decoherence**: Experimentally, it is difficult to create maximally entangled states. The source, due to misalignments, could introduce a small distinguishability between the states of the two photons, thus reducing the coherence. This effect can be modeled, in the formalism of the density matrices, by an additional factor $\frac{c}{2}(|HH\rangle\langle HH| + |VV\rangle\langle VV|)$, regulated by the parameter c.

The effective model for the states emitted by the source, considering the effects of depolarization and decoherence, can be written as:

$$\hat{\rho}_{AB} = (1-p-c)\left|\phi^+_{AB}\right\rangle\left\langle\phi^+_{AB}\right| + \frac{p}{4}\mathbb{I} + c\frac{|HH\rangle\langle HH| + |VV\rangle\langle VV|}{2} \qquad p, c \in \mathbb{R} \tag{1.93}$$

The parameters p and c can be derived from the experimental measurements of the visibilities $V_{\mathbb{Z}}$ and $V_{\mathbb{X}}$. To show this, we can start by defining the probabilities of each projective measurement on the $\mathbb{Z}$ and $\mathbb{X}$ bases using the model introduced in Eq. (1.93). In the $\mathbb{Z}$-basis we get the following probabilities:

$$\begin{aligned} p_{HH} &= Tr(\hat{\rho}_{AB}\,|HH\rangle\langle HH|) = \frac{2-p}{4} \\ p_{HV} &= Tr(\hat{\rho}_{AB}\,|HV\rangle\langle HV|) = \frac{p}{4} \end{aligned} \tag{1.94}$$

For symmetry $p_{VV} = p_{HH}$ and $p_{VH} = p_{HV}$. Therefore, the visibility $V_{\mathbb{Z}}$ can be written in terms of the p parameter as

$$V_{\mathbb{Z}} = \frac{p_{HH} + p_{VV} - p_{HV} - p_{VH}}{p_{HH} + p_{VV} - p_{HV} - p_{VH}} = 1 - p \tag{1.95}$$

Similarly, the probabilities for the measurements in the $\mathbb{X}$-basis are:

$$\begin{aligned} p_{DD} &= Tr(\hat{\rho}_{AB}\,|DD\rangle\langle DD|) = \frac{2-p-c}{4} \\ p_{DA} &= Tr(\hat{\rho}_{AB}\,|DA\rangle\langle DA|) = \frac{p+c}{4} \end{aligned} \tag{1.96}$$

and for symmetry $p_{AA} = p_{DD}$ and $p_{DA} = p_{AD}$. The visibility $V_{\mathbb{X}}$ becomes

$$V_{\mathbb{X}} = \frac{p_{DD} + p_{AA} - p_{DA} - p_{AD}}{p_{DD} + p_{AA} + p_{DA} + p_{AD}} = 1 - p - c \tag{1.97}$$

The coefficients which characterize the effective model of the biphoton state are expressed in terms of the visibilities as

$$\begin{aligned} p &= 1 - V_{\mathbb{Z}} \\ c &= V_{\mathbb{Z}} - V_{\mathbb{X}} \end{aligned} \tag{1.98}$$

This model allows also to predict the value of S in CHSH inequality. To do this we can directly calculate S in Eq. (1.63) by evaluating all the correlators in the state $\hat{\rho}_{AB}$ of the Eq. (1.93). Finally, we get:

$$\begin{aligned} \langle\hat{A}_0\hat{B}_0\rangle = \langle\hat{A}_0\hat{B}_1\rangle &= \frac{1-p}{\sqrt{2}} = \frac{V_{\mathbb{Z}}}{\sqrt{2}} \\ \langle\hat{A}_1\hat{B}_0\rangle = -\langle\hat{A}_1\hat{B}_1\rangle &= \frac{1-p-c}{\sqrt{2}} = \frac{V_{\mathbb{X}}}{\sqrt{2}} \end{aligned} \tag{1.99}$$

The expression that relates S to the experimental visibilities $V_{\mathbb{Z}}$ and $V_{\mathbb{X}}$ is

$$S = \sqrt{2}(V_{\mathbb{X}} + V_{\mathbb{Z}}) \tag{1.100}$$

Chapter 2

Spontaneous Parametric Down-Conversion

Spontaneous Parametric Down-Conversion (SPDC) is a fundamental process extensively used in quantum communications to generate entangled photons. This second-order nonlinear optical process involves the conversion of a single high-energy pump photon into two lower-frequency photons passing through an optical material. The properties of the emitted photons, and thus of the source, strongly depend on the characteristics of both the nonlinear crystal and the pump beam. In this chapter, we will explore the physical origin of SPDC, with a particular emphasis on characterizing its properties. Specifically, we will describe the model used to analyze the source's performance under different configurations.

2.1 Electromagnetism in a Nonlinear Medium

To study nonlinear optics, it is necessary to describe the behavior of an electromagnetic field in a medium. In the absence of free charges and currents, Maxwell's equations within a medium are given as [32]:

$$\begin{cases} \boldsymbol{\nabla} \cdot \mathbf{D}(\mathbf{r},t) = 0 \\ \boldsymbol{\nabla} \cdot \mathbf{H}(\mathbf{r},t) = 0 \\ \boldsymbol{\nabla} \times \mathbf{E}(\mathbf{r},t) = -\frac{\partial \mathbf{B}(\mathbf{r},t)}{\partial t} \\ \boldsymbol{\nabla} \times \mathbf{H}(\mathbf{r},t) = \frac{\partial \mathbf{D}(\mathbf{r},t)}{\partial t} \end{cases} \tag{2.1}$$

where $\mathbf{E}(\mathbf{r},t)$ is the electric field, $\mathbf{B}(\mathbf{r},t)$ is the magnetic field and the vector field $\mathbf{H}(\mathbf{r},t)$, in non-ferromagnetic media, is defined as $\mathbf{H}(\mathbf{r},t) = \frac{1}{\mu}\mathbf{B}(\mathbf{r},t)$ (where μ is the magnetic permeability). An important quantity is the electric displacement vector field $\mathbf{D}(\mathbf{r},t)$ which is written as

$$\mathbf{D}(\mathbf{r},t) = \epsilon_0 \mathbf{E}(\mathbf{r},t) + \mathbf{P}(\mathbf{r},t) \tag{2.2}$$

where ϵ_0 is the electric permittivity of vacuum and $\mathbf{P}(\mathbf{r},t)$ is the polarization field induced on the material under the action of an external electric field. In a nonlinear medium the polarization field can be expressed as a series of powers of the electric field:

$$\mathbf{P}(\mathbf{r},t) = \epsilon_0 \chi^{(1)} \mathbf{E}(\mathbf{r},t) + \epsilon_0 \chi^{(2)} \mathbf{E}(\mathbf{r},t)\mathbf{E}(\mathbf{r},t) + \epsilon_0 \chi^{(3)} \mathbf{E}(\mathbf{r},t)\mathbf{E}(\mathbf{r},t)\mathbf{E}(\mathbf{r},t) + ... \tag{2.3}$$

The linear susceptibility $\chi^{(1)}$ characterizes the dominant factor for low intensities of the electric field. When the applied electric field becomes sufficiently intense, higher-order terms become significant and as a result, we can see nonlinear effects. These contributions depend on the susceptibility tensors $\chi^{(i)}$ (with $i \geq 2$), whose components are typically several orders of magnitude smaller than those of $\chi^{(1)}$. Second-order nonlinear effects can only occur in noncentrosymmetric crystals, which are crystals that do not display inversion symmetry [33]. These effects are relevant for the SPDC process as we will explain in the following sections.

2.2 SPDC Theoretical Model

When an electromagnetic wave interacts within a medium, dipolar interactions can occur between the dipoles of the medium and the electromagnetic field of the radiation. As a result, the electric dipoles oscillate at well-defined frequencies, acting, if the relative phase is correct, as a source of new electromagnetic radiations. More precisely, starting by Maxwell's equations (2.1) we can derive the wave equation of an electromagnetic field propagating in a medium:

$$\nabla^2 \mathbf{E}(\mathbf{r},t) - \frac{1}{c^2}\frac{\partial^2 \mathbf{E}(\mathbf{r},t)}{\partial t^2} = \frac{1}{\epsilon_0 c^2}\frac{\partial^2 \mathbf{P}(\mathbf{r},t)}{\partial t^2} \tag{2.4}$$

where the polarization field $\mathbf{P}(\mathbf{r},t)$ is defined in Eq. (2.3). When dealing with second-order nonlinear effects, we can focus only on the second-order term, whose components are:

$$\mathbf{P}_i^{(2)}(\mathbf{r},t) = \epsilon_0 \chi_{ijk}^{(2)} \mathbf{E}_j(\mathbf{r},t)\mathbf{E}_k(\mathbf{r},t) \tag{2.5}$$

where we employed Einstein's notation to simplify the tensor product. Eq. (2.4), which describes the evolution of an electromagnetic wave in a medium, is a nonhomogeneous differential equation due to the presence of a nonzero polarization term on the right-hand side.

The polarization field depends on the electric field of the radiation incident on the nonlinear medium and can be considered as the source of the emitted radiation as described before. Following this concept, the emitted electromagnetic field, in turn, induces polarization in the medium, which results in a modification of the radiation itself, and so on. This physical process suggests an iterative solution for Eq. (2.4). We begin by solving the homogeneous differential equation (which corresponds to a wave propagating in vacuum), leading to a plane wave solution. This wave corresponds to the electric field which is incident on the nonlinear medium. Subsequently, we insert it into the polarization term finding, at the first order, the radiation source. This type of approach to solve the differential equation (2.4) represents the first step of the Born approximation. [34].

Suppose for example, the incident radiation $\mathbf{E_0}(\mathbf{r},t)$ on the nonlinear medium has two different frequency components, ω_1 and ω_2. The polarization term, which is quadratic in $\mathbf{E_0}(\mathbf{r},t)$ will then have components at five angular frequencies: 0, $2\omega_1$, $2\omega_2$, $\omega_+ = \omega_1 + \omega_2$, and $\omega_- = \omega_1 - \omega_2$ [34]. According to Born's first approximation, the polarization term contains the same spectral components as the emitted radiation ω_3 [34]. In the literature, these correspond to different processes, commonly known as optical rectification ($\omega_3 = 0$), second harmonic generation ($\omega_3 = 2\omega_1, 2\omega_2$), sum frequency generation ($\omega_3 = \omega_+$), and difference frequency generation ($\omega_3 = \omega_-$) [33]. However, in order to be effectively generated it is important to notice that the three waves involved in these processes must satisfy the energy and momentum conservation, which correspond to $\omega_3 = \omega_1 + \omega_2$ and $\vec{k}_3 = \vec{k}_1 + \vec{k}_2$ (this condition is known as *phase-matching*[1]). As we will discuss later, this condition could be quite stringent, and usually only one of the frequency components in the polarization term can be generated. Once this wave is generated, it starts interacting with the input waves, in a process called *three-wave mixing process*.

A similar process, involving the interaction of three waves in a nonlinear medium, which is the topic of this thesis, is the SPDC. In this process, a single high-frequency input photon, called the *pump* photon, interacts with a nonlinear crystal and spontaneously splits into two photons of lower frequencies, referred to as the *signal* and *idler* photons. The term *spontaneous* refers to the intrinsic probabilistic nature of this process, while *parametric* indicates that the material's optical parameters, such as refractive indexes, vary based on the energy and polarization of the photons involved. The parametric variation plays a fundamental role in the conservation of energy and momentum during the photon generation process, resulting in photons with lower energy than the pump photon (hence referred to as *downconverted*). In the particular case where the two photons are emitted in the same direction, parallel to the pump beam, it is referred to as collinear SPDC, which is the case of interest for this thesis. An illustration of the collinear and non-collinear SPDC processes is shown in Fig. 2.1.

[1] In the literature, commonly, phase-matching is associated with momentum conservation. However, wavevectors are also constrained by energy conservation. Therefore, for brevity, we denote phase-matching as the combination of both these conditions.

a) Non - Collinear

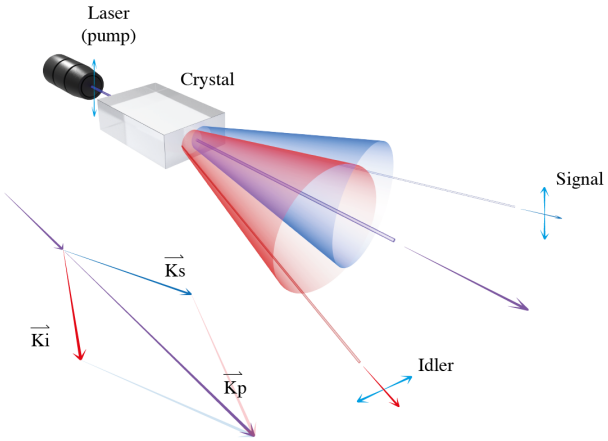

b) Collinear

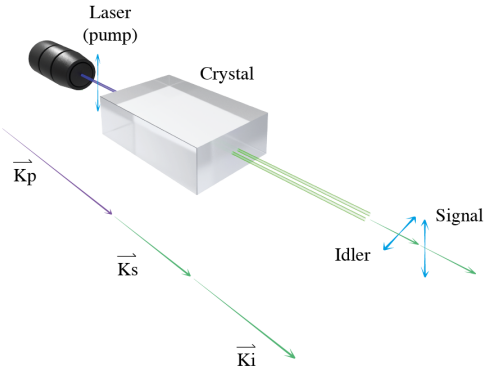

Figure 2.1: Schematic diagrams of SPDC showing the relationship between frequency and polarization of pump, signal and idler beams in a non-collinear (a) and a collinear (b) SPDC process.

The previous discussion on nonlinear effects already introduced, in a classical and intuitive way, some crucial features of SPDC, i.e. the role of the nonlinear terms in the polarization and the phase-matching condition. However, a complete treatment of this phenomenon involves the concept of quantum vacuum, which clearly can not be explained through classical models. A deeper understanding of this phenomenon can only be achieved through a quantum treatment, which will be the object of the model described in the following sections.

2.2.1 SPDC Interaction Hamiltonian

In this section, we will begin a formal description of the SPDC process using the formalism of quantum mechanics. The first step consists in deriving the interaction Hamiltonian for the process. In classical physics, the energy density of an electromagnetic field in a medium is given by [32, 35]:

$$\mathcal{H}(\mathbf{r},t) = \int [\mathbf{H}(\mathbf{r},t)\cdot d\mathbf{H}(\mathbf{r},t) + \mathbf{E}(\mathbf{r},t)\cdot d\mathbf{D}(\mathbf{r},t)] \tag{2.6}$$

while the Hamiltonian can be obtained by integrating over the volume of the system ($\mathcal{V}$) the corresponding energy density:

$$H(t) = \int_{\mathcal{V}} \mathcal{H}(\mathbf{r},t) d^3\mathbf{r} \tag{2.7}$$

Now, we assume that our medium is nonmagnetic which means that the magnetic field is $\mathbf{H}(\mathbf{r},t) = \frac{\mathbf{B}(\mathbf{r},t)}{\mu_0}$. The electric field, instead, can be expressed in terms of the displacement vector field as

$$\mathbf{E}(\mathbf{r},t) = \zeta^{(1)}\mathbf{D}(\mathbf{r},t) + \zeta^{(2)}\mathbf{D}(\mathbf{r},t)\mathbf{D}(\mathbf{r},t) + \zeta^{(3)}\mathbf{D}(\mathbf{r},t)\mathbf{D}(\mathbf{r},t)\mathbf{D}(\mathbf{r},t) + ... \tag{2.8}$$

where $\zeta^{(i)}$ represent the inverse optical susceptibility tensors. With these two assumptions, we are now able to rewrite the energy density of Eq. (2.6):

$$\mathcal{H}(\mathbf{r},t) = \frac{\mathbf{B}^2(\mathbf{r},t)}{2\mu_0} + \frac{1}{2}\zeta^{(1)}\mathbf{D}(\mathbf{r},t)\mathbf{D}(\mathbf{r},t) + \frac{1}{3}\zeta^{(2)}\mathbf{D}(\mathbf{r},t)\mathbf{D}(\mathbf{r},t)\mathbf{D}(\mathbf{r},t) + ... \tag{2.9}$$

This expression can be interpreted as a perturbative expansion of the Hamiltonian density of the form:

$$\mathcal{H}(t) = \mathcal{H}_0(t) + \mathcal{H}_I^{(tot)}(t) \tag{2.10}$$

where $\mathcal{H}_0(t)$ is the zero-order term which corresponds to:

$$\mathcal{H}_0(t) = \frac{\mathbf{B}^2(\mathbf{r},t)}{2\mu_0} + \frac{1}{2}\zeta^{(1)}\mathbf{D}(\mathbf{r},t)\mathbf{D}(\mathbf{r},t) \tag{2.11}$$

This term regulates the interaction of the pump photons with the medium without generating new photons. The interaction part of the Hamiltonian density contains infinite terms involving the expansion of the electric field as a function of the displacement vector field Eq. (2.8). These terms describe the multiphoton interaction induced by the crystal. The SPDC process is related to the production of a photon pair induced by a stimulating photon. To describe this process we can focus on the lower order term of the total interacting Hamiltonian $\mathcal{H}_I^{(tot)}(t)$. Explicitly, the interaction Hamiltonian involved in the SPDC process is:

$$\mathcal{H}_I(t) = \frac{1}{3}\int_{\mathcal{V}} \zeta^{(2)}_{ijk}(\mathbf{r})\mathbf{D}_i(\mathbf{r},t)\mathbf{D}_j(\mathbf{r},t)\mathbf{D}_k(\mathbf{r},t)d^3\mathbf{r} \tag{2.12}$$

We observe that in this equation there are three displacement vector fields that correspond to pump, signal, and idler photons. Until now we have used only arguments derived by classical physics. In quantum mechanics formalism, however, the interaction is mediated by a Hamiltonian operator. The procedure consists of deriving such an operator through the quantization of the displacement vector fields, which are now denoted as p, s, and i (which stand for pump, signal, and idler, respectively) [36]:

$$\hat{\mathcal{H}}_I(t) = \frac{1}{3}\int_{\mathcal{V}} \zeta^{(2)}(\mathbf{r})\hat{\mathbf{D}}_p(\mathbf{r},t)\hat{\mathbf{D}}_s(\mathbf{r},t)\hat{\mathbf{D}}_i(\mathbf{r},t)d^3\mathbf{r} \tag{2.13}$$

Following the approach of R. Glauber [37] we can write the quantized field operator $\hat{\mathbf{D}}$ as:

$$\hat{\mathbf{D}}(\mathbf{r},t) = \int_{-\infty}^{0} \hat{\tilde{\mathbf{D}}}(\mathbf{r},\omega)e^{-i\omega t}d\omega + \int_{0}^{+\infty} \hat{\tilde{\mathbf{D}}}(\mathbf{r},\omega)e^{-i\omega t}d\omega = \hat{\mathbf{D}}^{(-)}(\mathbf{r},t) + \hat{\mathbf{D}}^{(+)}(\mathbf{r},t) \tag{2.14}$$

where $\hat{\mathbf{D}}^{(+)}(\mathbf{r},t)$ and $\hat{\mathbf{D}}^{(-)}(\mathbf{r},t)$ are the positive and negative frequency parts of the displacement field operator. In particular, the positive frequency part is:

$$\hat{\mathbf{D}}^{(+)}(\mathbf{r},t) = \int_{0}^{+\infty} \hat{\tilde{\mathbf{D}}}(\mathbf{r},\omega)e^{-i\omega t}d\omega = \int_{0}^{+\infty} d\omega \sqrt{\frac{\hbar\omega}{4\pi c\epsilon_0}}\mathbf{D}(\mathbf{r},\omega)e^{-i\omega t}\hat{a}(\mathbf{r},\omega) \tag{2.15}$$

and $\hat{\mathbf{D}}^{(-)}(\mathbf{r},t) = \hat{\mathbf{D}}^{(+)}(\mathbf{r},t)^\dagger$. The characteristics of the displacement field function at a given frequency ω are described by $\mathbf{D}(\mathbf{r},\omega)$, while $\hat{a}(\mathbf{r},\omega)$ and $\hat{a}^\dagger(\mathbf{r},\omega)$ are the annihilation and creation operators that destroy or create, respectively, a photon with angular frequency ω at the position $\mathbf{r}$. At this point, the displacement field operators of the pump, signal, and idler photons can be decomposed as:

$$\begin{cases} \hat{\mathbf{D}}_p(\mathbf{r},t) = \hat{\mathbf{D}}_p^{(-)}(\mathbf{r},t) + \hat{\mathbf{D}}_p^{(+)}(\mathbf{r},t) \\ \hat{\mathbf{D}}_s(\mathbf{r},t) = \hat{\mathbf{D}}_s^{(-)}(\mathbf{r},t) + \hat{\mathbf{D}}_s^{(+)}(\mathbf{r},t) \\ \hat{\mathbf{D}}_i(\mathbf{r},t) = \hat{\mathbf{D}}_i^{(-)}(\mathbf{r},t) + \hat{\mathbf{D}}_i^{(+)}(\mathbf{r},t) \end{cases} \tag{2.16}$$

Substituting these relations in Eq. (2.13) we find:

$$\hat{\mathcal{H}}_I(t) = \frac{1}{3}\int_{\mathcal{V}} \zeta^{(2)} \left[\hat{\mathbf{D}}_p^{(-)}(\mathbf{r},t) + \hat{\mathbf{D}}_p^{(+)}(\mathbf{r},t)\right]\left[\hat{\mathbf{D}}_s^{(-)}(\mathbf{r},t) + \hat{\mathbf{D}}_s^{(+)}(\mathbf{r},t)\right]\left[\hat{\mathbf{D}}_i^{(-)}(\mathbf{r},t) + \hat{\mathbf{D}}_i^{(+)}(\mathbf{r},t)\right] d^3\mathbf{r} \tag{2.17}$$

There are eight different terms with all possible coupling of three displacement field operators, however, it is possible to demonstrate that the only two terms which contribute to the summation are $\hat{\mathbf{D}}_p^{(+)}(\mathbf{r},t)\hat{\mathbf{D}}_s^{(-)}(\mathbf{r},t)\hat{\mathbf{D}}_i^{(-)}(\mathbf{r},t)$ and $\hat{\mathbf{D}}_p^{(-)}(\mathbf{r},t)\hat{\mathbf{D}}_s^{(+)}(\mathbf{r},t)\hat{\mathbf{D}}_i^{(+)}(\mathbf{r},t)$ while the other six terms are averaged out when the Hamiltonian is integrated over time [38]. It is thus possible to reduce the Eq. (2.17) in the following way:

$$\hat{\mathcal{H}}_I(t) = \frac{1}{3}\int_{\mathcal{V}} \zeta^{(2)}(\mathbf{r})\hat{\mathbf{D}}_p^{(+)}(\mathbf{r},t)\hat{\mathbf{D}}_s^{(-)}(\mathbf{r},t)\hat{\mathbf{D}}_i^{(-)}(\mathbf{r},t)d^3\mathbf{r} + \text{H.c.} \tag{2.18}$$

where H.c. stands for Hermitian conjugate. This interaction Hamiltonian is able to describe two processes: the sum frequency generation (SFG) and the spontaneous parametric-down conversion (SPDC) processes. The first of these two processes, SFG, operates in a contrary fashion to SPDC. It

involves the interaction of two photons with lower energy, resulting in the emission of one photon with higher energy. However, since we are interested in describing the SPDC, we focus only on the first term of Eq. (2.18), neglecting the H.c. part. Now, further simplifications can be adopted to write the interaction Hamiltonian operator in a more compact way.

The pump field, due to its high intensity, can be treated as a classical field. In this case, the quantum operator $\hat{\mathbf{D}}_p^{(+)}(\mathbf{r},t)$ assumes the form of a classical field $\mathbf{D}_p^{(+)}(\mathbf{r},t)$ and the destruction operator $\hat{a}(\mathbf{r},\omega)$ can be replaced by the complex amplitude $a(\omega_p) = s(\omega_p)\sqrt{N_p}$, where the spectral amplitude of the pump is represented by $s(\omega_p)$ (it must satisfy the condition $\int d\omega |s(\omega)|^2 = 1$) and N_p represents the number of pump photons per unit time.

$$\mathbf{D}_p^{(+)}(\mathbf{r},t) = \int_0^{+\infty} d\omega_p \sqrt{\frac{\hbar\omega}{4\pi c\epsilon_0}} \mathbf{D}_p(\mathbf{r},\omega_p) e^{-i\omega_p t} s(\omega_p)\sqrt{N_p} \tag{2.19}$$

These manipulations allow to rewrite the interaction Hamiltonian operator as

$$\begin{aligned}\hat{\mathcal{H}}_I(t) = \frac{1}{3}\left(\frac{\hbar}{4\pi c\epsilon_0}\right)^{\frac{3}{2}} \int_0^{+\infty}\int_0^{+\infty}\int_0^{+\infty} d\omega_p d\omega_s d\omega_i s(\omega_p)\sqrt{N_p\omega_p\omega_s\omega_i} e^{-i(\omega_p-\omega_s-\omega_i)t} \\ \times \int_{\mathcal{V}} d^3\mathbf{r}\zeta^{(2)}(\mathbf{r})\mathbf{D}_p(\mathbf{r},\omega_p)\mathbf{D}_s^*(\mathbf{r},\omega_s)\mathbf{D}_i^*(\mathbf{r},\omega_i)\hat{a}^\dagger(\mathbf{r},\omega_s)\hat{a}^\dagger(\mathbf{r},\omega_i)\end{aligned} \tag{2.20}$$

Now that we have derived the expression for the Hamiltonian in the SPDC process, we can proceed to describe the evolution of the pump photon after the interaction and subsequently derive an expression for the biphoton wave function of the downconverted photons.

2.2.2 Generation of a Two-Photon Field

The unitary evolution of the initial quantum state $|initial\rangle$, in the interaction picture, is given by:

$$|\Psi(t)\rangle = e^{-\frac{i}{\hbar}\int_0^t \hat{\mathcal{H}}_I(t')dt'}|initial\rangle \approx (\mathbb{I} - \frac{i}{\hbar}\int_0^t \hat{\mathcal{H}}_I(t')dt')|initial\rangle = |initial\rangle + |\Psi_{si}(t)\rangle \tag{2.21}$$

where in the second step we performed a first-order Taylor expansion. Each order n of the expansion corresponds to the generation of 2^n photons, while the zero-order is the non-interacting case: in this discussion, we neglect the contribution of multi-pairs production. For our scope, since we are interested in the study of SPDC, we focus only on the first-order term.

Before the interaction, the initial state of the signal and idler photons is $|initial\rangle = |0\rangle_s|0\rangle_i$. The two-photon state after the interaction is obtained by combining the Eq. (2.21) and 2.20:

$$\begin{aligned}|\Psi_{si}(t)\rangle = -\frac{i}{3\hbar}\left(\frac{\hbar}{4\pi c\epsilon_0}\right)^{\frac{3}{2}} \int_0^t dt' \int_0^{+\infty}\int_0^{+\infty}\int_0^{+\infty} d\omega_p d\omega_s d\omega_i s(\omega_p)\sqrt{N_p\omega_p\omega_s\omega_i} e^{-i(\omega_p-\omega_s-\omega_i)t'} \\ \times \int_{\mathcal{V}} d^3\mathbf{r}\zeta^{(2)}(\mathbf{r})\mathbf{D}_p(\mathbf{r},\omega_p)\mathbf{D}_s^*(\mathbf{r},\omega_s)\mathbf{D}_i^*(\mathbf{r},\omega_i)\hat{a}^\dagger(\mathbf{r},\omega_s)\hat{a}^\dagger(\mathbf{r},\omega_i)|0\rangle_s|0\rangle_i\end{aligned} \tag{2.22}$$

Here we can directly see the action of the two creation operators on the vacuum state $|0\rangle_s|0\rangle_i$:

$$\hat{a}^\dagger(\mathbf{r}_s,\omega_s)\hat{a}^\dagger(\mathbf{r}_i,\omega_i)|0\rangle_s|0\rangle_i = |\mathbf{r}_s,\omega_s\rangle_s|\mathbf{r}_i,\omega_i\rangle_i \tag{2.23}$$

where $|\mathbf{r}_s,\omega_s\rangle_s$ and $|\mathbf{r}_i,\omega_i\rangle_i$ represent the states of the signal and idler photons generated in this process.

Since the interaction time t is assumed to be much longer than the time required by the SPDC process to generate the photons, we can extend the integration time to $-\infty$ and $+\infty$ and the corresponding integral can be written as:

$$\int_{-\infty}^{+\infty} dt' e^{i(\omega_s+\omega_i-\omega_p)t'} \Longrightarrow \int_{-\infty}^{+\infty} dt' e^{i(\omega_s+\omega_i-\omega_p)t'} = 2\pi\delta(\omega_s+\omega_i-\omega_p) \tag{2.24}$$

This condition formally states the conservation of the energy: $\omega_p = \omega_s + \omega_i$.

The Eq. (2.22) can be further simplified using the results found in Eqs. (2.23) and (2.24):

$$\begin{aligned} |\Psi_{si}(t)\rangle = -\frac{2\pi i}{3\hbar}\left(\frac{\hbar}{4\pi c\epsilon_0}\right)^{\frac{3}{2}} \int_0^{+\infty}\int_0^{+\infty}\int_0^{+\infty} d\omega_p d\omega_s d\omega_i s(\omega_p)\delta(\omega_s+\omega_i-\omega_p) \\ \times\sqrt{N_p\omega_p\omega_s\omega_i}e^{-i(\omega_p-\omega_s-\omega_i)t'}\int_{\mathcal{V}} d^3\mathbf{r}\zeta^{(2)}(\mathbf{r})\mathbf{D}_p(\mathbf{r},\omega_p)\mathbf{D}_s^*(\mathbf{r},\omega_s)\mathbf{D}_i^*(\mathbf{r},\omega_i)\,|\mathbf{r}_s,\omega_s\rangle_s\,|\mathbf{r}_i,\omega_i\rangle_i = \\ = -\int_0^{+\infty}\int_0^{+\infty} d\omega_s d\omega_i \psi(\omega_s,\omega_i)\,|\mathbf{r}_s,\omega_s\rangle_s\,|\mathbf{r}_i,\omega_i\rangle_i \end{aligned} \tag{2.25}$$

where in the last step we have defined the biphoton spectral distribution $\psi(\omega_s,\omega_i)$ which can be rewritten up to a complex phase as:

$$\psi(\omega_s,\omega_i) := \frac{2\pi}{3\hbar}\left(\frac{\hbar}{4\pi c\epsilon_0}\right)^{\frac{3}{2}}\sqrt{(\omega_s+\omega_i)\omega_s\omega_i}\,s(\omega_s+\omega_i)\mathcal{O}(\omega_s,\omega_i) \tag{2.26}$$

where the spatial overlap of pump, signal, and idler modes in the medium is represented by the following quantity:

$$\mathcal{O}(\omega_s,\omega_i) := \int_{\mathcal{V}} d^3\mathbf{r}\zeta^{(2)}(\mathbf{r})\mathbf{D}_p(\mathbf{r},\omega_p)\mathbf{D}_s^*(\mathbf{r},\omega_s)\mathbf{D}_i^*(\mathbf{r},\omega_i) \tag{2.27}$$

which strictly depends on the particular modal expansion of displacement vector fields of the pump, signal, and idler photons. At this point, in order to assess the spectral distribution of the emitted photons (Eq. (2.26)), we need to incorporate the spatial modes $\mathbf{D}_p(\mathbf{r},\omega_p)$, $\mathbf{D}_s(\mathbf{r},\omega_s)$, and $\mathbf{D}_i(\mathbf{r},\omega_i)$ of the pump, signal, and idler fields.

2.2.3 Gaussian Beams Treatment

In the experiment described in this work of thesis, the pump is derived from a laser beam in a Gaussian mode. Additionally, the signal and idler modes are collected using single-mode optical fibers, which are designed to ideally select Gaussian modes. As a consequence, for the subsequent calculations, the spatial modes of the pump, signal, and idler photons are assumed to be Gaussian beams. The electric field of a linearly polarized paraxial Gaussian beam propagating along the z-axis focused at the origin of the reference system can be written as[2]:

$$\mathbf{E}(\mathbf{r}) = \frac{\mathbf{e}}{\sqrt{\pi/2}}\frac{w}{q}\exp\left\{-\frac{x^2+y^2}{q}+ikz\right\} \tag{2.28}$$

where w is the waist size, $\mathbf{e}$ is the polarization versor, $q = w^2 + 2iz/k$, $k = \frac{n\omega}{c}$ is the wavenumber in the medium, and n is the refractive index of the medium along the direction defined by the polarization versor. The relation between the displacement vector field and the electric vector field is given by Eq. (2.2). In particular, neglecting the higher-order terms of the susceptibility tensor we have

$$\mathbf{D}(\mathbf{r}) \approx \epsilon_0(1+\chi^{(1)})\mathbf{E}(\mathbf{r}) = \epsilon_0 n^2\mathbf{E}(\mathbf{r}) \tag{2.29}$$

where in the second step we used the known relation between the refractive index and the linear susceptibility $n = \sqrt{1+\chi^{(1)}}$. In this case (as described in Sec. 2.2.4) the three photons are linearly polarized along two crystallographic axes (z-axis for signal and y-axis for pump and idler). The displacement vector field of each beam can be written as:

$$\mathbf{D}_\mathbf{k}(\mathbf{r}) = \frac{\epsilon_0 n_k^2\mathbf{e}_\mathbf{k}}{\sqrt{\pi/2}}\frac{w}{q}\exp\left\{-\frac{x^2+y^2}{q}+ikz\right\} \tag{2.30}$$

with $k = p,s,i$ and $n_p = n_i$.

[2]Here and in the following calculations, we will often use the notations of R. Bennink [39].

A further simplification of the spatial mode overlap in Eq. (2.27) is given by the tensorial product of the term $\zeta^{(2)}(\mathbf{r})\mathbf{e_p}\mathbf{e_s}\mathbf{e_i} = \zeta^{(2)}_{eff}(\mathbf{r})$. This quantity is defined as the effective inverse susceptibility and depends on the polarization of the photons and the type of material. The most commonly reported quantity in the literature is the susceptibility tensor $\chi^{(2)}$, as it is the one that can be experimentally measured. The effective inverse electric susceptibilities can be related to the effective susceptibilities using the approximation [36, 40]:

$$\zeta^{(2)}_{eff}(\mathbf{r}) \approx -\frac{\chi^{(2)}_{eff}(\mathbf{r})}{\epsilon_0^2 n_p^2 n_s^2 n_i^2} \tag{2.31}$$

where the effective susceptibility, similarly to the effective inverse susceptibility, is defined as $\chi^{(2)}_{eff}(\mathbf{r}) = \chi^{(2)}(\mathbf{r})\mathbf{e_p}\mathbf{e_s}\mathbf{e_i}$. At this point we are able to rewrite the spatial mode overlap (Eq. (2.27)), using the Gaussian modes introduced in Eq. (2.30) and the effective inverse susceptibility in Eq. (2.31):

$$\mathcal{O}(\omega_s, \omega_p) = \epsilon_0 \frac{w_p w_s w_i}{(\pi/2)^{\frac{3}{2}}} \int_{\mathcal{V}} \frac{dxdydz}{q_p q_s^* q_i^*} \chi^{(2)}_{eff}(\mathbf{r}) \exp\left[-(x^2+y^2)\left(\frac{1}{q_p} + \frac{1}{q_s^*} + \frac{1}{q_i^*}\right) + i\Delta k\, z\right] \tag{2.32}$$

where we introduced the quantity $\Delta k = k_p - k_s - k_i$ which is called wavevector (or momentum) mismatch [33] and it represents the variation of the total momentum between the generated photons and the initial pump photon along the z-axis.

2.2.4 Phase-Matching

The SPDC process is heavily influenced by the principles of momentum and energy conservation. It involves the generation of two photons with specific frequencies, ω_s and ω_i, and their probability distribution is determined by the squared modulus of the biphoton wave function in Eq. (2.26). To proceed with the calculations, the first crucial step involves solving the spatial integral in Eq. (2.32). We begin by assuming that the spatial variation of the effective nonlinear coefficient $\chi^{(2)}_{eff}(\mathbf{r})$ can be considered negligible, approximating it as a constant ($\chi^{(2)}_{eff}$). The initial focus is on solving the integral specifically along the z-axis:

$$\int_{-L/2}^{L/2} e^{i\Delta k z} dz = L \frac{\sin\left(\Delta k \frac{L}{2}\right)}{\Delta k \frac{L}{2}} = L\ \mathrm{sinc}\left(\Delta k \frac{L}{2}\right) \tag{2.33}$$

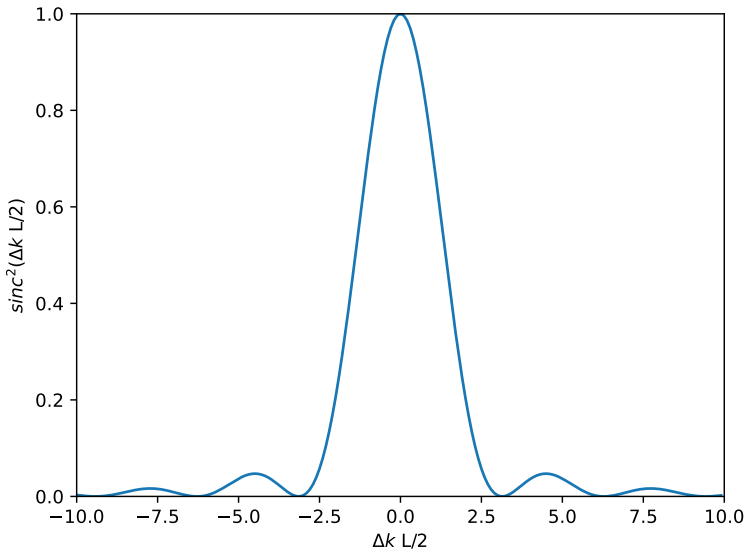

Figure 2.2: Plot of $\mathrm{sinc}^2\left(\Delta k \frac{L}{2}\right)$ contained in the spectral distribution $|\psi(\omega_s, \omega_i)|^2$.

The spectral distribution of the biphoton state is directly proportional to the spatial mode overlap $|\mathcal{O}(\omega_s, \omega_i)|^2$ (Eq.2.32), resulting in $|\psi(\omega_s, \omega_i)|^2 \propto \text{sinc}^2\left(\Delta k \frac{L}{2}\right)$. The behavior of the sinc^2 function (as shown in Fig. 2.2) reaches its maximum when the momentum mismatch $\Delta k = 0$, rapidly declining to zero when this condition is not met. This particular trend arises due to the finite integration range of Eq. (2.33), which is constrained by the crystal's finite length. In the limit of an infinitely large crystal, it approaches a Dirac's delta distribution. Based on these considerations, as expected, the emitted photons that satisfy the momentum conservation condition $\Delta k = 0$ are strongly favored[3].

The wavenumber in a medium is given by $k = \frac{2\pi n}{\lambda}$, where n is the refractive index and λ is the wavelength. In the case of anisotropic crystals, the refractive indexes vary with different crystallographic axes. Furthermore, these refractive indexes also depend on the wavelength of the incident radiation. Consequently, in the collinear SPDC process, the phase-matching condition, which encompasses both momentum and energy conservation, can be expressed as follows:

$$\begin{cases} \frac{n_p(\lambda_p)\omega_p}{c} = \frac{n_s(\lambda_s)\omega_s}{c} + \frac{n_i(\lambda_i)\omega_i}{c} \\ \omega_p = \omega_s + \omega_i \end{cases} \tag{2.34}$$

The phase-matching condition is challenging to satisfy since the refractive indexes of many media monotonically decrease with the wavelength of the photons. For instance, let's consider a situation where $\omega_p = 2\omega_s = 2\omega_i$, resulting in $n(\lambda_s) = n(\lambda_i)$. In this case, Eq. (2.34) can be simplified to:

$$\frac{n(\lambda_p)\omega_p}{c} = 2\frac{n(\lambda_s)\omega_s}{c} \tag{2.35}$$

However, this equation leads to the condition $n(\lambda_p) = n(\lambda_s)$, which is clearly not possible since $\lambda_p < \lambda_s$ (we expect $n(\lambda_p) > n(\lambda_s)$). More generally (as discussed in Boyd [33]), let's consider three photons with angular frequencies $\omega_s \leq \omega_i \leq \omega_p$ which constrain the values of the refractive indexes to be $n_s \leq n_i \leq n_p$. The first condition in Eq. (2.34) can be rewritten as:

$$n_p = \frac{n_s\omega_s + n_i\omega_i}{\omega_p} \tag{2.36}$$

By subtracting n_i from both sides and using the second condition of Eq. (2.34), we obtain:

$$n_p - n_i = \frac{n_s\omega_s + n_i\omega_i - n_i\omega_p}{\omega_p} = \frac{n_s\omega_s + n_i(\omega_i - \omega_p)}{\omega_p} = (n_s - n_i)\frac{\omega_s}{\omega_p} \tag{2.37}$$

This equation cannot be satisfied since the first term is positive while the second term is negative. One way to address this challenge is by leveraging the birefringence commonly found in anisotropic crystals. In such media, the refractive indexes are polarization-dependent for the transmitted radiation. By carefully selecting the crystal's orientation, it becomes possible in certain cases to optimize it in a way that satisfies the phase-matching condition in Eq. (2.34) for a specific combination of wavelengths and polarizations of the pump, signal, and idler photons.

An important category of anisotropic birefringent crystals is the uniaxial crystals, such as BiBO, which exhibit two refractive indexes referred to as *ordinary* (n_o) and *extraordinary* (n_e). Typically, the pump photons, having the highest frequency, are polarized along the direction that corresponds to the lowest refractive index. The remaining photons can be polarized in two different ways. In 1965, Midwinter and Warner [41] classified them into two classes (see Tab. 2.1):

- Type-I: The generated photons have the same polarization.
- Type-II: The generated photons are polarized along two orthogonal directions.

Another important category of nonlinear crystals employed for SPDC sources are the biaxial crystals, such as KTP. Biaxial crystals possess three distinct refractive indexes. Due to this property, it

[3]Note that the momentum conservation is expressed with a less restrictive condition, unlike the energy conservation, which is represented by $\delta(\omega_p - \omega_s - \omega_i)$.

	Positive uniaxial ($n_e > n_o$)	Negative uniaxial ($n_e < n_o$)
Type-I	$n_p^o\omega_p = n_s^e\omega_s + n_i^e\omega_i$	$n_p^e\omega_p = n_s^o\omega_s + n_i^o\omega_i$
Type-II	$n_p^o\omega_p = n_s^o\omega_s + n_i^e\omega_i$	$n_p^e\omega_p = n_s^e\omega_s + n_i^o\omega_i$
	$n_p^o\omega_p = n_s^e\omega_s + n_i^o\omega_i$	$n_p^e\omega_p = n_s^o\omega_s + n_i^p\omega_i$

Table 2.1: Phase-matching in uniaxial crystals.

becomes easier to achieve the phase-matching condition, as it requires less birefringence compared to uniaxial crystals. The nomenclature of the possible phase-matching conditions presented in Tab. 2.1 remains valid but with an increased number of combinations due to the presence of three refractive indexes. In uniaxial crystals, the refractive index of the ordinary wave is independent of the angle θ between the wavevector and the optical axis. However, the orientation of the wavevector affects the extraordinary refractive index $n_{eff}(\theta)$ [26]:

$$\frac{1}{n_{eff}^2(\theta)} = \frac{\cos^2\theta}{n_o^2} + \frac{\sin^2\theta}{n_e^2} \tag{2.38}$$

In biaxial crystals, all the refractive indexes depend on the orientation of the wavevector. In such situations, achieving phase-matching requires precise alignment of the crystal's optical axis with respect to the pump beam. Furthermore, the refractive indexes in these crystals are frequently highly temperature-dependent, making temperature tuning a critical factor that must be taken into consideration to achieve optimal phase-matching in a wide range of applications.

2.2.5 Quasi-Phase-Matching

The previous techniques to achieve the phase-matching condition can be difficult to be practically realized: the crystal could be not birefringent or its birefringence could be insufficient to satisfy the phase-matching condition of Eq. (2.34). When the birefringence of the crystal is inadequate to achieve complete phase-matching, the widely used technique is quasi-phase-matching. This method involves the use of periodically poled (PP) crystals that are structured with multiple layers, and the optical axes are oriented in a periodic manner. The period of alternation of the crystallographic axis is called *poling* (Λ) (see Fig. 2.3).

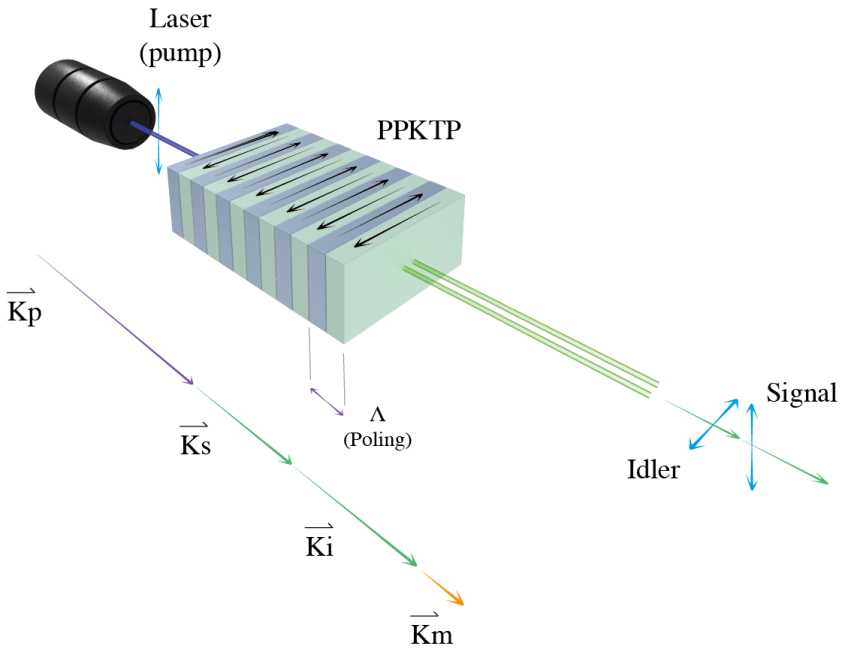

Figure 2.3: Schematic representation of the SPDC process in a periodically poled crystal. The m-order quasi-phase-matching is achieved by the additional wavevector $k_m = \frac{2\pi m}{\Lambda}$ which depends on the poling period Λ.

A detailed mathematical description of this technique is presented by R. Boyd [33]. While in a bulk crystal, the effective susceptibility can be approximated to a constant $\chi^{(2)}_{eff}$, in a periodically poled crystal, the effective susceptibility is alternately inverted for each layer. Mathematically, its spatial dependence can be described as a square wave along the z-axis.

$$\chi^{(2)}(z) = \chi^{(2)}_{eff}\text{sign}\left[\cos\left(\frac{2\pi z}{\Lambda}\right)\right] \tag{2.39}$$

It is usefut to rewrite the spatial dependence of $\chi^{(2)}(z)$ using the Fourier series:

$$\chi^{(2)}(z) = \chi^{(2)}_{eff}\sum_{m=\infty}^{+\infty} G_m e^{ik_m z} \tag{2.40}$$

where $k_m = \frac{2\pi m}{\Lambda}$ is the wavevector associated with the m-th Fourier coefficient along the z-axis, while the coefficient factors G_m are given by:

$$G_m = \frac{2}{m\pi}\sin\left(\frac{m\pi}{2}\right) \tag{2.41}$$

As the value of m increases, the coefficients G_m decrease. The first-order coefficient G_1 is the dominant term, with $G_1 = \frac{2}{\pi}$. Therefore, the effective susceptibility in a periodically poled crystal can be approximated by stopping the Fourier expansion in Eq. (2.40) at the first order:

$$\chi^{(2)}(z) = \chi^{(2)}_{eff}\frac{2}{\pi}e^{i\frac{2\pi}{\Lambda}z} \tag{2.42}$$

Finally, by substituting the expression of the effective susceptibility (Eq. (2.42)) into the spatial mode overlap (Eq. (2.32)), we obtain:

$$\mathcal{O}(\omega_s,\omega_p) = \epsilon_0\chi^{(2)}_{eff}\frac{2}{\pi}\frac{w_p w_s w_i}{(\pi/2)^{\frac{3}{2}}}\int_{\mathcal{V}}\frac{dxdydz}{q_p q_s^* q_i^*}\exp\left[-(x^2+y^2)\left(\frac{1}{q_p}+\frac{1}{q_s^*}+\frac{1}{q_i^*}\right)+i\left(\Delta k+\frac{2\pi}{\Lambda}\right)z\right] \tag{2.43}$$

In this scenario, the wavevector mismatch becomes $\Phi = \Delta k + \frac{2\pi}{\Lambda}$. In such cases, we have the flexibility to adjust the phase-matching by choosing an appropriate poling period Λ that satisfies the following conditions:

$$\begin{cases}\frac{n_p(\lambda_p)\omega_p}{c} - \frac{n_s(\lambda_s)\omega_s}{c} - \frac{n_i(\lambda_i)\omega_i}{c} + \frac{2\pi}{\Lambda} = 0\\ \omega_p = \omega_s + \omega_i\end{cases} \tag{2.44}$$

2.3 Performance Parameters of an SPDC Source

We are now able to explicitly derive the biphoton wave function. Much of the notation and calculations in this section are based on R. Bennink's work [39]. To begin, we simplify Eq. (2.43) by integrating over x and y:

$$\mathcal{O}(\omega_s,\omega_p) = \epsilon_0\sqrt{\frac{32}{\pi^3}}\chi^{(2)}_{eff}w_p w_s w_i\int_{-L/2}^{L/2}dz\frac{\exp\left[i(\Delta k+\frac{2\pi}{\Lambda})z\right]}{q_s^*q_i^*+q_pq_i^*+q_pq_s^*} \tag{2.45}$$

Furthermore, we need to consider the spectral amplitude of the pump beam $s(\omega)$. For a laser beam, we can approximate this quantity with a Gaussian profile [42]:

$$s(\omega_p) = \frac{\sqrt{\tau_p}}{\sqrt[4]{\pi}}e^{-\frac{\tau_p^2}{2}(\omega-2\omega_0)^2} \tag{2.46}$$

Here, τ_p represents the pulse duration, which is related to the coherence time of the laser, and $2\omega_0$ is the central frequency of the pump pulse. The multiplicative terms ensure that $\int|s(\omega)|^2d\omega = 1$, satisfying the normalization condition.

When the laser operates in a continuous wave (CW) regime, the pulse duration becomes infinitely long[4], and we can perform the following approximation:

$$|s(\omega)|^2 = \delta(\omega) \tag{2.47}$$

The biphoton wave function can be obtained from Eq. (2.26) using the expression for $\mathcal{O}(\omega_s, \omega_i)$ in Eq. (2.45) and the pump spectral amplitude from Eq. (2.46):

$$\psi(\omega_s, \omega_i) = \sqrt{\frac{2\hbar\epsilon N_p}{9\epsilon_0 \pi^4 c^3}} \sqrt{(\omega_s + \omega_i)\omega_s\omega_i}\, s(\omega_s + \omega_i) \chi^{(2)}_{eff} w_p w_s w_i \int_{-L/2}^{L/2} dz \frac{\exp\left[i(\Delta k + \frac{2\pi}{\Lambda})z\right]}{q_s^* q_i^* + q_p q_i^* + q_p q_s^*} \tag{2.48}$$

where ϵ is an experimental coefficient that quantifies the losses in this process due to the transmissivity of the crystal and the reflections that can occur inside it. The biphoton wave function is the fundamental ingredient for evaluating the performance parameters of SPDC, which include:

- **Brightness**
- **Heralding ratio**
- **Spectral purity**

These parameters are of significant importance in characterizing the performance of an SPDC source, as they are directly related to specific applications. In the following paragraphs, we will provide a more detailed description of these properties and how they are related to the wave function of downconverted photons.

2.3.1 Brightness

The first quantity that we can estimate from the biphoton wave function (Eq. (2.48)) is the joint spectral density $|\psi(\omega_s, \omega_i)|^2$ which corresponds to the expected number of photons pairs, per signal bandwidth per idler bandwidth, emitted into the Gaussian collection modes. As a consequence, the rate of pairs emitted by the source can be easily calculated by integrating over ω_s and ω_i the joint spectral density:

$$R_{\mathrm{si}} = \int_0^{+\infty} \int_0^{+\infty} |\psi(\omega_{\mathrm{s}}, \omega_{\mathrm{i}})|^2 \, d\omega_{\mathrm{s}} d\omega_{\mathrm{i}} \tag{2.49}$$

This quantity is called *brightness*. It is a crucial parameter in numerous applications, particularly in quantum communications, where it becomes significant due to the high losses encountered in various telecommunication channels. When the collected photons pass through spectral filters of narrow bandwidth, the effective brightness of the source is determined by integrating the joint spectral density over the range of frequencies covered by the filters.

2.3.2 Single-Photon Collection and Heralding Ratio

In certain applications of SPDC, the detection of a photon in the signal mode is used as an indication of the presence of a photon in the idler mode. However, even though photons are always emitted in pairs, they may be emitted in different spatial modes. Since the optical setup is designed to collect only Gaussian modes, there may be situations where only one of the two photons is collected. This can happen when one of the two photons is emitted in a Gaussian mode, while its partner is emitted into a different spatial mode and remains uncollected. These events reduce the number of effective entangled states produced by the source compared to the total number that each channel is capable of emitting. To quantify this, we can define the *heralding ratio* (or *heralding efficiency*), which estimates the probability that, once a photon (signal/idler) is emitted in a Gaussian mode, its partner is also emitted in the same mode. To start, let's define the rate of emission of photons in a Gaussian mode

[4] In our experimental setup, the pulse duration in CW becomes on the order of $\mathcal{O}(ns)$, whereas in the pulsed mode, it is on the order of $\mathcal{O}(ps)$. The difference between these time scales is significant enough to justify the following approximation.

regardless of the spatial mode of its partner as R_s (for signal) and R_i (for idler). The heralding ratios for signal (η_s) or idler (η_i) photons can be estimated as follows:

$$\eta_s = \frac{R_{si}}{R_s} \qquad \eta_i = \frac{R_{si}}{R_i} \tag{2.50}$$

To estimate the heralding ratios, we initiate the calculation of R_s and R_i. For now, let's focus on R_s. The approach is similar to what we used for estimating brightness, but in this case, the spatial mode overlap (Eq. (2.27)) is different since only the signal photon is emitted in a Gaussian mode. To characterize the spatial mode of the idler photon $\mathbf{D_i}(\mathbf{r})$, we can express it in terms of Laguerre-Gauss modes, which form an orthonormal basis set of solutions for the paraxial wave equation [39,43]. The spatial mode of the idler photon $\mathbf{D_i}^{(n,l)}(\mathbf{r})$ as a function of the associated Laguerre polynomial L_n^l is:

$$\mathbf{D_i}^{(n,l)}(\mathbf{r}) = \frac{\epsilon_0 n_i^2 \mathbf{e_i}}{\sqrt{\pi/2}} \left(\frac{w_i}{q_i}\right)^{l+1} \left(\frac{q_i^*}{q_i}\right)^n L_n^l \left(\frac{2w_i^2(x^2+y^2)}{|q_i|^2}\right) \exp\left[-\frac{x^2+y^2}{q_i} + ik_i z + il\phi\right] \tag{2.51}$$

where $\phi = \arctan\left(\frac{x}{y}\right)$. The Gaussian mode defined in Eq. (2.30) can be obtained by setting $n = l = 0$. As the pump and signal photons are emitted in Gaussian modes, which are azimuthally symmetric, the only contributions that do not vanish after the integration over the entire volume are the modes $\mathbf{D_i}^{(n,l)}(\mathbf{r})$ that are azimuthally symmetric as well. Hence, the possible modes of the idler photon are those that satisfy the condition $l = 0$. In particular, the spatial overlap now depends solely on n, and using an approach similar to the one described in Sec. 2.2.3, the n-order overlap is given by:

$$\begin{aligned}\mathcal{O}_n(\omega_s, \omega_p) = \epsilon_0 \chi^{(2)}_{eff} \frac{2}{\pi} \frac{w_p w_s w_i}{(\pi/2)^{\frac{3}{2}}} \int_{\mathcal{V}} \frac{dxdydz}{q_p q_s^* q_i^*} L_n^l \left(\frac{2w_i^2(x^2+y^2)}{|q_i|^2}\right) \\ \times \exp\left[-(x^2+y^2)\left(\frac{1}{q_p} + \frac{1}{q_s^*} + \frac{1}{q_i^*}\right) + i\left(\Delta k + \frac{2\pi}{\Lambda}\right)z\right]\end{aligned} \tag{2.52}$$

which can be further simplified by employing the Laguerre polynomial expansion. After simplification, we obtain:

$$\mathcal{O}_n(\omega_s, \omega_p) = \epsilon_0 \sqrt{\frac{32}{\pi^3}} \chi^{(2)}_{eff} w_p w_s w_i \int_{-L/2}^{L/2} dz \frac{\exp\left[i(\Delta k + \frac{2\pi}{\Lambda})z\right]}{q_s^* q_i^* + q_p q_i^* + q_p q_s^*} \left(\frac{q_s^* q_i + q_p q_i - q_p q_s^*}{q_s^* q_i^* + q_p q_i^* + q_p q_s^*}\right)^n \tag{2.53}$$

For the n-th idler mode, we have the correspondent spatial overlap $\mathcal{O}_n$ and thus a wave function $\psi_n(\omega_s, \omega_i)$ defined, similarly to Eq. (2.26), as:

$$\begin{aligned}\psi_n(\omega_s, \omega_i) = \frac{2\pi}{3\hbar} \left(\frac{\hbar}{4\pi c \epsilon_0}\right)^{\frac{3}{2}} \sqrt{(\omega_s + \omega_i)\omega_s \omega_i}\, s(\omega_s + \omega_i) \mathcal{O}_n(\omega_s, \omega_i) = \\ \sqrt{\frac{2\hbar \epsilon N_p}{9\epsilon_0 \pi^4 c^3}} \sqrt{(\omega_s + \omega_i)\omega_s \omega_i}\, s(\omega_s + \omega_i) \chi^{(2)}_{eff} w_p w_s w_i \\ \times \int_{-L/2}^{L/2} dz \frac{\exp\left[i(\Delta k + \frac{2\pi}{\Lambda})z\right]}{q_s^* q_i^* + q_p q_i^* + q_p q_s^*} \left(\frac{q_s^* q_i + q_p q_i - q_p q_s^*}{q_s^* q_i^* + q_p q_i^* + q_p q_s^*}\right)^n\end{aligned} \tag{2.54}$$

It is straightforward to verify that if $n = 0$, we obtain the biphoton wave function obtained in Eq. (2.48). The signal rate R_s is given by:

$$R_s = \int_0^{+\infty} \int_0^{+\infty} \sum_{n=0}^{+\infty} |\psi_n(\omega_s, \omega_i)|^2 d\omega_s d\omega_i \tag{2.55}$$

Using the above expression, we can calculate the signal heralding ratio as given in Eq. (2.50). Similarly, the idler rate R_i can be obtained by interchanging the labels s and i everywhere.

2.3.3 Spectral Purity

The *spectral purity* of an SPDC source refers to how well the generated photons are confined to a specific wavelength with a narrow bandwidth. In an ideal SPDC process, all generated photons would have the exact same wavelength, resulting in a perfectly pure spectral state. However, in practice, the SPDC process can lead to some broadening of the photon's spectral bandwidth due to factors like the characteristics of the pump beam and the pulse duration. The spectral purity of an SPDC source is crucial for various applications, particularly those that rely on interference between nominally identical sources. These applications include generating multiphoton entangled states for quantum computing [44] and utilizing quantum properties like the Hong-Ou-Mandel [45] or Bell-state measurements [46].

To quantify spectral purity, one can calculate the spectral bandwidth of the emitted photons. A lower spectral bandwidth corresponds to higher spectral purity, indicating that the photons are confined to a narrower range of frequencies. Alternatively, spectral purity can be quantified in terms of the degree of spectral entanglement between the signal and idler frequencies, providing a more quantitative measure of its quality. In this case, the spectral purity is expressed as:

$$\rho = \frac{\sum_j \sigma_j^2}{(\sum_j \sigma_j)^2} \tag{2.56}$$

where σ_j are the eigenvalues of the Schmidt decomposition of the biphoton wave function, which can be written as:

$$\psi(\omega_s, \omega_i) = \sum_j \sqrt{\sigma_j} u_j(\omega_s) v_j(\omega_i) \tag{2.57}$$

This formula is analogous to Eq. (1.53), but with ω_s and ω_i treated as continuous variables. To find the values of σ_j, u_j, and v_j, one can solve the corresponding eigenvalue equations [47].

$$\begin{aligned} \int K_1(\omega, \omega') u_j(\omega') d\omega' &= \sigma_j u_j(\omega) \\ \int K_2(\omega, \omega') v_j(\omega') d\omega' &= \sigma_j v_j(\omega) \end{aligned} \tag{2.58}$$

where:

$$\begin{aligned} K_1(\omega, \omega') &= \int \psi(\omega, \omega_i) \psi^*(\omega', \omega_i) d\omega_i \\ K_2(\omega, \omega') &= \int \psi(\omega_s, \omega) \psi^*(\omega_s, \omega') d\omega_s \end{aligned} \tag{2.59}$$

The spectral purity and spectral entanglement of the signal and idler photons are inversely related. When a state is separable, it has only one eigenvalue, $\sigma = 1$, indicating no spectral entanglement. As a result, the spectral purity reaches its maximum value, namely $\rho = 1$.

2.4 Optimization of the Source Performances

The performance parameters listed above strictly depend on the focussing condition of pump, signal, and idler photons inside the crystal that can be expressed in terms of the waists of the corresponding beams w_p, w_s and w_i. These quantities play a key role in the biphoton wave function and, as a consequence, they deeply affect all the properties previously described of an SPDC source. The analysis of these properties can be used to predict the optimal source configuration to maximize its performance, which could depend on the practical application. The most interesting result in the work of Bennink [39] consists in the description of a procedure to optimize the individual properties varying the focusing conditions. Some of these properties can be jointly optimized while others require a trade-off.

To simplify the notation, Bennink introduced an adimensional variable, called *focal parameter* defined as

$$\xi_j \equiv \frac{L}{k_j w_j^2} \tag{2.60}$$

where L is the crystal length, w_j the waist and $k_j = \frac{\omega n_j}{c}$ is the wavenumber of the field j ($j = p, s, i$) in the medium. For $\xi_j \gg 1$ ($\xi_j \ll 1$) the beam is strongly (weakly) focused in the crystal.

In order to simplify the computations, Bennink rewrote the biphoton wave function Eq. (2.48) in terms of adimensional quantities, which are defined as follows:

$$A_\pm(\omega_s, \omega_i) = 1 + \frac{k_s}{k_p}\frac{\xi_s}{\xi_p} \pm \frac{k_i}{k_p}\frac{\xi_i}{\xi_p} \tag{2.61}$$

$$B_\pm(\omega_s, \omega_i) = \left(1 - \frac{\Delta k}{k_p}\right)\left(1 + \frac{k_s + \Delta k}{k_p - \Delta k}\frac{\xi_p}{\xi_s} \pm \frac{k_i + \Delta k}{k_p - \Delta k}\frac{\xi_p}{\xi_i}\right) \tag{2.62}$$

$$C(\omega_s, \omega_i) = \frac{\Delta k}{k_p}\frac{\xi_p^2}{\xi_s \xi_i}\frac{A_+}{B_+} \tag{2.63}$$

$$\xi(\omega_s, \omega_i) = \frac{B_+}{A_+}\frac{\xi_s \xi_i}{\xi_p} \tag{2.64}$$

The frequency dependence is incorporated through the wavenumbers k_j and focal parameters ξ_j. In this way, the biphoton wave function can be written as:

$$\begin{aligned}\psi(\omega_s, \omega_i) = \sqrt{\frac{n_s(\omega_s) n_i(\omega_i) E_p \epsilon L}{n_p(\omega_s + \omega_i)\epsilon_0 \omega_0}} \frac{\omega_s \omega_i \chi^{(2)}_{eff} s(\omega_s + \omega_i)}{6\pi^2 c^2} \frac{1}{\sqrt{A_+(\omega_s, \omega_i) B_+(\omega_s, \omega_i)}} \\ \times \int_{-1}^{1} dl \frac{\sqrt{\xi(\omega_s, \omega_i)}\exp\{i\Phi l/2\}}{1 - i\xi(\omega_s, \omega_i) - C\xi^2(\omega_s, \omega_i) l^2}\end{aligned} \tag{2.65}$$

where we have rewritten the number of pump photons incident on the crystal per unit time in terms of the corresponding energy E_p as $N_p = \frac{E_p}{2\hbar\omega_0}$, where ω_0 represents the angular frequency of the emitted photons (the energy of a pump photon is given by $2\hbar\omega_0$). The phase mismatch is denoted as $\Phi = \Delta k + \frac{2\pi}{\Lambda}$. From this notation, we observe that $|\psi(\omega_s, \omega_i)|^2 \propto L$, indicating that the brightness also linearly scales with the length of the crystal.

With these notations, we can proceed with the optimization procedure, relying on the following approximations:

1. We can assume that the momentum mismatch Δk is much smaller than k_j. This assumption arises from the fact that when $\Delta k + \frac{2\pi}{\Lambda} = 0$, the SPDC process is maximized. Consequently, we can approximate $\Delta k \approx -\frac{2\pi}{\Lambda}$, which is typically much smaller than k_j. Based on this approximation, we find:

$$1 \pm \frac{\Delta k}{k_j} \approx 1 \tag{2.66}$$

$$C \approx 0 \tag{2.67}$$

2. The frequency dependence of $\psi(\omega_s, \omega_i)$ (Eq. (2.65)) is mainly determined by the pump spectrum $s(\omega_s + \omega_i)$ and the frequency dependence of the momentum mismatch Δk. We can assume that near phase-matching conditions:

$$A_\pm, B_\pm, \xi_j, \sqrt{\frac{n_s n_i}{n_p}}\chi^{(2)}_{eff}\omega_s\omega_i \approx \text{const} \tag{2.68}$$

   For this relationship to hold, the bandwidths of the photons must be significantly smaller than the optical frequency.

3. Another important assumption for the calculations is the approximately linear frequency dependence of Δk:

$$\delta k_j \approx \frac{n_j'}{c}\delta\omega_j \tag{2.69}$$

   where $n_j' \equiv c\,\partial k_j/\partial\omega$ and $\delta\omega_j$ (δk_j) denotes a small variation from the nominal frequency (wavenumber) of mode j.

These approximations are valid for SPDC sources that have a crystal of length $L \gtrsim 1$ mm, refractive indexes $n \gtrsim 1.5$, a poling period $\Lambda \gtrsim 5\ \mu$m and the wavelength of the photons is $\lambda_p \lesssim 0.8\ \mu$m and $\lambda_{s,i} \lesssim 1.6\ \mu$m. In particular, the following optimization procedure has been performed with a reference source consisting of degenerate type-II SPDC in a PPKTP crystal with length $L = 10$ mm and a 750 nm pump beam (which is quite similar to the source realized in this thesis work) [39].

2.4.1 SPDC Optimization

Bennink optimizes four quantities as a function of the focal parameters ξ_p, ξ_s, and ξ_i: the peak of the joint spectral density, the brightness, the heralding ratio, and the spectral purity. The main result of this analysis is the identification of a trade-off optimal focusing condition, which maximizes the performance of the source.

Joint spectral density

The primary objective is to maximize the amplitude of the peak of the joint spectral density. A well-defined peak in the spectral distribution typically corresponds to a narrow bandwidth. This characteristic becomes particularly important in certain applications where narrow filters are employed to reduce the bandwidth of emitted photons. In such scenarios, a broader spectral distribution would significantly reduce the brightness, which is obtained by integrating the spectral distribution over a limited range of frequencies. Exploiting the approximations mentioned before (Eqs. (2.66), (2.67), (2.68)), one can optimize the peak of the joint spectral density with respect to $(\xi_p, \xi_s, \xi_i, \Phi)$, given by $\max_{(\xi_p,\xi_s,\xi_i,\Phi)} |\psi(\omega_s, \omega_i)|^2$. The maximum value is obtained when (refer to Fig. 2.4):

$$\xi_s \approx \xi_i \approx \xi_p \approx 2.84 \tag{2.70}$$

$$\Phi \approx -1.04\pi \tag{2.71}$$

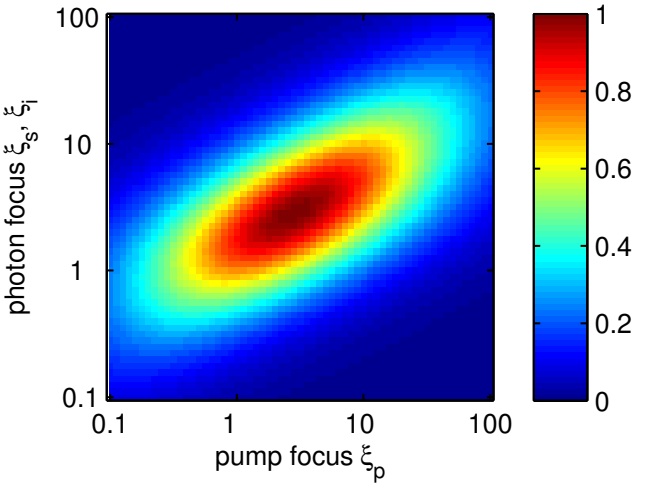

Figure 2.4: Peak of the joint spectral density, normalized to the global maximum, as a function of the pump, signal, and idler focal parameters [39].

Brightness

In numerous applications, the use of narrow filters may not be necessary, and instead, it is preferable to employ only broadband spectral filters to effectively filter noise. Therefore, in such cases, the primary focus lies in maximizing the brightness rather than the joint spectral density peak. By employing the approximation $C \approx 0$, there are no finite values of ξ_p, ξ_s, and ξ_i that can maximize R_{si}. The brightness indeed grows with increasing field focusing. However, at high focusing one can demonstrate that the approximation $C \approx 0$ is not valid anymore and the brightness is upper bounded. If we consider the condition where the signal and idler focal parameters are fixed $(\xi_s = \xi_i)$, which is quite common in many SPDC sources, the optimal focusing for the pump is given by $\xi_p = \xi_s (= \xi_i)$. On the other hand, if we fix ξ_p, then the optimal value of ξ_s is nearly equal to ξ_p when $\xi_p \gtrsim 10$, and it is slightly larger than ξ_p when $\xi_p \lesssim 10$. The relationship of R_{si} with ξ_p and $\xi_s = \xi_i$ is shown in Fig. 2.5.

Heralding ratio

In a similar manner to R_{si}, the local maximization of R_s occurs when $\xi_s \approx \xi_p$ (see Fig. 2.5). However, compared to R_{si}, R_s exhibits slower variations with ξ_s and ξ_p (Fig. 2.6). The broader nature of R_s in comparison to R_{si} implies that collecting the signal in a non-optimal Gaussian mode will project the idler onto a mode that does not couple well to any Gaussian mode of any size, i.e., a non-Gaussian

mode. When setting $\xi_s = \xi_i = \xi_p$, which locally maximizes both R_{si} and R_s, the signal heralding ratio can be expressed simply as:

$$\eta_s = \frac{k_i}{k_p}\left(\frac{k_s}{k_p} + 1\right). \tag{2.72}$$

A similar expression exists for η_i. For near-degenerate SPDC, where $k_s \approx k_i \approx k_p/2$, these expressions give $\eta_s = \eta_i = 0.75$, and for the non-degenerate case, the values are less than 0.75. However, it is possible to achieve higher heralding ratios with different focusing conditions. The optimal source configuration concerning both heralding and brightness is not defined by a single set of parameter values but rather a curve in the parameter space. This curve has the property that η_s cannot be increased without decreasing R_{si}, and vice versa. Thus, there exists a trade-off between heralding efficiency and brightness in the optimization of the source configuration.

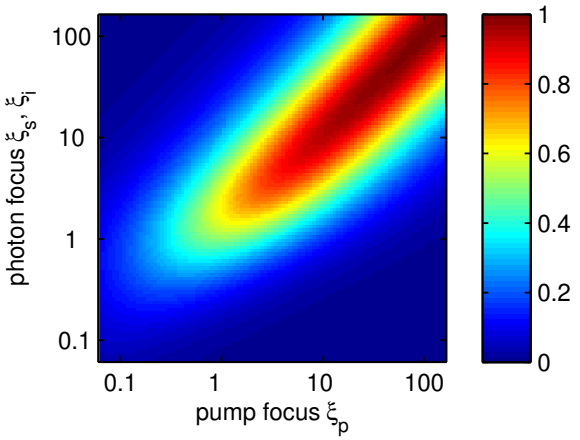

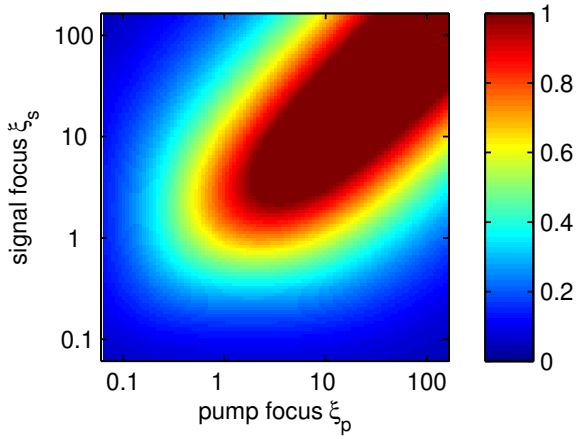

Spectral purity

Finally, it is intriguing to investigate the connection between spectral purity and beam focusing, in order to understand how this quantity is related to the brightness and the heralding ratio. Specifically, this parameter is associated with the factorability of $\psi(\omega_s, \omega_i) \propto u(\omega_s)v(\omega_i)$, which is achieved when the joint spectral density is narrow. Consequently, we observe a similar trend to that which maximizes the peak of the joint spectral density. Through numerical calculations, in the case where $\xi_p \approx \xi_s \approx \xi_i (= \xi)$, promoting high brightness and heralding ratios, an optimal value of $\xi \approx 2$ is obtained.

Optimal focusing condition

These quantities exhibit optimal values for different focal parameters, creating a trade-off between brightness and heralding ratio. As the pump is collimated ($\xi_p \to 0$), the signal heralding ratio η_s (and equivalently the idler heralding ratio η_i) approaches unity since all the photons are emitted in Gaussian modes. However, in this limit, the brightness is minimized, as it benefits from a highly focused pump beam. Additionally, spectral purity is optimized for $\xi \approx 2$. One of the most significant findings of this study is the existence of specific focusing conditions ($\xi_p, \xi_s, \xi_i \sim 2.5$) that simultaneously optimize brightness, heralding ratio, and spectral purity, bringing them close to their maximum values. This condition will be fundamental for the design and experimental realization of the SPDC source, leading to the selection of particular optical configurations.

Chapter 3

Design of the Experimental Apparatus

The realization of a polarization-entangled photon source requires the use of suitable instrumentation and a meticulous selection of constituent elements. In this chapter, we will provide an overview of the most important experimental tools employed to create and characterize the source, such as the pump laser Mira 900, the optical fibers, and the highly efficient single-photon detectors (SNSPD). Moreover, we will delve into the selection process for key elements used in the source, such as the PPKTP crystal and the focusing lenses for the pump, signal, and idler beams. Particular attention will be given to the design choices made for the source, as they significantly impact its performance. Although the general design based on the Sagnac interferometer is known in the literature, we made several optimizations for this specific case.

3.1 Pump Laser

A fundamental instrument for this experiment is the Mira 900 laser from Coherent (Fig. 3.2). This laser offers tunable wavelengths in the range from 700 nm to 1000 nm and can operate in both continuous wave (CW) and pulse mode. These features make it an ideal candidate as a pump photon source for the SPDC process.

The Mira 900 laser is a Ti:Sapphire laser, a type of solid-state laser that employs a titanium-doped sapphire crystal to convert light from a primary laser source into a different wavelength. This conversion is based on the principle of stimulated emission of photons. When the titanium-doped sapphire crystal is pumped with a laser operating at a specific wavelength (typically within the range of 527 nm to 532 nm), the electrons in the titanium ions become excited and move to higher energy levels. Upon returning to their lower energy states, these electrons emit photons in the red or infrared spectrum, which are then collected and amplified within the optical cavity.

The Mira 900 features a primary laser source known as *Verdi*, capable of delivering up to 18 W of power and emitting a continuous wave (CW) laser beam at 532 nm. This beam is subsequently directed through a series of mirrors towards the crystal, positioned within the Mira 900's cavity. Within the cavity, the laser beam undergoes the process of stimulated emission and optical amplification, which converts it into an infrared laser beam. This type of laser has two main features:

- **Wavelength tuning**: The Ti:Sapphire crystal possesses inherent dispersion characteristics, causing varying phase delays for different wavelengths of light. This property is used to carefully choose the wavelength of the emitted radiation. To achieve this, a prism is introduced into the laser cavity. This prism effectively separates the different wavelengths emitted by the crystal. By adjusting the orientation of the prism within the laser cavity, we can select the specific wavelength to be amplified and subsequently emitted by the laser. This tunability allows for precise selection of the desired wavelength, catering to the specific experimental requirements (as shown in Fig. 3.1, which depicts the laser's spectrum in the working configuration). To achieve this fine regulation experimentally, a micrometric screw is utilized to control the prism's inclination, enabling accurate tuning of the emitted wavelength.

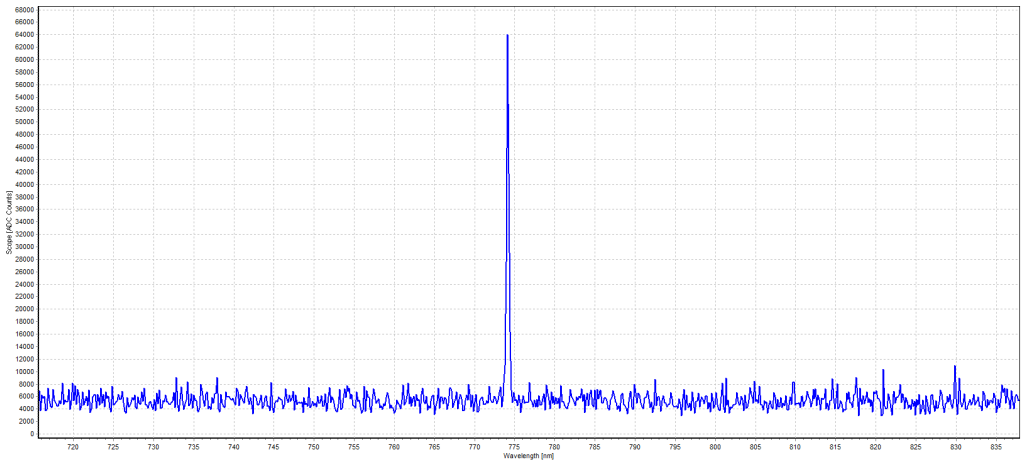

Figure 3.1: Spectrum of Coherent Mira 900 recorded with the spectrometer Avantes. The wavelength is tuned to 775 nm which is the working condition.

- **Ultrashort pulses**: This type of laser can generate ultrafast pulses using a technique called *mode-locking* [48]. The pulse duration τ_p (introduced in Eq. (2.46)) is defined as the inverse of the standard deviation of the laser spectral distribution[1]. The laser operates at a repetition rate of 76 MHz, and the pulse duration can vary depending on the specific cavity setup. There are three available configurations referred to as *femto* ($\tau_p \sim \mathcal{O}(100\,\text{fs})$, *pico-short* ($\tau_p \sim \mathcal{O}(1\,\text{ps})$), and *pico-long* ($\tau_p \sim \mathcal{O}(10\,\text{ps})$). For this particular experiment, the cavity has been adjusted to the pico-short configuration, and the experimental estimation of the pulse duration is approximately $\tau_p \approx 2.17$ ps. In a mode-locked laser, the light is constrained to a specific set of longitudinal modes or frequencies. These modes undergo constructive interference, resulting in the coherent superposition of their electric fields. This constructive interference causes the light intensity to rapidly build up, leading to the emission of ultrashort pulses. The specific mode-locking technique employed by Mira is known as *passive Kerr-lens mode-locking* [50]. This method involves incorporating a Kerr medium, typically a nonlinear optical crystal with a high Kerr nonlinearity, into the laser cavity. The Kerr effect is a phenomenon where the refractive index of a material changes in response to the intensity of light passing through it. Within this setup, the Kerr medium functions as a self-focusing lens. As the intensity of light increases, the refractive index of the medium also increases. Consequently, the laser pulses experience self-phase modulation, wherein the peak intensity of the pulse results in a higher refractive index, effectively acting as a lens that focuses the light. Conversely, as the intensity decreases towards the pulse's tail, the refractive index diminishes, leading to a defocusing effect. This self-focusing and defocusing behavior of the Kerr medium acts as a feedback mechanism, promoting the stabilization of the mode-locking process, facilitating the generation of ultrashort pulses. The term *passive* denotes that the mode-locking process does not rely on external elements like modulators or active feedback control systems. Instead, the self-phase modulation induced by the Kerr medium alone is adequate to initiate and maintain the mode-locking, making the system more straightforward.

The performance of the laser relies on various factors that are largely influenced by environmental conditions. The primary quantities to be controlled are temperature and air humidity. Many components of the laser exhibit temperature dependence and fluctuations in temperature can lead to expansion or contraction of the laser cavity's components.

The refractive index of the Ti:Sapphire material used in the laser changes with temperature, resulting in a wavelength drift in the laser emission. This becomes crucial in applications that demand

[1]The pulse duration τ_p can be derived by the coherence time τ_{coh} of the laser using the relation: $\tau_p = \pi\sqrt{2}\tau_{coh}$ [49]. This relation is useful because the coherence time is the quantity that is typically measured in the laboratory. We note that there are other frequently used quantities that are directly related to the pulse duration. For instance, the standard deviation of a (temporally and spectrally) Gaussian pulse is $\tau_p/4\pi$.

precise and stable laser wavelengths, as in the case of this experiment where the emission of 1550 nm photons occurs only within a narrow range of wavelengths centered at 775 nm. Temperature changes can further induce variations in the cavity resonance, leading to mode-hopping or mode competition in the laser output[2]. These unpredictable fluctuations affect the laser's emission characteristics, including the power of the beam. In pulse mode, such effects become more pronounced as even slight perturbations can disrupt this delicate condition. The optimal laser performance is achieved when the environment's temperature is around 20°C. Several systems are employed in the room to achieve and maintain this temperature as closely as possible.

Humidity is another significant factor that can impact the laser's performance. High humidity levels can cause water vapor to condense on optical elements, such as crystals and mirrors, leading to contamination and degradation of their optical surfaces. This type of fluctuation can have a more pronounced effect on mode-locking performance, further highlighting the importance of maintaining stable environmental conditions for the optimal laser operation.

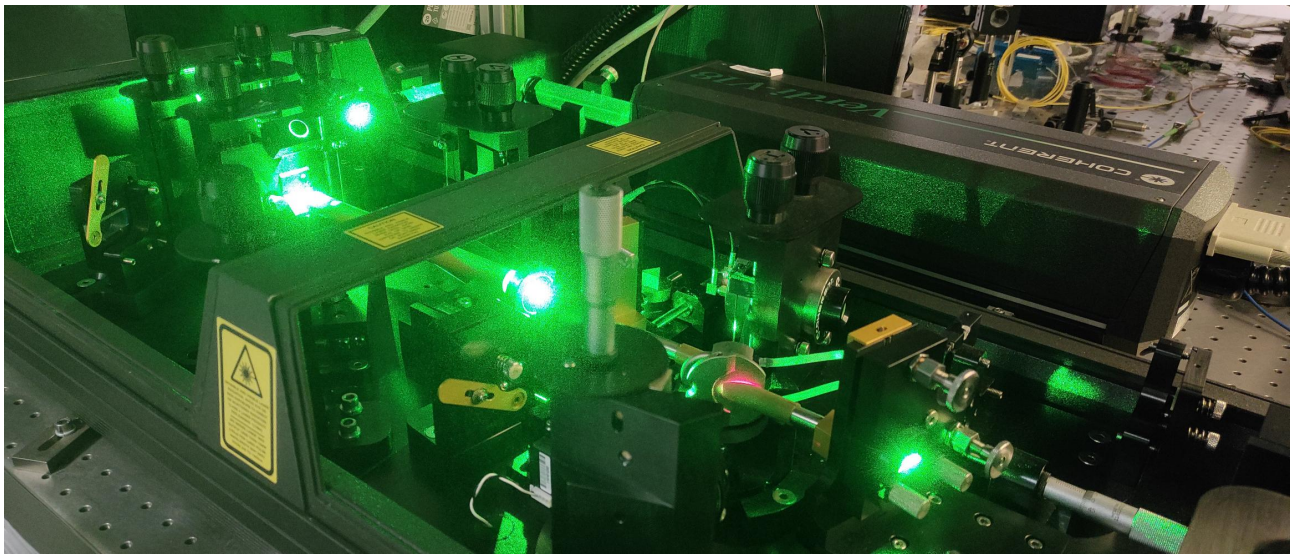

Figure 3.2: Photo of Mira's optical system. The green light is the pump laser from Verdi which interacts in the Ti:Sapphire crystal emitting an infrared wavelength tunable laser beam.

3.2 Optical Fibers

Optical fibers play a crucial role in modern telecommunications systems. An optical fiber typically consists of a core, where light propagates, and a cladding that surrounds the core. The core and cladding are made of different materials with different refractive indexes. When light enters the fiber, the refractive index difference between the core and cladding causes the fiber to act as a waveguide, guiding the light along its length through total internal reflection.

Different types of optical fibers exist, classified based on core material and diameter, which influences the mode of light propagation inside them. Two primary types of optical fibers are:

- **Single-mode fiber**: Single-mode fibers have a small core diameter, typically around $5 - 10$ μm. Their design is optimized to efficiently transport a single mode of light at a specific wavelength. This results in less dispersion and attenuation, making single-mode fibers suitable for long-distance communication and high-speed data transmission.

- **Multi-mode fibers**: Multi-mode fibers possess a larger core diameter, typically ≥ 30 μm. Their design enables them to carry multiple modes of light, allowing light to traverse through the core along various paths. However, this characteristic also leads to increased dispersion and attenuation, which restricts their maximum transmission distance and bandwidth.

[2]Mode-hopping in a laser refers to the phenomenon where the laser output switches between different longitudinal modes of the laser cavity.

The primary distinction between single-mode and multi-mode optical fibers lies in the modes of light that propagate within the fiber. In particular, single-mode fibers can collect and emit only the Gaussian mode of light, while multi-mode fibers can transmit different modes due to their larger core diameter. As a result, multi-mode fibers are easier to couple with external light sources.

Fiber coupling is the process of directing a light beam into the fiber, typically achieved using two mirrors. These mirrors are adjusted along the horizontal and vertical directions to precisely align the beam with the fiber's core and achieve the correct tilt, maximizing the light transmitted by the fiber.

The acceptance angle of an optical fiber is determined by the numerical aperture (NA), expressed as $\sin\theta$, where θ represents the maximum angle at which incident light can enter the fiber core while maintaining total internal reflection.

For single-mode fibers, an essential property is the mode field diameter (MFD), which characterizes the spatial distribution of light intensity within the fiber's core. The mode field diameter represents the size of the light beam supported by the fiber's core. It can be calculated using Marcuse's equation [51]:

$$MFD = 2a\left(0.65 + \frac{1.619}{V^{\frac{3}{2}}} + \frac{2.879}{V^6}\right) \tag{3.1}$$

where $V = \frac{2\pi}{\lambda}aNA$, with λ being the wavelength of the light, a the core radius, and NA the numerical aperture. The mode field diameter is important as it allows us to estimate the waist W of the Gaussian beam propagating along the fiber: $2W = MFD$.

In this thesis work, single-mode fibers were predominantly used to transmit signals. For instance, we employed them to carry the light from the laser to the source (for the 775 nm pump beam) and from the source to the detectors (for the 1550 nm emitted photons). The choice of single-mode fibers was not only due to the high light transmission but also their ability to select only the Gaussian mode, effectively acting as filters. For this experiment, we utilized two types of single-mode optical fibers, each suitable for a specific wavelength of light. The 780HP fiber was used for pump beam at 775 nm, while the SMF28 Ultra fiber was employed for the 1550 nm photons emitted by the source.

Optical fibers are susceptible to both thermal and mechanical effects, which can significantly influence their performance and reliability. Thermal effects encompass thermal expansion, changes in attenuation, thermal gradients, and thermal shock. On the other hand, mechanical effects include bending and microbending losses, tensile and compressive stress, vibration, and cable crush can deeply affect the transmissivity of the fiber. In addition to these losses, optical fibers can induce a change in the polarization of the input light. This effect is due to the intrinsic birefringence or asymmetry of the fiber, leading to the splitting of light into two orthogonal polarization modes. As light propagates through the fiber, these polarization modes experience different velocities, causing the light's polarization state to vary over time. This effect leads to a transformation of the quantum state of a photon, which can be described as a unitary transformation (a rotation on the Bloch sphere).

To address this issue, a potential solution is to use a *polarization controller*, a device that modifies the polarization of the light exiting the fiber by applying mechanical stress to the fiber. Alternatively, one can use a QWP and HWP before or after the optical fiber to compensate for the induced polarization transformation on the light state. These approaches help in maintaining the desired polarization state of the light and are useful in various quantum communication technologies.

3.3 Single-Photon Detectors

Superconducting nanowire single-photon detectors (SNSPDs) represent highly sophisticated photodetectors designed to detect individual photons with exceptional efficiency, minimal noise, and short dead time. When compared to traditional photodetectors like photomultiplier tubes or avalanche photodiodes, SNSPDs offer several distinct advantages. Their near-unity quantum efficiency allows them to detect a high percentage of incident photons, with very low dark count rates, minimizing false detections caused by thermal noise. Additionally, SNSPDs exhibit ultra-fast response times, enabling them to resolve photons with extremely short time intervals. These characteristics make SNSPDs invaluable in a wide range of applications, including quantum optics, quantum commu-

nication, quantum cryptography, and quantum information processing. Their ability to efficiently detect single photons has unveiled new prospects in quantum technology and fundamental research.

In this experiment, the detectors utilized belong to the ID281 Series from ID Quantique (a photo is shown in Fig. 3.3). This particular instrument comprises 7 available channels, each corresponding to a detector. The detection efficiency may vary across these channels and is influenced by the wavelength of the incident light. For this study, we focused on characterizing two specific channels (Ch. 5 and Ch. 8). To assess their efficiency at 1550 nm, a detailed procedure is provided in Appendix C.

The working principle of SNSPDs, as described by Gol'tsman, Semenov, and Young [52–54], can be summarized in the following steps (see Fig. 3.4 part (a)):

1. Initially, the superconducting wire is traversed by a constant current which is maintained by an external circuit. Given the material's property of zero resistance in the superconducting state, there is a null voltage between the two ends of the wire.

2. When a photon interacts with the wire, it releases sufficient energy to create a resistive hotspot within the medium, a phenomenon feasible within a specific range of wavelengths.

3. The resistive hotspot behaves as a normal conductor, while the rest of the wire remains in a superconducting state. This causes the supercurrent to bypass the newly formed resistive barrier.

4. The supercurrent density increases at the periphery of the hotspot. Due to the narrowness of the wire, the current density can attain the critical value at the hotspot's border, effectively expanding the dimensions of the resistive hotspot in the transverse direction.

5. The presence of resistance in the middle of the nanowire promotes Joule heating, rapidly spreading the resistive barrier throughout the entire wire, elevating the system's temperature above the critical temperature. The expansion of the resistive barrier causes a voltage increase across the nanowire. This voltage drop is then amplified and analyzed by specialized electronic systems, which identify it as an event.

6. Electrons start to diffuse away from the hotspot releasing their energy through electron-phonon interactions, consequently cooling the system and restoring it to its initial state (point 1).

The depicted diagram illustrates two characteristic times denoted as τ_1 and τ_2. τ_1 quantifies the duration required for the resistive hotspot, formed after the photon interaction, to encompass the entire wire. On the other hand, τ_2 represents the time taken by the detector to return to its initial state. After the detection of a photon, the detector is unable to register another signal for a specific period of time denoted as $t_d = \tau_1 + \tau_2$. This duration is commonly referred to as the *dead time*. During this period, the detector is recovering and resetting itself, making it temporarily unresponsive to subsequent photon interactions. The shape of the electric signal induced by the detector following the photon interaction is displayed in Fig. 3.4 part (c). This signal can be represented by an equivalent circuit comprising a kinetic inductance L_k and a variable resistance $R_n(t)$ (part (b)).

After being registered, the electric signal from the detector is amplified and subsequently fed into a time tagger. A time tagger is a crucial device employed in experimental setups to accurately measure and record the timing of events. Its primary function is to assign a precise time step to each event detected. Time taggers are especially valuable when precise timing information is required for various applications, such as coincidence analysis.

An important characteristic of these detectors is their high-temperature dependence, which arises from the properties of superconductivity. Their optimal working temperature is around $\sim$ 0.83 K, achieved through a refrigeration system based on a mixture of ^{3}He and ^{4}He.

The dead time of these detectors is $t_d \sim 100$ ns. In comparison, semiconductor-based single-photon detectors like Single-Photon Avalanche Diode (SPAD) typically have a dead time higher than 1 μs (which is also due the fact that they must be intentionally kept off to reduce afterpulsing). Due to this dead time, the detectors can only record signals for reduced time intervals. If the counting rate is sufficiently high, meaning we expect more than one event on average during a dead time interval, the effective loss of signals cannot be overlooked. If we record N_{meas} events in 1 s, the total dead time

Figure 3.3: Photo of the SNSPDs used in this experiment (from datasheet).

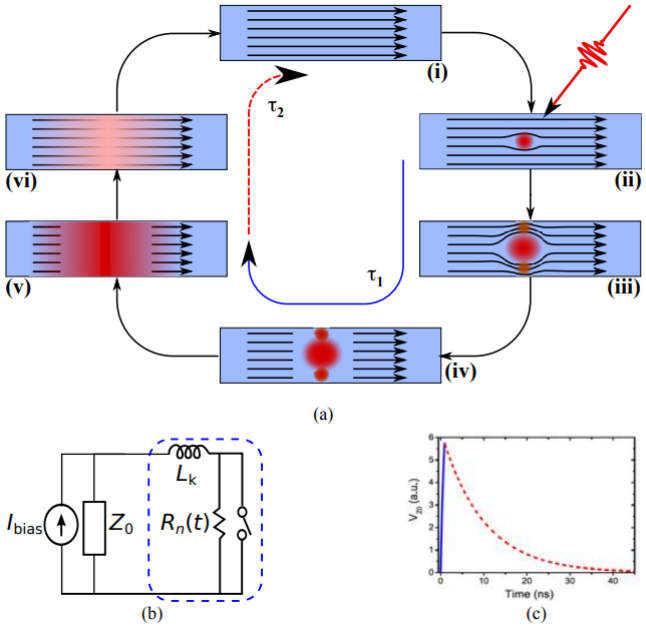

Figure 3.4: Schematic working principle of SNSPDs [55].

is given by $\Delta t_d = N_{meas} t_d$. To obtain the correct counting rate, taking into account the dead time of the detectors, we divide the recorded events by the time interval in which the detector is able to record signals, which is $1 - t_d N_{meas}$. This yields the effective counting rate N_{corr},which can be calculated as

$$N_{corr} = \frac{N_{meas}}{1 - t_d N_{meas}} \tag{3.2}$$

Another important characteristic of SNSPDs is the dependence of their quantum efficiency on the polarization of the incident radiation. This polarization dependence can be attributed to the anisotropic nature of the nanowire's crystal lattice. Superconducting nanowires are typically composed of crystalline materials, and their crystal structure exhibits distinct absorption cross-sections for photons with different polarizations. As a result, when the light is polarized in a direction different from the optimal alignment, the efficiency is significantly reduced, reaching only a fraction of the maximum value (leading to a reduction in efficiency of approximately $\sim 30 - 40\%$). To address this issue, polarization controller systems are employed. These systems allow to conveniently adjust the polarization of the signal photons after they have propagated through optical fibers. By using polarization controllers, it becomes possible to manipulate the polarization direction of the incident photons and optimize the efficiency of the SNSPDs for a wide range of experimental scenarios.

3.4 PPKTP Crystal

Periodically poled crystals are extensively used in SPDC sources due to their capability to enable quasi-phase-matching, leading to high-efficiency photon generation, as explained in Sec. 2.2.5. Various techniques are employed for the fabrication of periodically poled crystals.

One approach, proposed by Armstrong et al. [56], involves slicing the nonlinear crystal and alternating segments with opposite orientations. However, this method has limitations concerning the precise slicing of thick crystal pieces. An alternative technique involves melting the crystal and modulating the ferroelectric domains, as demonstrated by Yamada et al. [57]. This method allows for the inversion of single domains through the application of a static electric field.

For this specific experiment, we utilized a periodically poled potassium titanyl phosphate (PPKTP) crystal from Raicol, with dimensions of $1 \times 2 \times 20$ mm^3. To protect the crystal from dust and damage, we designed a small 3D-printed support holder enclosed within a protective box. The enclosure also serves to facilitate the placement of the crystal on other supports, such as the translation

stage. This feature enables fine adjustments and precise positioning of the crystal, thereby enhancing experimental control and accuracy in the setup.

3.4.1 Sellmeier Equations

In our study, we focus on a type-II SPDC process with the pump and idler photons polarized along the y-axis and the signal polarized along the z-axis. To fully characterize this process and understand the propagation of these beams within the crystal, we need to determine the corresponding refractive indexes, denoted as n_y and n_z. These refractive indexes are wavelength-dependent. To quantify these parameters, we employ the Sellmeier equations, which are empirical mathematical models commonly used to describe the refractive index of a material as a function of the wavelength of light passing through it. The Sellmeier equations are conventionally referenced at a specific temperature, usually $T = 25°C$. In this case, the refractive index along the z-axis, as a function of the wavelength λ (expressed in μm), is [58]:

$$n_z(\lambda[\mu\text{m}]) = \sqrt{A_z + \frac{B_z}{1 - C_z/\lambda^2} + \frac{D_z}{1 - E_z/\lambda^2} - F_z\lambda^2} \tag{3.3}$$

The corresponding Sellmeier coefficients are provided in Tab. 3.1.

A_z	B_z	$C_z[\mu\text{m}^2]$	D_z	$E_z[\mu\text{m}^2]$	$F_z[\mu\text{m}^{-2}]$
2.12725	1.18431	$5.14852 \cdot 10^{-2}$	0.6603	100.00507	$9.68956 \cdot 10^{-3}$

Table 3.1: Sellmeier coefficients for z-axis.

Similarly, to determine the refractive index along the y-axis, we rely on the relationship [59]:

$$n_y(\lambda[\mu\text{m}]) = \sqrt{A_y + \frac{B_y}{1 - C_y/\lambda^2} - D_y\lambda^2} \tag{3.4}$$

The associated Sellmeier coefficients are listed in Tab. 3.2.

A_y	B_y	$C_y[\mu\text{m}^{-2}]$	$D_y[\mu\text{m}^2]$
2.09930	0.922683	0.0467695	0.0138404

Table 3.2: Sellmeier coefficients for y-axis.

3.4.2 Temperature Dependence of Refractive Indexes

Changes in temperature can lead to modifications in the crystal's structure and optical properties, resulting in alterations of the refractive index. In many cases, the temperature dependence of refractive indexes is relatively small, particularly within a limited temperature range around room temperature. However, in certain processes like SPDC, even slight temperature variations can have a significant impact on the phase-matching or quasi-phase-matching conditions, as described by Eqs. 2.34 and 2.44. These variations deeply influence the generation of photons, affecting the efficiency and quality of the source.

In the case of KTP, the temperature dependence can be evaluated using the following expressions [60]:

$$\Delta n_z(\lambda[\mu\text{m}], T[^\circ\text{C}]) = n_{1,z}(\lambda)(T - 25^\circ\text{C}) + n_{2,z}(\lambda)(T - 25^\circ\text{C})^2 \tag{3.5}$$

$$\Delta n_y(\lambda[\mu\text{m}], T[^\circ\text{C}]) = n_{1,y}(\lambda)(T - 25^\circ\text{C}) + n_{2,y}(\lambda)(T - 25^\circ\text{C})^2, \tag{3.6}$$

where

$$n_{i,\alpha}(\lambda[\mu\text{m}]) = \left(a_0^{(i,\alpha)} + \frac{a_1^{(i,\alpha)}}{\lambda} + \frac{a_2^{(i,\alpha)}}{\lambda^2} + \frac{a_3^{(i,\alpha)}}{\lambda^3}\right) \tag{3.7}$$

The coefficients are presented in Tab. 3.3.

	$n_{1,z}[10^{-6}][°C^{-1}]$	$n_{2,z}[10^{-8}][°C^{-2}]$	$n_{1,y}[10^{-6}][°C^{-1}]$	$n_{2,y}[10^{-8}][°C^{-2}]$
$a_0[°C^{-1}]$	9.9587	-1.1882	6.2897	-0.14445
$a_1[\mu m/°C]$	9.9228	10.459	6.3061	2.2244
$a_2[\mu m^2/°C]$	-8.9603	-9.8136	-6.0629	-3.5770
$a_3[\mu m^3/°C]$	4.1010	3.1481	2.6486	1.3470

Table 3.3: Temperature dependence coefficients for refractive indexes n_y and n_z of KTP.

3.4.3 Temperature Dependence of Quasi-Phase-Matching

The manufacturer specifies a poling period $\Lambda = 46.2$ μm at a reference temperature of $T = 25°$C. To achieve quasi-phase matching, as described by Eq. (2.44), the optimal poling period depends on temperature and the wavelengths of the pump, signal, and idler beams. This dependence can be determined using the expressions for the refractive indexes provided in Eqs. (3.3) and (3.4) as follows

$$|\Lambda(T, \lambda_p, \lambda_s, \lambda_i)| = \frac{2\pi}{\frac{n_y(\lambda_p.T)}{\lambda_p} - \frac{n_z(\lambda_s,T)}{\lambda_s} - \frac{n_y(\lambda_i,T)}{\lambda_i}} \tag{3.8}$$

Here, we use the absolute value because the chosen Fourier expansion convention employed to rewrite the effective susceptibility in Sec. 2.2.5 results in a negative Λ. However, it is important to clarify that this negative sign does not impact the physical interpretation of this quantity.

With a poling period of 46.2 μm, the quasi-phase-matching condition is satisfied for degenerate SPDC with emitted photons at 1550 nm. Nevertheless, changes in temperature can affect this condition, altering the wavelengths of the emitted photons. In certain types of crystals, the temperature dependence of the refractive indexes significantly impacts the quasi-phase-matching condition and the efficiency of SPDC photon generation. In such situations, a common and effective solution is to use temperature controllers, such as Peltier cell thermostats, to maintain precise and stable temperatures during the experiment.

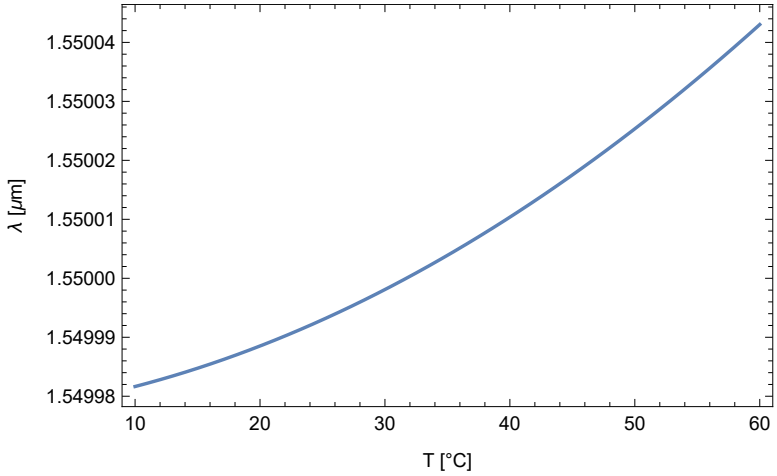

Figure 3.5: Wavelength of the emitted photons as a function of the crystal temperature for degenerate SPDC.

When designing the system, it is essential to assess whether such a solution is necessary or not. This evaluation involves analyzing the temperature dependence of the wavelength of the emitted photons. In particular, we can focus on the degenerate case where $\lambda_s = \lambda_i (= \lambda)$. The wavelength of the pump is fixed at $\lambda_p = 775$ nm, and the poling period is set to $\Lambda = 46.2$ μm. At a specific temperature T, the optimal wavelength λ for the emitted photons in degenerate SPDC is determined by solving the following equation:

$$\frac{n_y(\lambda_p, T)}{\lambda_p} - \frac{n_z(\lambda, T)}{\lambda} - \frac{n_y(\lambda, T)}{\lambda} + \frac{2\pi}{\Lambda} = 0 \tag{3.9}$$

The temperature dependence of the emitted photons wavelength, ranging from 10°C to 60°C, is depicted in Fig. 3.5. The plot clearly shows that the wavelength variation remains below 0.1 nm, which is considerably smaller than the bandwidth of many fiber filters that can be employed to precisely select these photons. Therefore, there is no need for a temperature control system for the crystal, as the small temperature-induced variations do not significantly impact the performance of the source.

3.5 Choice of the Optical Elements

Until now, we have thoroughly explored the specific properties of some experimental instruments, including the pump laser (Sec. 3.1), the optical fibers (Sec. 3.2), and the SNSPDs (Sec. 3.4). Understanding these properties was crucial as they directly influence the design of the source. Indeed, the intensity and polarization control of the laser source is accomplished through the implementation of a suitable optical system. Furthermore, to compensate for the polarization transformation induced by the optical fiber and to optimize the efficiency of the SNSPDs, a polarization control system becomes indispensable.

We can now proceed with the actual design of the source. In this section, we will elucidate the choices behind the optical setup, with a particular focus on the selection of lenses, while taking into account the constraints imposed by the geometry of the system.

3.5.1 Intensity and Polarization Controller

The pump beam for the SPDC source is generated by the 775 nm laser Mira. However, directly connecting the laser to the source is not feasible for several reasons. The SPDC source requires precise beam alignment, and the laser's direction can experience slight changes over time. Periodic realignment and cleaning processes can alter the settings of the optics inside the laser cavity, affecting the output beam direction. To ensure a stable pump beam direction aligned with the other optical elements of the source, it is necessary to decouple the laser from the source, allowing the pump beam to always maintain the same direction. This approach also enables easy replacement of the laser without the need for realigning the entire source. The solution to this challenge involves using an optical fiber. The light emitted by the laser is coupled into the optical fiber, which then guides the beam to the SPDC source. If the laser's alignment deviates, it can be easily adjusted by manipulating the mirrors that regulate the beam direction, redirecting it back into the optical fiber without disturbing the alignment of the source.

This type of configuration also provides the flexibility to control the intensity and polarization of the pump beam. The optical system used for this purpose is composed of:

- **Intensity controller**: The output beam of the laser has a power of approximately 2 W, and it usually operates at its maximum power for enhanced stability. However, both the PPKTP crystal and the optical fiber have a lower damage threshold. Therefore, we require an instrument that can efficiently reduce the input power by acting as an intensity controller. To achieve this, we use a combination of a QWP and a HWP placed before a PBS. The PBS selectively transmits horizontally polarized photons. By adjusting the angles of the waveplates, we can modify the polarization of the laser beam, specifically selecting its horizontal component and regulating the light transmitted by the PBS.

- **Polarization controller**: In various applications of the SPDC source, precise regulation of the pump beam's polarization is crucial. The light from the intensity controller is initially linearly polarized, with a horizontal polarization state denoted as $|H\rangle$, set by the PBS. However, as the light travels through the optical fiber, its polarization is altered. To compensate for this effect and set an arbitrary polarization state for the pump beam inside the source, we incorporate a combination of an HWP and a QWP after the intensity controller, just before the optical fiber. This polarization controller allows for finely adjusting the polarization of the pump beam according to our specific requirements.

After passing through the polarization controller, the light is coupled into the optical fiber using a lens with a focal length of 4 mm. The optical setup for the intensity and polarization controller is depicted in Fig. 3.6, while a photo of the experimental setup is shown in Fig. 3.7.

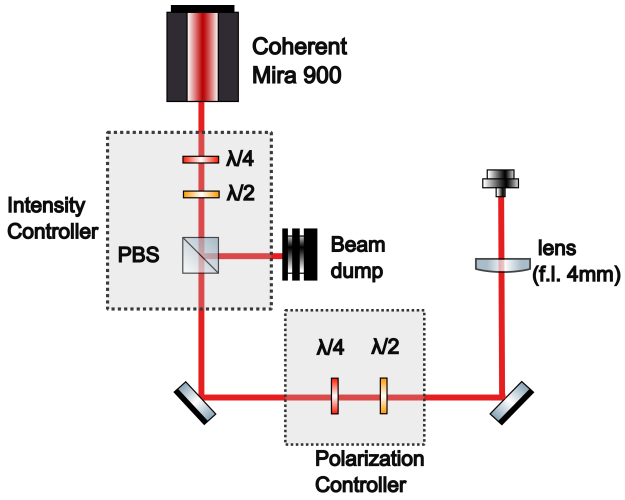

Figure 3.6: Schematic of the intensity and polarization controller [61].

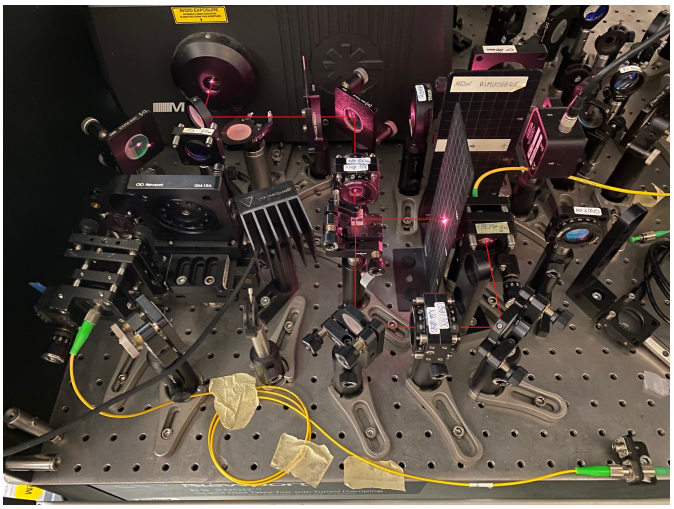

Figure 3.7: Photo of the intensity and polarization controller.

3.5.2 Estimation of the Optimal Focusing Conditions

An essential aspect of the source design is dedicated to selecting an appropriate set of lenses for pump, signal, and idler photons, aiming to optimize the source's performance in terms of brightness, heralding ratio, and spectral purity. In Sec. 2.4, we explored the collinear SPDC properties and identified certain critical focusing conditions that maximize all these parameters simultaneously. These conditions can be expressed in terms of the focal parameters ξ_j (as defined in Eq. (2.60)), where $j = p, s, i$, and they correspond to $\xi_p \approx \xi_s \approx \xi_i = 2.5$. We use these conditions as a starting point to determine the optimal set of lenses for the system.

Calculation of pump waist

We begin by calculating the pump momentum k_p of the beam in the PPKTP crystal. Next, we invert the relation that connects the waist of the pump beam w_p with ξ_p (as given in Eq. (2.60)), yielding the following results:

$$k_p = \frac{\omega_p}{c_{n_p}} = \frac{\omega_p n_p}{c} = \frac{2\pi n_p}{\lambda_p} \approx 1.43 \cdot 10^7 \text{ m}^{-1} \tag{3.10}$$

$$w_p = \sqrt{\frac{L}{k_p \xi_p}} = \sqrt{\frac{L\lambda_p}{2\pi n_p \xi_p}} \approx 23.7 \ \mu\text{m} \tag{3.11}$$

In these calculations, we used the following values:

$$\lambda_p = 775 \text{ nm} \tag{3.12}$$

$$n_p = n_y(\lambda_p) \approx 1.734 \tag{3.13}$$

$$L = 2 \text{ cm} \tag{3.14}$$

$$\xi_p = 2.5 \tag{3.15}$$

The refractive index n_p of the crystal along the y-axis at the wavelength λ_p has been calculated using the formula in Eq. (3.4).

Calculation of downconverted photons waists

In a similar manner to the pump photons, we can determine the optimal waists of the downconverted photons inside the crystal, denoted as w_s and w_i, by calculating their respective wavenumbers k_s and k_i. We then proceed to express the waists in terms of their corresponding focal parameters:

$$k_s = \frac{\omega_s}{c_{n_s}} = \frac{\omega_s n_s}{c} = \frac{2\pi n_s}{\lambda_s} \approx 7.36 \cdot 10^6 \text{ m}^{-1} \tag{3.16}$$

$$k_i = \frac{\omega_i}{c_{n_i}} = \frac{\omega_i n_i}{c} = \frac{2\pi n_i}{\lambda_i} \approx 7.03 \cdot 10^6 \text{ m}^{-1} \tag{3.17}$$

$$w_s = \sqrt{\frac{L}{k_s \xi_s}} = \sqrt{\frac{L\lambda_s}{2\pi n_s \xi_s}} \approx 32.9 \ \mu\text{m} \tag{3.18}$$

$$w_i = \sqrt{\frac{L}{k_s \xi_i}} = \sqrt{\frac{L\lambda_i}{2\pi n_i \xi_i}} \approx 33.7 \ \mu\text{m} \tag{3.19}$$

where we used:

$$\lambda_s = \lambda_i = 1550 \text{ nm} \tag{3.20}$$

$$n_s = n_z(\lambda_s) \approx 1.847 \tag{3.21}$$

$$n_i = n_y(\lambda_i) \approx 1.758 \tag{3.22}$$

$$L = 2 \text{ cm} \tag{3.23}$$

$$\xi_s = \xi_i = 2.5 \tag{3.24}$$

In this scenario, the refractive index of the signal photons is considered along the z-axis, while for the idler photons, it is along the y-axis. To compute these values, we employed Eqs. (3.3) and (3.4), respectively.

3.5.3 Geometrical Path Design for Fiber Coupling

To efficiently focus the pump beam inside the crystal and collect the downconverted photons, we need to design an appropriate optical setup. The pump laser is emitted from an optical fiber with a specific mode field diameter $MFD = 2W_0$, where W_0 represents the beam waist of the emitted Gaussian beam. Due to the divergence of the beam, a set of lenses is required to focus the beam within the crystal. Using a single lens setup can be challenging, as it necessitates precise positioning between the fiber and the crystal to ensure proper focusing. To overcome this challenge, a more practical approach involves employing a two-lens setup. The first lens serves to collimate the beam that emerges from the fiber[3]. Once collimated, a second lens can be positioned to efficiently focus the beam onto the crystal. This configuration offers the advantage of decoupling the focusing lens position from the fiber position. Since we are now using a collimated beam, the focusing lens can be conveniently positioned based on the crystal's location without being affected by the fiber's position. In Fig. 3.8, we provide a schematic representation of this two-lens setup. We refer to the beam radius of the collimated beam as W_0', while the focused beam waist is denoted as W_0''. The same setup can also be employed to collect the downconverted photons. In that case, the direction of the photons is opposite, but the approach remains equivalent.

Referring to Fig. 3.8, our goal is to establish a relationship between W_0'' and W_0, considering the focal lengths f_1 and f_2 of the two lenses. To begin, we look at the propagation of a Gaussian beam and its relation between W_0'' and W_0' [34]:

$$W_0' = W_0'' \sqrt{1 + \left(\frac{z_3 - z_2}{z_R''}\right)^2} = W_0'' \sqrt{1 + \left(\frac{f_2 \lambda_p}{\pi W_0''^2}\right)^2} \tag{3.25}$$

[3] A collimated Gaussian beam, namely a Gaussian beam with a zero divergence, is not theoretically possible. However, this is a useful approximation in the calculations that can be experimentally achieved by minimizing the divergence of the beam.

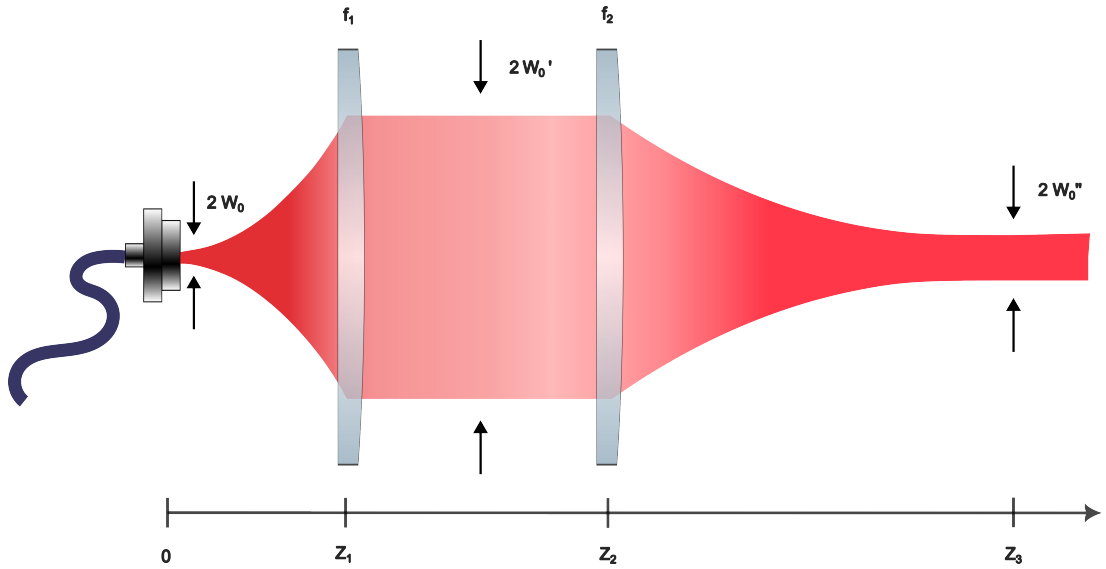

Figure 3.8: Schematic of the two-lens optical system employed for focusing and collecting the photons in the source. At the fiber output, the beam's waist is denoted as W_0. Once the beam is collimated, it possesses a beam radius of W_0'. Finally, the waist size inside the crystal is denoted as W_0''. The focal lengths of the lenses are denoted as f_1 and f_2, and they are positioned at distances z_1 and z_2, respectively, relative to the fiber output. The second lens is used to focus the beam at position z_3.

where we used the fact that the waist W_0'' is achieved at a distance $\Delta z'' = z_3 - z_2 = f_2$ from the second lens. Additionally, the Rayleigh range of the focusing beam is given by:

$$z_R'' = \frac{\pi W_0''^2}{\lambda_p} \tag{3.26}$$

We assume that the beam between the two lenses is collimated or, more generally, that $\Delta z' = z_2 - z_1 \ll z_R'$, ensuring that the beam radius W_0' remains approximately constant during its propagation between the two lenses. Similarly, we can relate W_0 to W_0' by describing the propagation of the Gaussian beam exiting from the fiber. The first lens is positioned at a distance $\Delta z = z_1 = f_1$ from the fiber output. Therefore, we obtain the expression for W_0' as follows:

$$W_0' = W_0\sqrt{1 + \left(\frac{z_1}{z_R}\right)^2} = W_0\sqrt{1 + \left(\frac{f_1\lambda_p}{\pi W_0^2}\right)^2}. \tag{3.27}$$

In this case, the Rayleigh range is $z_R = \frac{\pi W_0^2}{\lambda_p}$. We now have two equations that relate the collimated beam radius W_0' to f_1, f_2, W_0, and W_0''. By equating Eq. (3.25) and (3.27), we retrieve the following relations between f_1, f_2, and W_0'':

$$f_1 = \frac{W_0}{W_0''\lambda_p}\sqrt{(f_2\lambda_p)^2 - (\pi W_0'')^2(W_0^2 - W_0''^2)} \tag{3.28}$$

$$f_2 = \frac{W_0''}{W_0\lambda_p}\sqrt{(f_1\lambda_p)^2 + (\pi W_0)^2(W_0^2 - W_0''^2)} \tag{3.29}$$

$$W_0'' = \sqrt{\frac{\pi^2 W_0^4 + f_1^2\lambda_p^2 - \sqrt{\pi^4 W_0^8 + 2(f_1^2 - 2f_2^2)\pi^2 W_0^4\lambda_p^2 + f_1^4\lambda_p^4}}{2(\pi W_0)^2}} \tag{3.30}$$

Up until now, all the calculations have been based on the assumption of beams propagating in free space, where the refractive index is $n = 1$. However, in the actual experimental setup, the beam is focused inside the crystal, which has refractive indexes higher than one, depending on the polarization and wavelength of the light propagating inside it (as given by Eqs. (3.13), (3.21), and (3.22)).

Now, we need to establish a relationship between the free-space waist W_0'' and the optimal waist of the pump beam inside the crystal, denoted as w_p and calculated using Eq. (3.11).

The ABCD-matrix method is a widely used approach to describe the propagation of a Gaussian beam in different optical media [34]. It establishes a relationship between the input and output parameters of a paraxial optical system, particularly the complex radius of curvature of the beam, denoted as $q = z - z_0 + iz_R$. In the context of our setup, we are specifically considering the transformation of a Gaussian beam passing through a flat interface with different refractive indexes. When the beam transitions from a medium with refractive index n_1 to a medium with refractive index n_2, the transformation of the initial parameter q_1 is given by:

$$q_2 = \frac{Aq_1 + B}{Cq_1 + D} \quad \text{with} \quad T = \begin{pmatrix} A & B \\ C & D \end{pmatrix} = \begin{pmatrix} 1 & 0 \\ 0 & n_1/n_2 \end{pmatrix}. \tag{3.31}$$

Now, let's consider a Gaussian beam exiting from the crystal. The refractive index of the first medium for the pump beam is $n_1 = n_p$, while the refractive index of the second medium is $n_2 = 1$ (free-space). The q-parameter of the pump beam inside the crystal, denoted as $q_c = z_c - z_{0,c} + iz_{R,c}$, is related to the q-parameter of the beam outside the crystal, denoted as q, through the following equation:

$$q = \frac{q_c}{n_p} = \frac{1}{n_p}(z_c - z_{0,c} + iz_{R,c}) = \frac{1}{n_p}\left(z_c - z_{0,c} + i\frac{\pi w_p^2 n_p}{\lambda_p}\right) = \frac{z_c - z_{0,c}}{n_p} + i\frac{\pi w_p^2}{\lambda_p}. \tag{3.32}$$

Hence, the waist of the focused beam inside the crystal is equal to the value obtained in free-space, namely $W_0'' = w_p$. When the Gaussian beam exits from the crystal at a distance $z_c - z_{0,c}$ from its waist w_p, it is transformed into a Gaussian beam with the same beam radius at z_c, but at a distance $(z_c - z_{0,c})/n_p$ from its waist. Therefore, the only effect of the medium is a change of the focus position. The distance between the waist position of the Gaussian beam inside the crystal and the waist position in free-space can be calculated as follows:

$$\Delta d = (z_c - z_{0,c}) - \frac{z_c - z_{0,c}}{n_p} = (z_c - z_{0,c})\left(\frac{n_p - 1}{n_p}\right) \tag{3.33}$$

A schematic representation of the transformation of the focusing beam from free-space to the crystal is depicted in Fig. 3.9.

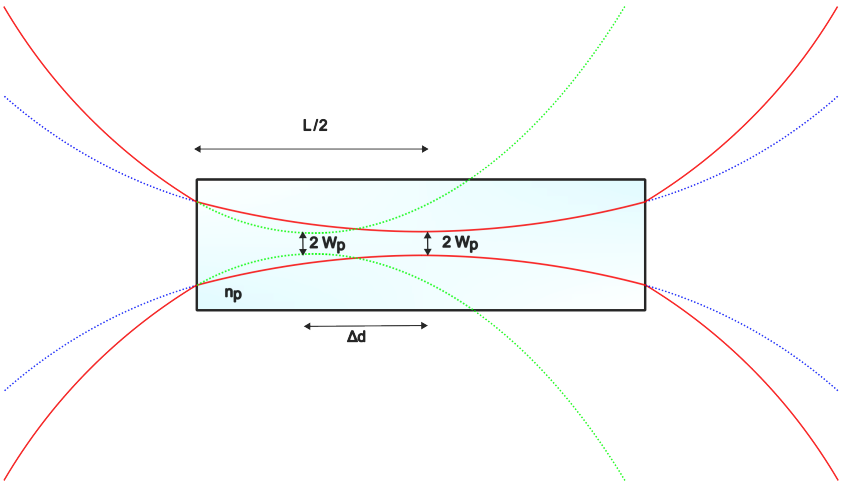

Figure 3.9: Transformation of a Gaussian beam passing from free-space into the crystal (red). The blue beam represents the continuation of the beam inside the crystal as if the refractive index did not change, while the green part shows the continuation of the free-space beam inside the crystal. The distance between the waist position of the free-space beam and that inside the crystal is denoted as Δd.

All the calculations performed on the SPDC process in Chap. 2 assume that the beam is focused at the center of the crystal. Therefore, we set the distance between the center of the crystal and the

crystal interface to half of the crystal length: $z_c - z_{0,c} = L/2$. As a consequence, the position of the free-space focus is shifted with respect to the crystal center by:

$$\Delta d = \frac{L}{2}\left(\frac{n_p - 1}{n_p}\right) \tag{3.34}$$

Due to the high refractive index of the crystal, this shift must be carefully considered during the realization and alignment procedure of the source.

When designing the optical setup of the source, we fix the waist W_0, which is half of the mode field diameter of the fiber. The goal is to find a set of two lenses with focal lengths f_1 and f_2 such that the waist inside the crystal (given by Eq. (3.30)) is as close as possible to the optimal values calculated in the previous section: w_p, w_s, and w_i for pump, signal, and idler, respectively.

3.5.4 Choice of the Lenses

The lenses used in this setup are plano-convex, which are suitable due to their ability to collimate and focus light effectively. However, the commercially available lenses (from Thorlabs) only offer some specific focal lengths, making it impossible to obtain the desired beam waist precisely (using Eq. (3.30)). Additionally, we must adhere to the geometrical constraints of the source, which is constructed on a breadboard measuring 450×600 mm^2.

In order to ensure consistency and symmetry between the signal and idler beams, we made the decision to employ an identical set of lenses for both beams. After carefully considering the constraints, we identified the optimal set of lenses with focal lengths for the pump, signal, and idler photons:

$$f_1^p = 25 \text{ mm}, \quad f_2^p = 250 \text{ mm}, \quad f_1^{s,i} = 40 \text{ mm}, \quad f_2^{s,i} = 250 \text{ mm} \tag{3.35}$$

The focal parameters are $\xi_p = 2.35$, $\xi_s = 2.53$, and $\xi_i = 2.66$.

To thoroughly assess the performance of the source and validate the SPDC model described in Chap. 2, we also opted to explore three other configurations that exhibit slight variations from the optimal case. For practical reasons, all the lens sets retain the same lenses for focusing the pump beam, while different lenses are utilized to collect the downconverted photons. This decision was motivated by the fact that altering the pump beam lenses is more complex, and for our purposes, modifying only the lenses responsible for the collection of the downconverted photons is sufficient. The specific lens sets chosen for the different configurations are provided in Tab. 3.4.

f_1^p[mm]	f_2^p[mm]	$f_1^{s,i}$[mm]	$f_2^{s,i}$[mm]	ξ_s	ξ_i	$w_{s,i}[\mu$m]	$r_s[\mu$m]	$r_i[\mu$m]
25	250	40	250	2.53	2.66	32.5	282.5	269.1
25	250	50	300	2.74	2.88	31.2	293.6	279.6
25	250	40	300	1.76	1.84	38.9	237.1	226.0
25	250	50	250	3.94	4.14	26.0	351.2	334.4

Table 3.4: Selection of the focussing and collimating lenses for pump, signal, and idler beams. The pump beam is fixed for all these configurations: $\xi_p = 2.35$, $w_p = 24.4\mu$m, $r_p = 179.2\mu$m.

An important parameter to take into account is the beam radius at the crystal interface, where the dimensions are 1×2 mm^2. The beam radius, denoted as r_j for each type of photon ($j = p, s, i$), can be calculated using the following formula:

$$r_j = w_j \sqrt{1 + \left(\frac{\lambda_j L}{2\pi n_j w_j^2}\right)^2} \tag{3.36}$$

To ensure the beam remains well-contained within the crystal and to prevent any clipping issues, it is essential to maintain a beam radius that is at least $1/3$ of the crystal thickness. This condition corresponds to a beam that is contained within the crystal by 6 standard deviations.

3.5.5 Spectral Filters

When dealing with entangled photons from an SPDC source, it is of utmost importance to reduce environmental noise to maximize the heralding ratio and the effective brightness of the source. One of the most significant contributions to the noise comes from the residue of the pump beam, which, in the collinear case, is collected similarly to signal and idler photons. Furthermore, given the high intensity of the pump beam, these photons can damage single-photon detectors (which can receive up to $\approx 10^7$ photons per second). Although a first level of selection is achieved using single-mode optical fibers optimized for transmitting photons at 1550 nm, it is not sufficient to completely eliminate the unwanted pump beam.

To achieve a precise selection of the downconverted photons and to distinguish them from noise, our source requires different types of spectral filters. We have selected two types of spectral filters in our setup, namely the FEL1000 Longpass Filter and the 12 nm bandpass filter FBH1550-12. These filters eliminate the residual pump photons and effectively reduce other sources of noise.

The spectral distribution of the downconverted photons is influenced by both the characteristics of the pump beam and the optical setup. When using a pulsed laser source, the emitted photon's bandwidth increases, leading to entangled photons with slightly different wavelengths. However, in specific applications such as multiphoton interaction experiments (e.g., Bell state measurement [46] and the Hong–Ou–Mandel effect [45]), narrow bandwidths are necessary. For these situations, we can employ optical fiber spectral filters with narrow bandwidths (approximately 0.5 nm). Using such filters can result in a reduction of brightness and heralding ratio due to the filtering out of some downconverted photons while the spectral purity is increased.

In summary, our source benefits from the use of spectral filters, allowing us to tailor the spectral characteristics of the downconverted photons to meet the specific requirements of our experiments. By selectively filtering and manipulating the spectral distribution, we optimize the performance of the entangled photon pairs for various applications.

3.6 Sagnac Interferometer

The SPDC process involves the emission of a pair of photons with different polarizations, represented by the separable state $|H_s\rangle |V_i\rangle$. However, the primary goal of the source is to generate entangled photons. This can be achieved through a well-designed optical setup that facilitates the interaction of the emitted photons in a way that leads to entanglement.

A widely used experimental setup for generating polarization-entangled photons in SPDC sources is based on a Sagnac interferometer, as demonstrated by Kim et al. in 2006 [62]. In this setup, the pump beam is directed through a dual-wavelength polarizing beam splitter (dPBS) that operates at two specific wavelengths (in our case 775 nm and 1550 nm). The dPBS divides the pump beam into two components based on polarization, the horizontal (H) and the vertical (V), which go into the opposite branches of the Sagnac loop (clockwise for V and counterclockwise for H, see Fig. 3.10). The general expression for the initial state of the pump field, denoted as $|\psi_p\rangle$, is:

$$|\psi_p\rangle = \alpha |H_p\rangle + \beta e^{i\phi_p} |V_p\rangle \tag{3.37}$$

In this expression, α and β are real coefficients, representing the complex probability amplitudes for horizontal and vertical polarizations, respectively, while ϕ_p accounts for the relative phase between the two polarization components. The goal is to manipulate the pump beam's polarization state within the Sagnac interferometer setup to achieve the desired entangled photon states.

The emission of downconverted photons is favored when the pump beam's polarization is horizontal. As a result, the reflected beam, with its vertical polarization, does not directly participate in this process. To address this issue, a dual-wavelength half-wave plate (dHWP) is introduced, with its fast axis rotated by 45° from the horizontal state. This transformation converts the polarization state $|V\rangle$ of the photon in this branch to $|H\rangle$, allowing it to be involved in the SPDC process.

The quantum output states after the interferometer generated in the clockwise (CW) and counter-clockwise (CCW) paths of the Sagnac loop are respectively:

$$|\psi_{CW}\rangle = \exp\{i[\phi_p + k_p L_B + \theta_p + (k_s + k_i)L_A + \delta]\}\eta_V \beta\, |H_s\rangle_1 |V_i\rangle_2 \tag{3.38}$$

$$|\psi_{CCW}\rangle = \exp\{i[k_p L_A + (k_s + k_i)L_B + \delta + \theta_s + \theta_i]\}\eta_H \alpha\, |V_s\rangle_1 |H_i\rangle_2 \tag{3.39}$$

Here, $\delta = (k_p + k_s + k_i)\frac{L}{2}$ represents the phase introduced by the crystal, which is the same in both paths (the crystal length here is denoted as L). The terms $\theta_{p,s,i}$ correspond to the phase introduced by the dHWP on the pump, signal, and idler photons, respectively. The parameters $L_{A,B}$ represent the length of the light path from the crystal interface to the dPBS in the two possible paths (clockwise or counterclockwise respectively). The fractions $\eta_{H,V}$ represent the efficiency of state selection in the two paths of the dPBS. These efficiencies are defined as the ratio between the number of photons projected into the corresponding state (H or V, depending on the path) and the total number of incident photons on the dPBS with that polarization. The distinction between the two branches arises because these two efficiency values are typically different; we usually achieve a better state selection on the transmitted path. In Eqs. (3.38) and (3.39), the two exiting ports of the dPBS are labeled as 1 and 2, respectively. A schematic of the experimental setup illustrating the transformation of both beams is shown in Fig. 3.10.

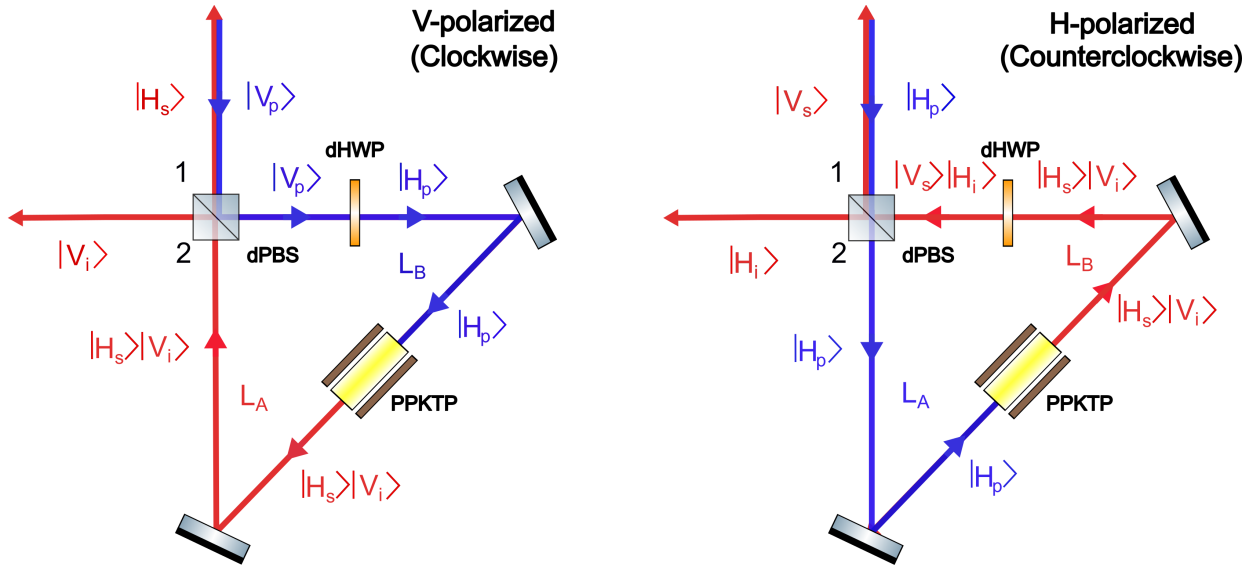

Figure 3.10: Schematic of the polarization Sagnac interferometer for the SPDC source. The clockwise (left) and counterclockwise (right) components are carefully directed to the PPKTP crystal, ensuring that their waist positions are precisely centered in the crystal. After passing through the crystal, the downconverted photons are then directed to the dPBS, where they are combined to create the entangled state $|\psi\rangle$.

The two separable states are recombined at the dPBS, and based on the free-space relation between the photon wavenumbers ($k_p = k_s + k_i$), we can simplify the final expression as follows:

$$|\psi\rangle \propto \left(|H_s\rangle_1 |V_i\rangle_2 + e^{i\phi}\gamma\, |V_s\rangle_1 |H_i\rangle_2\right) \tag{3.40}$$

where $\gamma = \frac{\eta_H \alpha}{\eta_V \beta}$ and $\phi = \theta_s + \theta_i - \theta_p - \phi_p + \epsilon$. In the relative phase ϕ, we have introduced the additional contribution ϵ. This term accounts for the phase difference that could arise in practical implementations due to a slight path mismatch between the two arms of the Sagnac loop, which occurs when the interferometer is not perfectly aligned.

To achieve the maximally entangled Bell state $|\Psi^+\rangle$, the relative amplitude γ can be set to one by adjusting the input components ratio of the pump beam $\frac{\alpha}{\beta}$ to compensate for the unequal transmittance and reflectance efficiencies. Moreover, a proper compensation of the phase difference is essential

for obtaining the Bell state. This requires precise alignment of the Sagnac loop ($\epsilon \sim 0$) and careful adjustment of the pump-phase ϕ_p. Liquid crystal retarders (discussed in Sec. 4.4.5) offer another possibility for phase compensation.

By properly compensating for the phase difference, the distinguishability between the clockwise and counterclockwise generated photons can be reduced, leading to increased quality of entanglement of the bipartite system. The Sagnac interferometer provides a stable and robust setup. The geometrical superposition of the two paths minimizes the impact of external disturbances, such as vibrations or environmental changes, resulting in a more reliable entanglement source.

Chapter 4

Development of the Source

The theoretical groundwork laid out in the preceding chapters provides the essential foundation for practically implementing the SPDC source. This chapter will provide a detailed and repeatable procedure for constructing sources of this kind. The process commences with the characterization of the crystal, employing suitable optical systems, and comparing the outcomes with simulation data. Additionally, we will elucidate the characterization process of other crucial optical components, such as the dPBS and the dHWP, both of which play a primary role in the performance of the source. Next, we will provide a step-by-step account of the assembly procedure for the source. This will involve the precise positioning of the crystal within the Sagnac loop, a critical factor that significantly influences the source's performance. Furthermore, we will elaborate on the alignment process for the complete Sagnac interferometer setup, an essential step to ensure the production of high-quality entangled photon states. Moreover, we will outline the alignment procedure for the optical setup utilized to collect the entangled photons, along with the process of switching optical configurations using different sets of lenses. Lastly, we will introduce the polarization measurement station utilized to evaluate the quality of the emitted entangled states. This measurement station provides the means for accurately characterizing and verifying the entanglement achieved in the SPDC source.

4.1 Characterization of the Crystal

We began by conducting an initial test that focused on characterizing the PPKTP crystal. This procedure aimed to assess the crystal's performance in terms of brightness, heralding ratio, and visibility. To achieve this, we employed two distinct optical setups: one dedicated to measuring brightness and heralding ratio, and the other to evaluate visibilities. Through these testing processes, we gained valuable insights into the crystal's capabilities and limitations, providing a deeper understanding of the practical alignment difficulties that may arise during the source development. The knowledge and experience gained from this characterization will be crucial in optimizing the performance of the source, ensuring its successful implementation.

4.1.1 Analysis of the Emitted Photon Pairs

The first quantity we aimed to observe was the emission of SPDC photons. To achieve this, we designed an optical setup capable of focusing the pump beam inside the crystal. For this particular test, we utilized a two-lens optical system, with lenses already available in the laboratory:

$$f_1^p = 40\text{ mm}, \quad f_2^p = 300\text{ mm}, \quad f_1^{s,i} = 40\text{ mm}, \quad f_2^{s,i} = 300\text{ mm} \tag{4.1}$$

The setup's main objective was to focus the pump beam, which comes from the intensity and polarization controller, onto the crystal and then efficiently collect the downconverted photons into two distinct channels. For a visual representation of the experimental arrangement, refer to Fig. 4.1 (a photo of the experimental setup is displayed in Fig. 4.2).

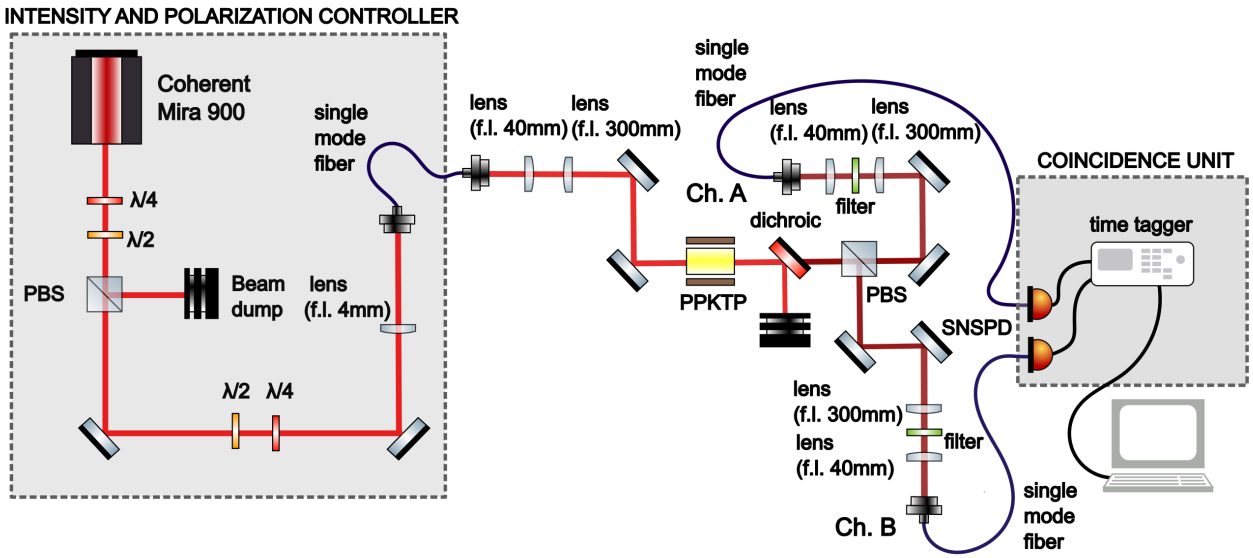

Figure 4.1: Schematic of the first experimental setup used to characterize the PPKTP crystal: measurement of brightness and heralding ratio.

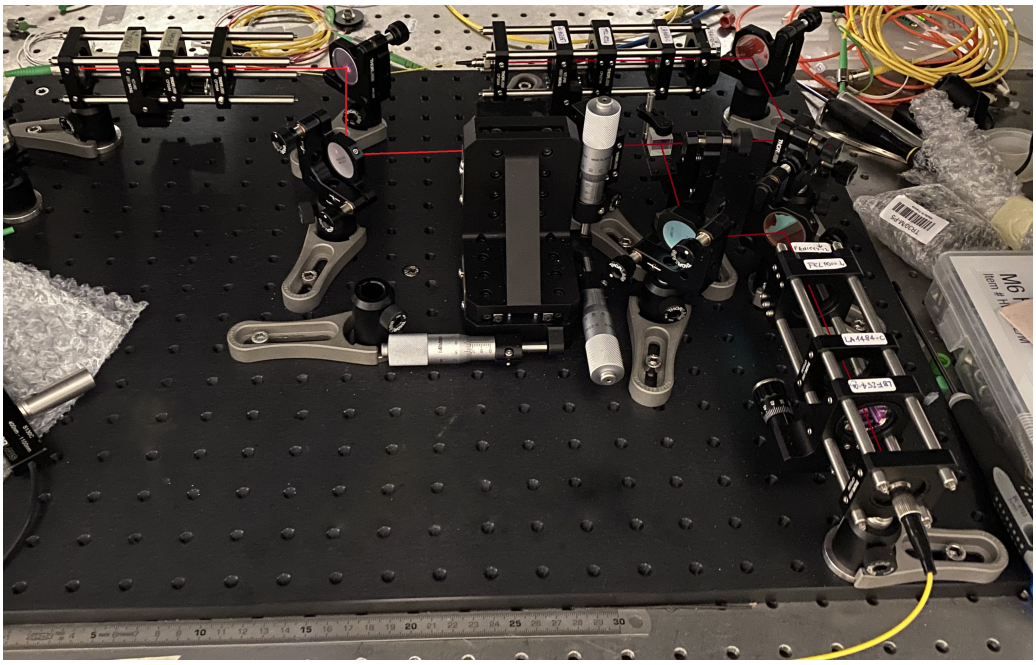

Figure 4.2: Photo of the first experimental setup used to characterize the PPKTP crystal: measurement of brightness and heralding ratio.

To filter out the majority of the pump photons, which do not interact in the crystal, we employed dichroic mirrors. These mirrors have variable reflection and transmission coefficients depending on the wavelength of the incident radiation. Consequently, they selectively reflect photons with specific wavelengths while allowing others to pass through. For our experiment, we utilized a dichroic mirror that transmits 1550nm photons (signal and idler) while reflecting the 775nm pump beam.

Our main interest lies in characterizing the emission of the signal and idler photons, particularly focusing on the brightness and heralding ratio. To achieve this, we require an apparatus that separates the signal photons from the idler photons. By employing two detectors and analyzing the coincidences between the two channels, we can identify the presence of an event since the two photons are emitted simultaneously by the SPDC process. To achieve the separation of the two beams, each possessing an orthogonal polarization state, we employed a PBS.

The crystal was carefully positioned within its support structure, establishing with its axes distinct horizontal and vertical directions. When properly aligned, these directions appriximately coincide with the polarization states selected by the PBS. As a result, the PBS acts as an efficient selector, directing the signal and idler photons along their respective paths based on their polarization.

The downconverted photons are then directed along two separate channels (denoted as A and B, see Fig. 4.1), where they are collected into optical fibers. These fibers guide the photons to the SNSPDs, passing through fiber polarization controllers which set the optimal polarization state that maximize the detectors efficiency.

The correct positioning of the crystal is a significant aspect that affects the performance of the SPDC process. To better adjust the crystal's position, we have placed it on a XYZ translation stage that enables precise movement along all three spatial directions. Additionally, we can regulate the inclination of the incident beam by using two mirrors. The alignment consists in two phases:

- **Waist positioning**: The first step consists in finding the correct positioning for the crystal along the beam direction such that the waist of the pump beam is centered in the crystal. To achieve this we employed the knife-edge method (which will be further elucidated in Sec. 4.4.2) to determine the beam profile. This method allowed us to identify the position of the waist of the beam. Subsequently, the crystal was positioned in a way that the focus in free-space was shifted from the center of the crystal by Δd (Eq. (3.33)).

- **Beam Direction**: Another important aspect is the direction of the pump beam. To set this, we adjusted the position of the crystal using the XYZ translation stage so that the beam was aligned with the border of one of the crystal's interfaces. If the beam was tilted, we observed two spots in the output: one transmitted through the crystal and the other reflected by the crystal's interface. By manipulating the tip-tilt of the mirrors, we were able to correct the inclination until only one spot was observed. Additionally, when we vertically moved the crystal, we ensured there were no discontinuities in the output beam as it transitioned from passing through the crystal to exiting it.

Once the crystal was properly positioned, we proceeded with aligning the system for photon collection. The initial alignment was accomplished using the *back-propagation* method. This involved injecting a 1550nm laser from the output fiber of each channel and aligning the system to ensure the pump beam and the 1550nm laser were precisely overlapped. During this phase, we temporarily removed the dichroic mirror and the spectral filters to visualize the pump beam until the fiber output of the 1550nm laser.

After completing the initial alignment, we connected the fiber outputs to the SNSPDs to start data collection. The events detected by the SNSPDs were then sent to a time tagger, which organized them based on their arrival time. Subsequently, a dedicated program analyzed the time tags and provided the counting rates for each channel, as well as the coincidences rates. The coincidences were determined by measuring the time difference between the recorded events of the two channels. If the time difference between two events fell within the temporal range defined by the coincidence window Δt_c, the events were recorded as coincidences (further details on this method will be presented in Sec. 5.1). To accurately estimate the coincidences between signal and idler events, we carefully set a delay between the two channels to account for any disparities in the lengths of their respective paths (including both the optical setup and the optical fibers). The distribution of signed temporal differences between two ordered channels typically follows a Gaussian distribution (as shown in Fig. 4.3). The standard deviation of this Gaussian ($\sigma \approx 80$ ps) is primarily influenced by the temporal resolution of the detectors and time tagger. In our experimental setup, the coincidence window was set to $\Delta t_c = 0.25$ ns, in order to accept approximately 6σ of the Gaussian distribution of signed differences. This window is a good compromise between capturing nearly all relevant events and minimizing the inclusion of accidental coincidences.

An interesting aspect of our analysis involves comparing the SPDC process in CW and pulse mode. To do this, we had to consider the possibility of accidental counts, i.e., coincidences that are not caused by paired SPDC photons (see Appendix D). In CW regime, the formula that estimates the accidental

coincidence rate is given by:

$$R_{acc}^{(CW)} = 2R_A R_B \Delta t_c \tag{4.2}$$

Here, R_A and R_B are the counting rates in the two channels, and Δt_c is the coincidence window. On the other hand, in pulse mode, the accidental coincidence rate can be estimated as:

$$R_{acc}^{(pulse)} = \frac{R_A R_B}{r_{MIRA}} \tag{4.3}$$

where $r_{MIRA} = 76\,\text{MHz}$ is the repetition rate of the laser. During the analysis, we took into account the accidental counting rates and removed them from the data. This allowed us to focus on the genuine correlations between signal and idler photons, and get more accurate results[1].

The results show that the heralding ratios in both channels are approximately $\eta_s \approx \eta_i \approx 16\%$ in both CW and pulse modes. To precisely estimate the brightness in this configuration, we varied the power of the pump beam and evaluated the number of effective coincidences. The data showed a linear trend (see Fig. 4.4), confirming that the brightness R_{si} depends linearly on the power of the pump beam P_{pump} at least at low power levels (while at higher power we expect a more important contribution of accidental coincidences caused by double-pair events, especially in pulse mode). This result is consistent with the fact that R_{si} is obtained by integrating $|\psi(\omega_s, \omega_i)|^2 \propto N_p$ in Eq. (2.48). The estimated brightness in CW and pulse mode are:

$$R_{si}^{(CW)} = (1630 \pm 10)\ \text{pairs/s/mW} \qquad R_{si}^{(pulse)} = (1580 \pm 20)\ \text{pairs/s/mW} \tag{4.4}$$

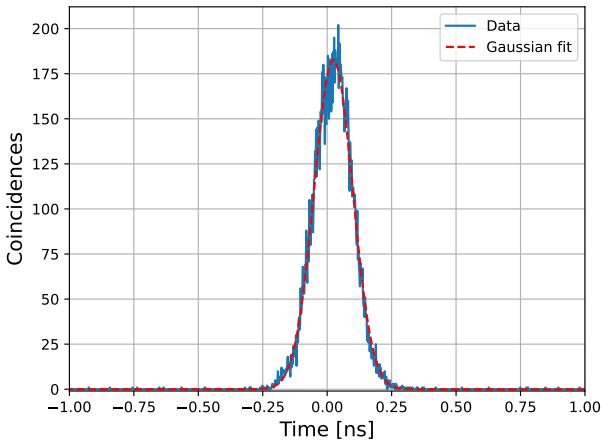

Figure 4.3: Histogram of time difference of coincidence events fitted with a Gaussian. The standard deviation is $\sigma \approx 80$ ps.

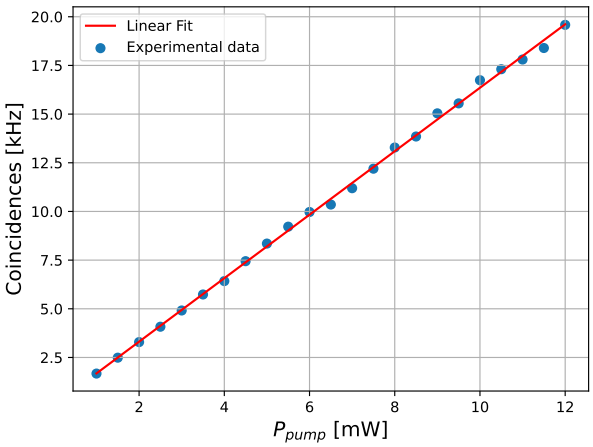

Figure 4.4: Linear regression of the measured coincidence counting rates plotted against the pump beam power.

These results are influenced by the losses of the experimental setup, which are due to the optics, optical fibers, and detectors. To quantify the actual performance of the source, we estimated the total transmission efficiency of each channel: ϵ_{TOT}^{A} (for channel A) and ϵ_{TOT}^{B} (for channel B).

For evaluating the transmission efficiency of the optics ϵ_{optics}, we employed a 1550nm laser beam injected through the output fiber, and then we measured the light dissipation from the fiber to the crystal. The crystal itself has a transmissivity $\epsilon_{CRY} = 0.937$ at 1550nm which is probably caused mostly by the two interfaces with the free space. As the emission can be approximated to occur at the center of the crystal, its effective contribution to the total transmission efficiency is $\sqrt{\eta_{CRY}}$. Similarly, we evaluated the transmissivity of the fibers that connect the source to the SNSPDs (ϵ_{fibers}). This was achieved by measuring the ratio between the transmitted and input optical power. To determine the

[1]Subtracting accidental coincidences is a common procedure typically used to characterize the properties of the source. However, in various applications, such as the Bell test, this method is not applicable.

detector efficiencies (ϵ_{SNSPD}), we conducted a specific procedure which is described in Appendix C). The overall efficiency of each channel is computed using the following expression[2]:

$$\epsilon_{TOT}^{A/B} = \sqrt{\epsilon_{CRY}}\epsilon_{optics}^{A/B}\epsilon_{fibers}^{A/B}\epsilon_{SNSPD}^{A/B} \tag{4.5}$$

The losses of the experimental setup (Tab. 4.1), will be utilized in Sec. 4.2 to simulate the SPDC process and compare the experimental results with the theoretical ones.

Channel	ϵ_{optics}	ϵ_{fibers}	ϵ_{SNSPD}	$\epsilon_{TOT}^{A/B}$
A	0.776	0.861	0.704	0.456
B	0.772	0.773	0.779	0.450

Table 4.1: Transmission efficiency of individual experimental elements.

4.1.2 Visibilities of the Emitted States

The quality of the entangled photons emitted by an SPDC source (as described in Sec. 1.5) is related to the visibilities in two mutually unbiased bases, such as the $\mathbb{Z}$ and $\mathbb{X}$ bases. The quantum states emitted in the SPDC process can be represented in the $\mathbb{Z}$-basis as the separable state $|H_s\rangle|V_i\rangle$. An important quantity to characterize the properties of the crystal is the measurement of the visibility in the $\mathbb{Z}$-basis. This measurement, indeed, allows quantifying the maximum achievable visibility of the states emitted by the source, thus serving as a reference point for enhancing the performance of the source during the alignment procedure which is used to generate the entangled photons (Sec. 4.4.6). For this purpose, we modified the experimental setup in Fig. 4.1 by replacing the PBS with a 50:50 BS. In addition, we incorporated an HWP and a PBS in each channel that can be used to perform projective measurements (as discussed in Sec. 1.3.1). The complete schematic of this experimental setup is depicted in Fig. 4.7, and a photo of the actual setup can be seen in Fig. 4.6.

This type of configuration is the foundation of a kind of SPDC source that emits polarization-entangled photon states by postselection. An important factor that must be considered in these types of sources is the *walk-off*. Although the $|H_s\rangle$ and $|V_i\rangle$ photons are generated instantaneously inside the crystal, they have two distinct polarizations and travel through a birefringent medium.

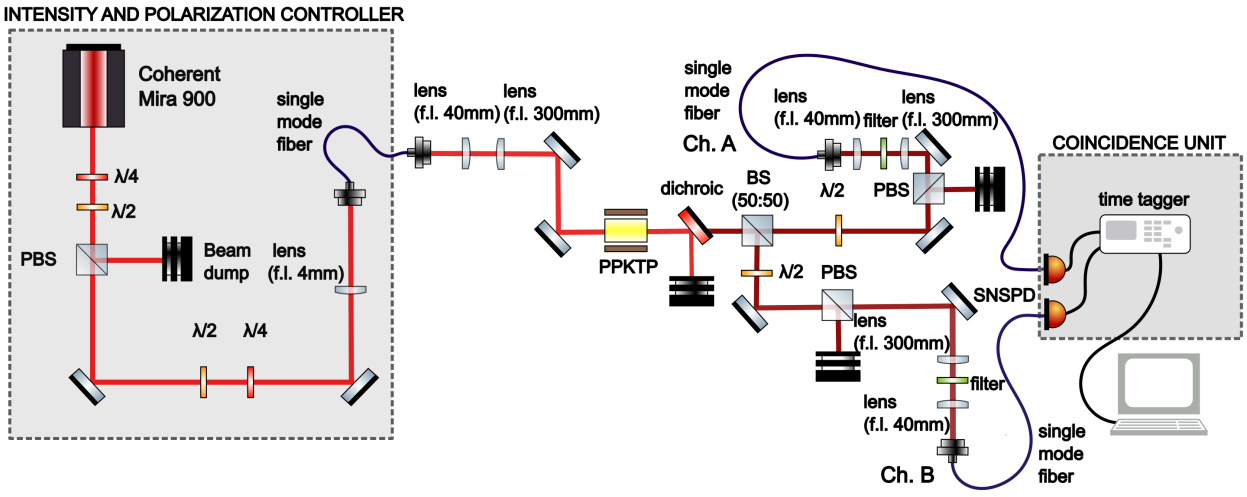

Figure 4.5: Schematic of the second experimental setup used to characterize the PPKTP crystal: measurement of the visibilities of the emitted states.

[2]In our analysis, we have not accounted for the coupling efficiency of the light collected into the single-mode optical fibers, as there is no precise way to estimate it. However, we can reasonably assume that, for a well-aligned optical setup, the coupling efficiency is $\eta_{coup} \geq 60\%$.

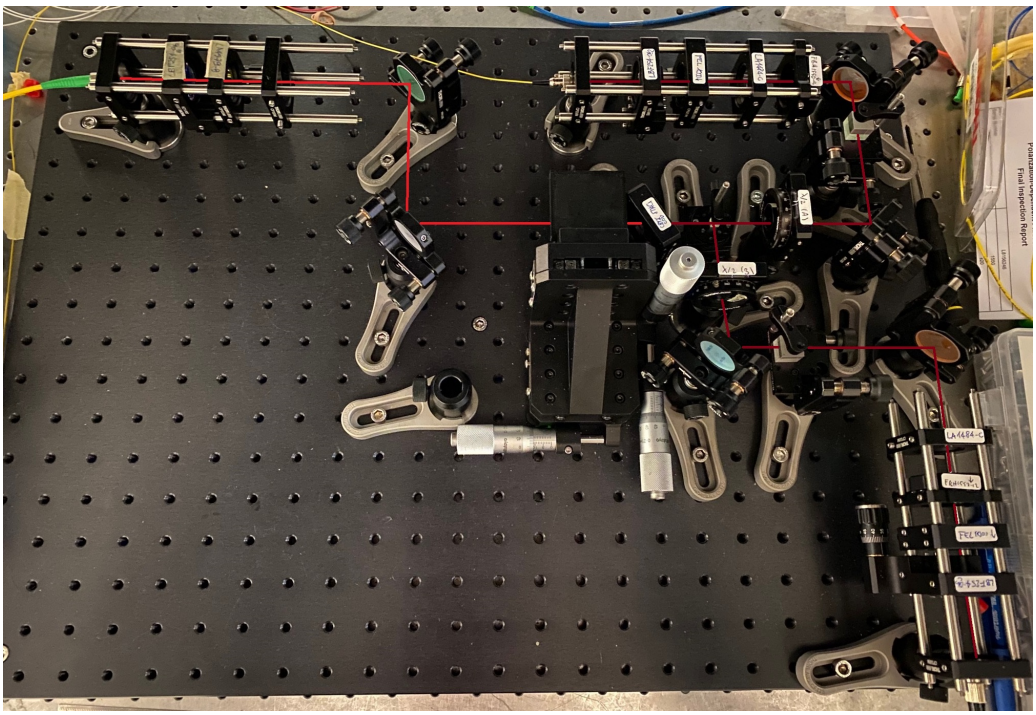

Figure 4.6: Photo of the second experimental setup used to characterize the PPKTP crystal: measurement of the visibilities of the emitted states.

The signal photons propagate with a velocity $v_s = c/n_s$, while the idler photons have a velocity $v_i = c/n_i$. As a result, the two photons are emitted by the crystal with a delay, referred to as temporal walk-off. To estimate the temporal walk-off, we can assume that the generation of the two photons occurs at the center of the crystal. It is given by:

$$\Delta t_{wo} = \frac{L}{2c}(n_s - n_i) \approx 3 \times 10^{-12} \text{ s} \tag{4.6}$$

This quantity affects the quality of the emitted entangled states in SPDC sources based on postselection. To address this issue, a potential solution is to compensate for the walk-off using another crystal, identical to the generation crystal but with half the length [63]. This compensating crystal can be placed in front of the generation crystal and rotated by 90° with respect to the first crystal. This arrangement ensures that the signal photons experience a refractive index n_i in the second crystal, while the idler photons experience n_s, effectively canceling out the walk-off. However, this method requires the second crystal to have the exact physical properties of the first crystal (preferably extracted from the same original crystal) and requires precise positioning.

If the walk-off is compensated, we can demonstrate that the optical setup illustrated in Fig. 4.5 can be used to produce entangled photons. The BS, indeed, acts on the input state $|H_s\rangle |V_i\rangle$, independently of its polarization, transmitting or reflecting the incident photons with the same probability. As a result, after the BS, the two-photon quantum state can be expressed as follows:

$$|\psi_{fin}\rangle \propto |H\rangle_A |V\rangle_A + e^{i\phi} |H\rangle_A |V\rangle_B + e^{i\phi} |V\rangle_A |H\rangle_B - |H\rangle_B |V\rangle_B \tag{4.7}$$

Where ϕ is a phase introduced by the BS in the reflected paths (for the purpose of this discussion, it is not necessary to know its exact value). In this representation, channel A corresponds to the transmitted path after the BS, while channel B corresponds to the reflected path. By considering only the events in which we have a coincidence between the two channel detections, we are effectively selecting only the states of the form:

$$|\psi_{PS}\rangle \propto |H\rangle_A |V\rangle_B + |V\rangle_A |H\rangle_B \propto |\Psi^+\rangle \tag{4.8}$$

In principle through this setup, one aims to obtain through postselection the state $|\Psi^+\rangle$, which can be

expressed in the $\mathbb{Z}$ and $\mathbb{X}$ bases as follows:

$$|\Psi^+\rangle = \frac{1}{\sqrt{2}}(|H\rangle|V\rangle + |V\rangle|H\rangle) = \frac{1}{\sqrt{2}}(|D\rangle|D\rangle - |A\rangle|A\rangle) \tag{4.9}$$

As a consequence, the visibilities in these two bases, written in terms of the coincidence counting rates N, become:

$$V_{\mathbb{Z}} = \frac{N_{HV} + N_{VH} - N_{HH} - N_{VV}}{N_{HV} + N_{VH} + N_{HH} + N_{VV}} \qquad V_{\mathbb{X}} = \frac{N_{DD} + N_{AA} - N_{AD} - N_{DA}}{N_{DD} + N_{AA} + N_{AD} + N_{DA}} \tag{4.10}$$

However, in the laboratory, we did not have a system capable of compensating for the significant temporal walk-off of the photons emitted by our crystal (Eq. (4.6)), but we still exploited the presented setup to measure the visibilities in $\mathbb{Z}$ and $\mathbb{X}$ bases. The presence of the walk-off, indeed, does not affect the measurement of the visibility in the $\mathbb{Z}$-basis, which still remains the main objective of this characterization, but only the visibility in the $\mathbb{X}$-basis.

The experimental measurement of the visibilities in these two bases requires the estimation of the coincidence counting rates through different polarization measurements. To determine the polarization state of the system, we need to find the angles of the HWPs (in the reference system of the rotary mounts in which they are inserted) corresponding to the states $|H\rangle$ or $|V\rangle$. This can be achieved by rotating the HWPs until we identify a minimum, which can be in the form of $|H\rangle_A|V\rangle_B$ or $|V\rangle_A|H\rangle_B$. In this case, we assumed the first scenario and set $\theta_A^{(H)} = 339.5°$ and $\theta_B^{(V)} = 354°$. If we use the opposite convention, we obtain the same results, as we just invert the values of the two minima or maxima, respectively. The results are summarized in Tab. 4.2. Furthermore, Fig. 4.7 illustrates the scan of the coincidence counting rate as a function of the angle of the B-analyzer, while maintaining the angle of the A-analyzer fixed at $\theta_A^{(H)} = 339.5°$.

$\mathbb{Z}$-basis	θ_A	θ_B	Coincidences [1min]	$\mathbb{X}$-basis	θ_A	θ_B	Coincidences [1min]
N_{HH}	339.5°	309°	350 ± 19	N_{DD}	2°	331.5°	38330 ± 200
N_{HV}	339.5°	354°	184990 ± 430	N_{DA}	2°	16.5°	37900 ± 190
N_{VH}	294.5°	309°	191590 ± 440	N_{AD}	47°	331.5°	37400 ± 190
N_{VV}	294.5°	354°	275 ± 17	N_{AA}	47°	16.5°	39430 ± 200

Table 4.2: Number of coincidences recorded in 1-minute acquisition time. We assume Poisson error on the photon counts.

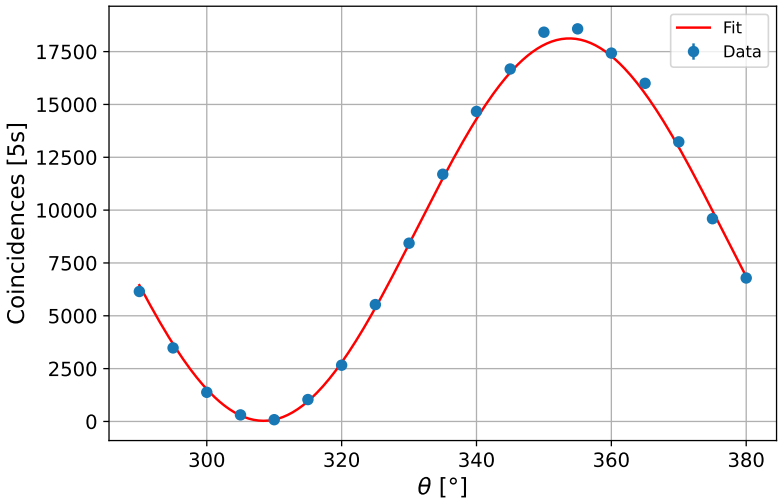

Figure 4.7: Scan of the $\mathbb{Z}$-basis visibility of the first setup. The angle of the A-analyzer is fixed to $\theta_A^{(H)} = 339.5°$ (state $|H\rangle$) while the angle of the B-analyzer θ is varied in the range $[290°, 380°]$. Data are fitted with a function of the type $A \cdot \sin^2(\theta + \theta_{\text{offset}}) + B$, using A,B, and θ_{offset} as free parameters.

The visibilities in the $\mathbb{Z}$ and $\mathbb{X}$ bases, estimated by the experimental coincidence counts in Tab. 4.2, are respectively:

$$V_{\mathbb{Z}} = (99.67 \pm 0.01)\% \qquad V_{\mathbb{X}} = (1.6 \pm 0.3)\% \tag{4.11}$$

This test has shown that it is possible to achieve high visibilities in the $\mathbb{Z}$-basis, and therefore, in principle, these values could be attained in both the $\mathbb{Z}$ and $\mathbb{X}$ bases[3] in the final source. Factors that might influence the reduction of such visibility in the final source setup are related to the optical components such as PBSs and waveplates used to perform measurements, the dPBS in the Sagnac loop, and the fibers employed to transfer the states (a more detailed description of these effects is found in Sec. 1.6.2).

Another result of this test (as expected) is the low visibility in the $\mathbb{X}$-basis. In particular, we verified the impact of the walk-off on the quality of the entangled states emitted by SPDC sources based on postselection. Only with a good walk-off compensation it is possible to generate entangled photons. Moreover, another problem of these sources is that the brightness is reduced to 50% of the maximum value because half of the emitted photons are discarded by the BS (Eqs. (4.7) and (4.8)) The optical setup based on the Sagnac loop, which is the working principle of the source discussed in this thesis, allows for achieving high performance in terms of brightness, heralding ratio, and visibilities. Although it is more complicated to build and align, it is possible to demonstrate that this setup provides an efficient method to solve the walk-off issue without sacrificing brightness and heralding ratio.

4.2 Simulations

In this section, we present the simulations of the SPDC process, which are used to evaluate the brightness and heralding ratio based on the model described in Chap. 2. Here, in particular, we will specifically show the results obtained for the optical configuration used to characterize the crystal and we will compare the experimental results of brightness and heralding ratio with the theoretical ones. The central aspect involves estimating the biphoton wave function (Eq. (2.48)) using specific input parameters:

- Effective susceptibility: In this process, the pump and idler photons are polarized along the y-axis, while the signal is polarized along the z-axis. Consequently, the effective susceptibility is obtained as $\chi^{(2)}_{eff} = \chi^{(2)}_{232}$. This quantity is typically related to the tensor d_{ijk}, as defined in the literature [64], by the equation:

$$d_{ijk} = \frac{1}{2}\chi^{(2)}_{ijk} \tag{4.12}$$

  Furthermore, depending on the symmetry of the system, this tensor is usually rewritten in terms of the contracted matrix d_{il} of size 3×6. The index l depends on the polarization of the signal and idler photons, as shown below:

jk :	11	22	33	23, 32	31, 13	12, 21
l :	1	2	3	4	5	6

(4.13)

  For this specific case, given the polarization of the pump, signal, and idler photons, we find that $\chi^{(2)}_{eff} = 2d_{2,4} = 7.28 \cdot 10^{-12}\text{m/V}$.

- The transmission efficiency of the apparatus for each channel, ϵ^{A}_{TOT} and ϵ^{B}_{TOT}, are considered when estimating the heralding ratios for signal and idler photons. On the other hand, the brightness is determined by considering the total transmission efficiency of both channels: $\epsilon_{TOT} = \epsilon^{A}_{TOT}\epsilon^{B}_{TOT}$ (the losses are presented in Tab. 4.1).

- The waists of the pump, signal, and idler photons are $w_p = 18.6\ \mu$m and $w_s = w_i = 39.0\ \mu$m.

[3] In practice, the visibility in the $\mathbb{X}$-basis, as will be discussed in Sec. 5.3, is typically lower than that in the $\mathbb{Z}$-basis due to imperfections of the experimental setup that result in a reduction of entanglement.

- The refractive indexes $n_p(\lambda_p, T)$, $n_s(\lambda_s, T)$, and $n_i(\lambda_i, T)$ (defined in Eqs. (3.3), (3.4), and (3.5)) are calculated as functions of the wavelength of the radiation, while the temperature is fixed at 20°C.
- The length of the crystal is L = 2 cm.
- The poling period is $\Lambda = 46.2$ μm.

4.2.1 Joint Spectral Density

We are interested in evaluating the joint spectral density $|\psi(\omega_s, \omega_i)|^2$, which represents the shape of the biphoton spectral distribution. Specifically, we explore how this distribution changes with varying pulse duration τ_p. Four simulations were conducted, setting τ_p to 1 ns, 10 ps, 1 ps, and 100 fs. Among these cases, the first one effectively represents the CW scenario, because 1 ns is long enough to cause negligible spectral effects, while the other three configurations represent the three possible configurations of Mira. The joint spectral distributions, rescaled to their maximum value, are depicted in Figs. 4.8, 4.9, 4.10, and 4.11.

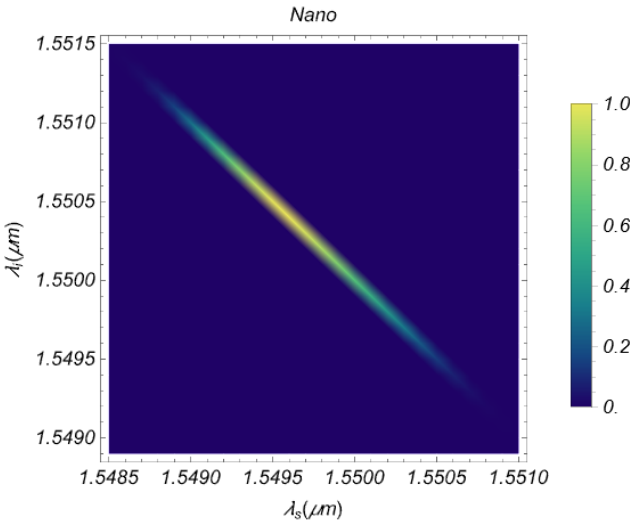

Figure 4.8: Rescaled spectral density distribution of downconverted photons with $\tau_p = 1$ ns.

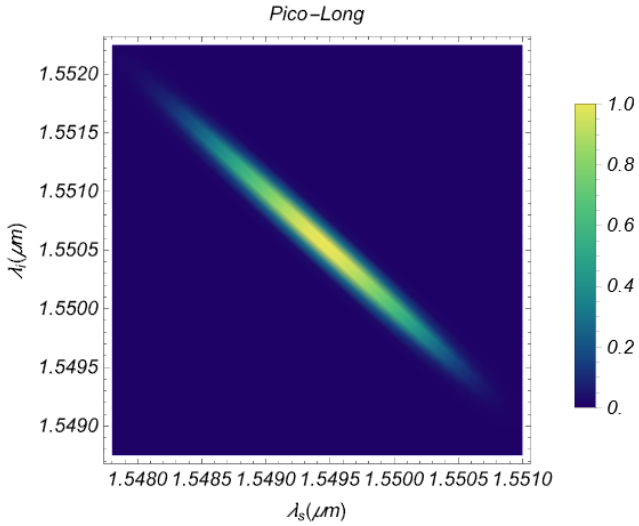

Figure 4.9: Rescaled spectral density distribution of downconverted photons with $\tau_p = 10$ ps.

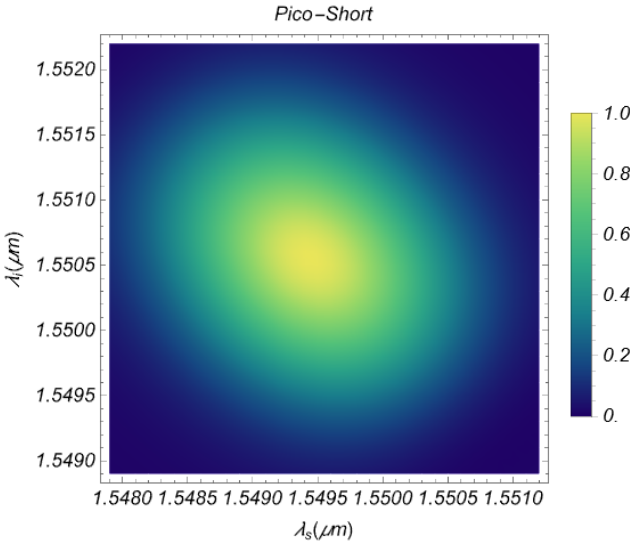

Figure 4.10: Rescaled spectral density distribution of downconverted photons with $\tau_p = 1$ ps.

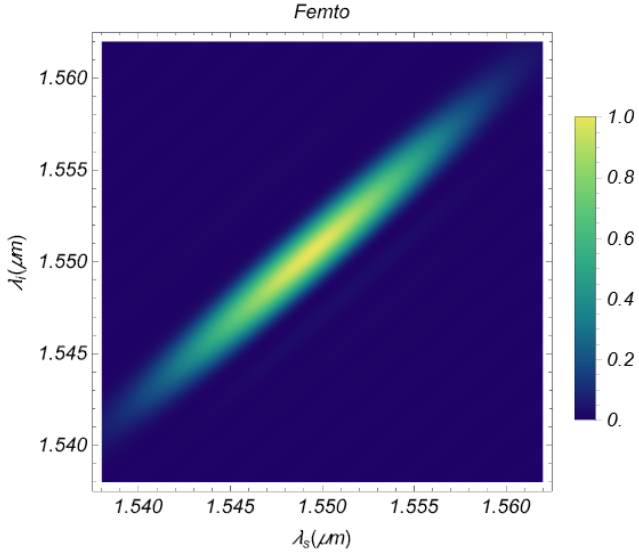

Figure 4.11: Rescaled spectral density distribution of downconverted photons with $\tau_p = 100$ fs.

In the case of long pulses (Figs. 4.8 and 4.9), the joint spectral density exhibits a tight clustering around the values that satisfy the condition $\omega_s + \omega_i = \omega_p$. As the pulse duration becomes shorter (Figs. 4.10 and 4.11), the energy of the pump photons gets distributed over a wider range of frequencies. Consequently, this broadens the energy conservation condition, leading to a widened spectral distribution. Fig. 4.10 illustrates that when $\tau_p \approx 1$ ps, the spectral distribution becomes approximately symmetric, and the bandwidth of the downconverted photons is around 4 nm. For even shorter pulse durations (Fig. 4.11), the effect of broadening the spectral distribution leads to a significant increase of the photon bandwidth, which, in the case of $\tau_p \approx 100$ fs, is approximately 20 nm.

These simulations offer valuable insights into the properties of the SPDC process for different pulse durations. Particularly, in applications in which short pulses are needed, these results become significant. Short pulses can aid in better selecting events from the noise, especially in scenarios where channel losses are high. However, they also result in a significant increase in the bandwidth, which reduces spectral purity. Additionally, when employing very short pulses, the use of narrow spectral filters can lead to a drastic reduction in brightness and heralding ratio. An optimal trade-off is achieved when the pulse duration is around $\tau_p \approx 1$ ps, which is similar to the pulse duration of Mira in the working configuration ($\tau_p = 2.17$ ps). For the simulations, we will use this specific value to evaluate the performance of the SPDC source in pulse mode.

4.2.2 Simulation Results

We conducted simulations of the SPDC process in both CW and pulse modes to evaluate the expected brightness and the heralding ratios for signal and idler photons in the specific optical configuration used to characterize the PPKTP crystal (Sec. 4.1.) For this purpose, we integrated the joint spectral density over a suitable range of frequencies for the signal and idler photons, corresponding to a wavelength range of 12 nm centered at 1550 nm which approximately corresponds to the passband of the filters employed in the experiment and we estimated the theoretical brightness $R_{si}^{(sim)}$. Similarly, following the approach described in Sec. 2.3.2 we evaluated the theoretical rate of photons (signal or idler) emitted in the collecting Gaussian mode regardless of the spatial mode of the corresponding partner. They are denoted (following the notation of Sec. 2.3.2) as $R_s^{(sim)}$ (for signal) and $R_i^{(sim)}$ (for idler). From these quantities, we estimated the theoretical heralding ratios for signal ($\eta_s^{(sim)} = R_{si}^{(sim)}/R_s^{(sim)}$) and idler ($\eta_i^{(sim)} = R_{si}^{(sim)}/R_i^{(sim)}$) photons. These theoretical results were evaluated neglecting the losses of the apparatus (listed in Tab. 4.1). To obtain estimates of these quantities that are comparable with experimental data, we took into account the contribution of the transmission efficiencies of each channel (ϵ_{TOT}^A and ϵ_{TOT}^B), evaluating the effective performance of the source (which would be achieved without experimental losses) in the following way:

- **Brightness**: The effective brightness is calculated considering the contribution of the losses of both channels: $R_{si} = R_{si}^{(exp)}/(\epsilon_{TOT}^A \epsilon_{TOT}^B)$.
- **Heralding Ratio**: The single-photon collection rates for the signal and idler photons are estimated considering the losses of the corresponding channel in which they were measured. In the experimental setup described in Sec. 4.1 the signal photons were detected in channel A while the idler photons in channel B. For this reason, the effective single-photon collection rates can be calculated as $R_s = R_s^{(exp)}/\epsilon_{TOT}^A$ and $R_i = R_i^{(exp)}/\epsilon_{TOT}^B$. Therefore, the effective heralding ratios become $\eta_s = R_{si}/R_s = \eta_s^{(exp)}/\epsilon_{TOT}^B$ and $\eta_i = R_{si}/R_i = \eta_i^{(exp)}/\epsilon_{TOT}^A$.

The differences between the simulations in CW and pulse modes are negligible and this fact is also confirmed by the experimental results. For this reason, we compared the experimental results and simulations only in the CW mode. These results are listed in Tab. 4.3.

Even if the simulations can approximately predict the experimental quantities, it is important to note that there might be some multiplicative factors not considered by the model, which could explain the higher values of the simulated brightness and heralding ratios. These factors may arise, for instance, by an incorrect estimation of some quantities such as the effective susceptibility or the refractive indexes of the medium. Moreover, in these calculations, we used the theoretical waists of

the pump, signal, and idler photons estimated through the theoretical formulas described in Sec. 3.5.3 that are applied to the set of lenses selected for this experimental configuration (Eq. 4.1. These waists may differ from the experimental values. This is primarily due to the experimental error in the lens positioning relative to the theoretical positions. Moreover, the lenses could induce non-ideal effects such as aberrations that are not considered by the theoretical model.

The multiplicative factors of the brightness and single-photon rates are eliminated in the heralding ratios, which are in any case overestimated compared to the experimental results. However, in these simulations, we did not consider the efficiency of the fiber coupling, which could explain the observed reduction of 60% in the experimental single-channel counting rates, as this efficiency is not directly measurable. Lastly, it is crucial to recognize that the performance of the SPDC process strongly depends on the alignment procedure. Some of the model assumptions, such as the centering of the crystal, may not be fully respected thus affecting the effective performance of this process. To further validate the presented model, it is essential to explore the SPDC process in other optical configurations. This will be studied in Chap. 5, where we will delve into the exploration and discussion of additional experimental scenarios to provide a more comprehensive understanding of the validity and limits of this model in describing the SPDC process.

	R_{si} [pairs/s/mW]	η_s	η_i
Effective exp. values	8000	0.36	0.36
Simulation	13040	0.63	0.64

Table 4.3: Comparison of the effective experimental brightness and heralding ratios with the simulations of the first setup employed for the characterization of the PPKTP crystal in CW. The effective experimental values are estimated by considering the contribution of the experimental losses.

4.3 Optics Characterization

There are crucial optical elements within the source that significantly impact its performance. One of these components is the dual-wavelength PBS (dPBS). Its primary function (as described in Sec. 3.6) involves selecting the downconverted photons emitted by the crystal and then directing them along distinct paths, depending on their polarization state. Another important component is the dual-wavelength HWP (dHWP) which is positioned within the Sagnac loop. Its crucial role involves converting the reflected V-polarized beam into an H-polarized beam, thereby enabling its interaction with the crystal. In this section, we will present the characterization of these two components which, as discussed in Sec. 4.4, will play a significant role in the implementation of the source.

Dual-wavelength PBS

For this particular source, the PBS0012-775/1550 from Newlight Photonics was utilized. The performance of this optical component is evaluated in terms of two quantities: the extinction ratio and the transmittance. The first quantity evaluates the dPBS's efficiency in selecting horizontal polarization for the transmitted path and vertical polarization for the reflected path, while the second parameter enables us to assess the losses induced by this optical component. The performance of the dPBS was assessed for each branch (transmitted and reflected) at both working wavelengths using laser beams at 775nm and 1550nm. To control and set an arbitrary linear polarization incident on the dPBS, we employed a combination of a PBS to linearly polarize the light and an HWP to rotate the polarization state. The significant experimental parameters for this characterization are the powers of transmitted light (P_H) and reflected light (P_V), which are proportional to the number of photons selected by the dPBS in the H and V states, respectively. The assessment of the dPBS's performance is carried out as follows:

- Extinction ratio: This quantity can be measured experimentally by calculating the ratio between the minimum ($P^{min}_{H/V}$) and maximum ($P^{max}_{H/V}$) powers observed in each branch of the dPBS, obtained by adjusting the incident light's polarization using the HWP. The minimum power is

indeed measured when the incident light's polarization is orthogonal to the one selected in that branch by the dPBS. In the ideal case, where state selection is perfect, this quantity is zero. However, in real components, there exists a small fraction of states that are not accurately selected by the dPBS. The extinction ratio of each branch is therefore expressed as:

$$R_{H/V} = \frac{P^{min}_{H/V} - P_{bkg}}{P^{max}_{H/V} - P_{bkg}}$$

where in this formula we have subtracted the contribution of the background power level P_{bkg}.

- Transmittance: To assess the transmission efficiency of each branch, we configured the polarization of the incident light to maximize the power in each branch. Subsequently, we measured the ratio between the maximum light output from the branch ($P^{max}_{H/V}$) and the incident light on the dPBS (P_0). Specifically, the expression for the transmittance of each branch, after subtracting the background contribution, is:

$$T_{H/V} = \frac{P^{max}_{H/V} - P_{bkg}}{P_0 - P_{bkg}}$$

The results of this characterization, evaluated for each branch of the dPBS and at both wavelengths, are summarized in Tab. 4.4.

Wavelength [nm]	R_H	R_V	T_H	T_V
775	$3.46 \cdot 10^{-4}$	$1.77 \cdot 10^{-3}$	0.978	0.969
1550	$1.29 \cdot 10^{-4}$	$4.74 \cdot 10^{-3}$	0.981	0.971

Table 4.4: Characterization of the dPBS: extinction ratio and transmittance.

An interesting property of this dPBS is that the optimal extinction ratio in the reflected beam at 1550 nm is achieved when it is tilted by approximately $\approx 4°$, deviating from the ideal configuration of being perpendicular to the input beam. When untilted, the extinction ratio is around 1.9%, but this dramatically improves to 0.47% when tilted. Similarly, for the 775nm reflected beam, the maximum extinction ratio is attained at a tilting angle of approximately $\approx 1.5°$. Notably, the extinction ratio in the transmitted path is not significantly affected by the tilting angle in both cases. Given that visibility is one of the most critical parameters of the source and is contingent on the dPBS's proficiency in separating downconverted photons according to their polarization, this characterization assumes paramount importance in actualizing the source setup.

Dual-wavelength HWP

Another crucial optical element is the dHWP. For this source, we utilized the WPD03-H1550-H775 from Newlight Photonics. Similar to the dPBS, characterizing the properties of the dHWP involves evaluating the extinction ratio and transmittance for both wavelengths. To achieve this, we employed a PBS to polarize the light incident on the dHWP and a second PBS after the dHWP to filter only the transmitted component of the light. By varying the angle of the dHWP, we can effectively manipulate the H-component of the beam, thereby altering the intensity of the beam transmitted by the second PBS. Plotting the power as a function of the dHWP angle, we obtained the plots displayed in Figs. 4.12 and 4.13. The data obtained align well with Malus' law and are fitted using a function of the form $P_{\max} \cdot \sin^2(\theta + \theta_{\text{offset}}) + P_{\min}$ to extract the maximum and minimum transmitted powers. Similarly to the dPBS, the effectiveness of the dHWP relies on the extinction ratio defined as $R = \frac{P_{\min} - P_{\text{bkg}}}{P_{\max} - P_{\text{bkg}}}$ and the transmittance denoted as $T = \frac{P_{\max} - P_{\text{bkg}}}{P_0 - P_{\text{bkg}}}$, where P_0 represents the power measured before the HWP, and P_{bkg} denotes the background power. A higher extinction ratio is indicative of a greater capacity to rotate the polarization state effectively. The comprehensive results of this characterization are presented in Tab. 4.5.

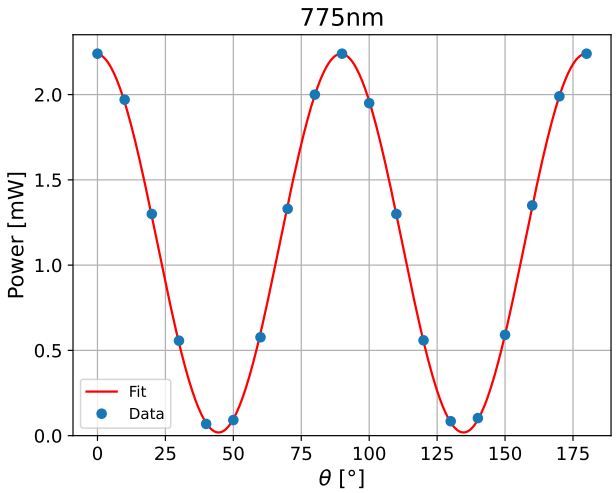

Figure 4.12: Characterization of the dHWP at 775nm.

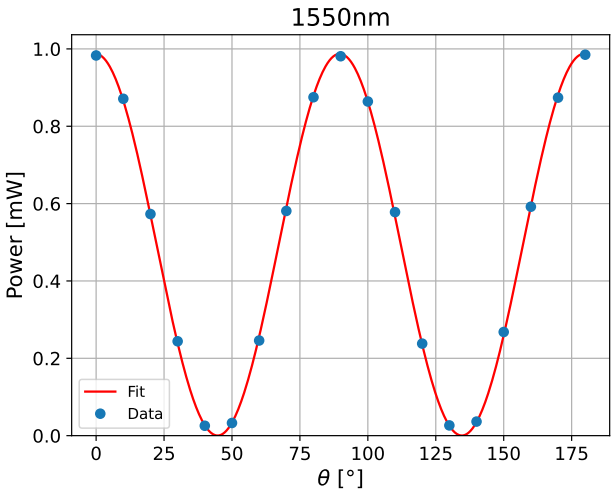

Figure 4.13: Characterization of the dHWP at 1550nm.

Wavelength [nm]	R	T
775	$5.12 \cdot 10^{-4}$	0.987
1550	$1.42 \cdot 10^{-3}$	0.982

Table 4.5: Characterization of the dHWP: extinction ratio and transmittance.

4.4 Source Optical Setup

After characterizing the optical elements, we proceeded with the realization of the source. During this phase, careful consideration of the limitations imposed by the breadboard dimensions (450 $\times$ 600 mm^2) is crucial. The XYZ translation stage's dimensions set a minimum size for the Sagnac loop. Conversely, the choice of the pump focusing lens (with a focal length of 250 mm) imposes a maximum size for the Sagnac loop to ensure the correct pump beam focusing inside the crystal. Addressing the requirements observed during the optical elements' characterization is also essential. To maximize the extinction ratio of the 1550nm light and enhance visibility, the dPBS needs to be tilted by 4°. Additionally, the XYZ translation stage allows for parallel movement along the string of holes in the breadboard but does not allow for tilting the crystal. As a result, the incident beam on the crystal inside the Sagnac loop must be parallel to this direction. In addition, we meticulously designed the source setup to facilitate the effortless replacement of lenses for both the pump and signal/idler photons. The setup has been constructed to accommodate lenses with focal lengths ranging from 250 mm to 450 mm. The entangled photons after exiting from the Sagnac loop are directed through two distinct channels (conventionally denoted as A and B) and they are consequently collected into optical fibers. To ensure a fine control of the fiber coupling of the emitted photons, we incorporated two mirrors for each channel. These mirrors play a crucial role in optimizing the fiber coupling process, enhancing the brightness and the heralding ratio. The final setup also integrates a HWP and QWP at 1550nm in front of each fiber output. These waveplates enable precise control of the polarization state of the photons. Such control is critical when using fibers to transport the entangled photons, as fibers can alter the photons' polarization. By adjusting these waveplates, one can compensate for the polarization changes induced by the fibers and set any maximally entangled state. To improve the quality of the entangled states, a liquid crystal (LCR) is introduced to correct a small phase within the range of $[0, 2\pi]$. This phase correction aims in compensating for a non-perfect alignment of the two paths in the Sagnac loop. The schematic of the final setup is illustrated in Fig. 4.14, and a photo of the experimental setup is shown in Fig. 4.15. This comprehensive setup achieves the desired control and stability required for generating entangled photons in a practical and efficient manner.

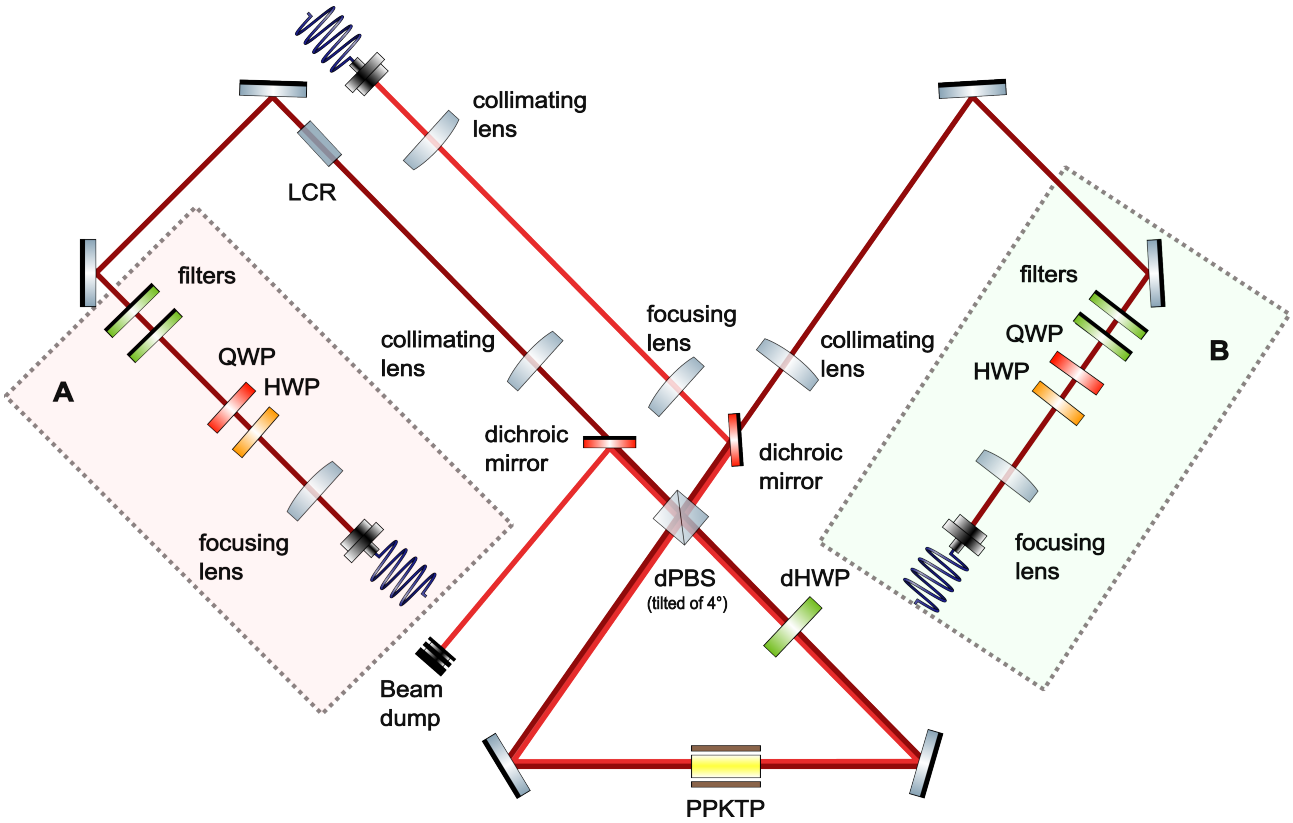

Figure 4.14: Schematic of the final design of the polarization-entangled photon source.

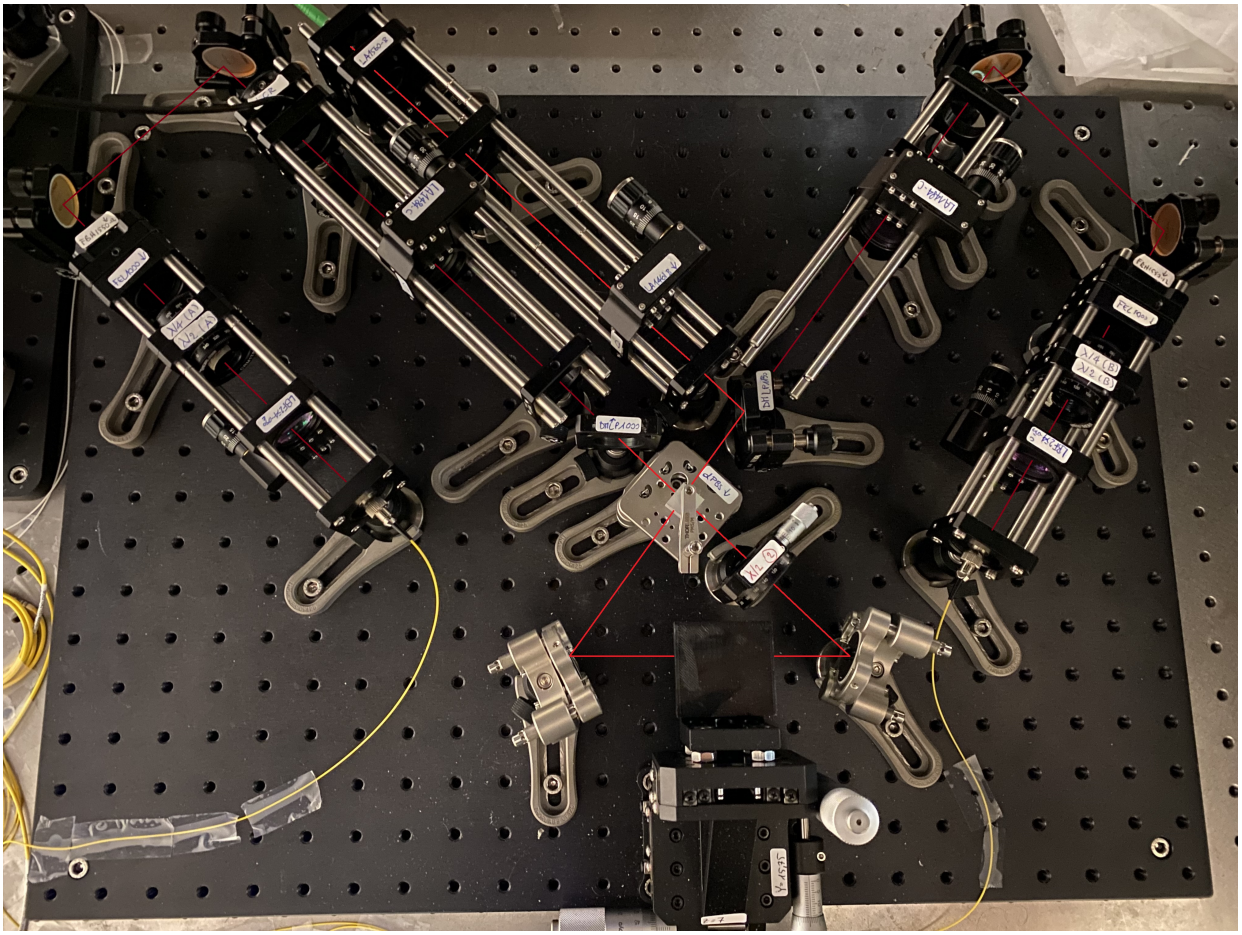

Figure 4.15: Photo of the source setup.

4.4.1 Sagnac Alignment

The first crucial step, after setting up the apparatus for collimating and focusing the pump beam, involves constructing the Sagnac loop. To ensure successful implementation, we must address specific constraints:

- The crystal must be positioned at the center of the Sagnac loop within the XYZ translation stage. As the crystal is aligned with a horizontal line of holes, and the translation stage lacks rotation capability, one arm of the Sagnac loop must be parallel to the crystal axis to properly direct the beam inside it.

- Proper orientation of the dPBS is essential to maximize the extinction ratio of the reflected beam at 1550 nm.

- The dimensions of the Sagnac loop must be chosen carefully to guarantee correct pump beam focusing and appropriate positioning of the dHWP inside it.

To overcome these challenges, the primary focus was on positioning the crystal and the dPBS. As the dPBS is tilted, special attention must be paid to the positioning of optical elements to avoid overlaps of optical components. In particular, special attention was given to the orientation of the beam exiting the dPBS and directed into channel A. In this situation, indeed, the support for the pump lenses and that of the downconverted photons would obstruct each other. In order to achieve the desired orientation, a 1550nm laser was employed, with its output positioned in front of the first mirror of channel A (where we intend to have the downconverted photons reflected). The laser was then directed toward the dPBS. The objective was to correctly orient the dPBS such that the output channel A coincided with that of the laser. To fine-tune the setup, a 1550nm PBS and HWP were introduced to linearly polarize the laser beam incident on the dPBS. The HWP angle was adjusted to minimize the intensity of light in the reflected branch of the dPBS. At this point, the dPBS was rotated to achieve maximum extinction in this branch. This way, we set up the dPBS so that the photons exiting from channel A were parallel to those coming from the pump. This alignment ensured that channel B became tilted, but it did not represent an issue as there was no risk of overlap with the other optical components (see Fig. 4.14).

The detailed procedure employed to construct and align the Sagnac loop is as follows:

1. Fix the altitude of the beam and ensure that all optical components maintain the beam's altitude.

2. Orient the 1550nm laser in such a way that it is parallel to the pump beam, crossing the dPBS in the middle of one of its faces.

3. To regulate the polarization of the laser, use a 1550nm PBS and an HWP. Then, proceed to rotate the dPBS until the extinction ratio on the reflected path is maximized (which occurs around 4°). Once the desired orientation is achieved, fix the position of the dPBS in place.

4. Adjust the dichroic mirror's position until the pump beam coincides with the 1550nm beam in both branches of the dPBS, and then secure that position.

5. The positioning of the mirrors is accomplished in two steps. Firstly, insert one of the mirrors such that the reflected beam is directed parallel to the crystal's orientation. Then, insert the second mirror to close the loop. This is possible if we observe that the two branches of the dPBS (clockwise and counterclockwise) coincide.

6. Insert the dHWP in a way that the reflection of the pump beam aligns as closely as possible with the original beam. This alignment is crucial to ensure that the waveplate is optimally positioned orthogonal to the incident beam. To correctly set the angle of the waveplate fast axis at 45° with respect to the state $|H\rangle$ (set by the dPBS), rotate the waveplate until the intensity of the pump beam exiting in channel A is minimized.

As the alignment of the Sagnac loop significantly affects the relative phase between photons traveling in the clockwise and counterclockwise paths, resulting in distinguishability and reduced entanglement, a second, finer, and more sophisticated procedure becomes essential. In this work, we utilized two methods to align the Sagnac loop:

- **Fiber recoupling method**: When the Sagnac loop is accurately aligned, and the dHWP's fast axis is set at 45°, all the light entering the loop exits through the input port (channel B) and is reflected back by the dichroic mirror to the pump fiber. We can take advantage of this property to effectively align the Sagnac loop by making adjustments to the configuration of the two mirrors to maximize the light that turns back and is recoupled into the pump fiber. This alignment process involves using a BS positioned in the polarization intensity controller to split the returning light from the input light. A successful alignment is achieved when the power of the light returning from the Sagnac loop reaches at least 25% of the initial power that entered the loop.
- **Interference method**: This method exploits the interference of the clockwise and counterclockwise paths at the dPBS. To make the two beams interfere, they must be projected into the same polarization state, which is possible by placing a polarizer in the reflected beam of the dichroic mirror in channel A. The method takes advantage of the non-optimal extinction ratio of the dPBS at 775nm, resulting in a residual pump beam that passes through channel A (although minimized by the dHWP configuration). If the two beams have the same direction and phase, constructive interference occurs. Otherwise, interference fringes are observed (see Fig. 4.16). These fringes can be horizontal or vertical, depending on the inclination of the beams at the dPBS. By analyzing the fringes, we can adjust the tip-tilt of the mirrors specifically until they disappear. When the Sagnac loop is perfectly closed, the phase difference is zero, and we achieve maximum constructive interference.

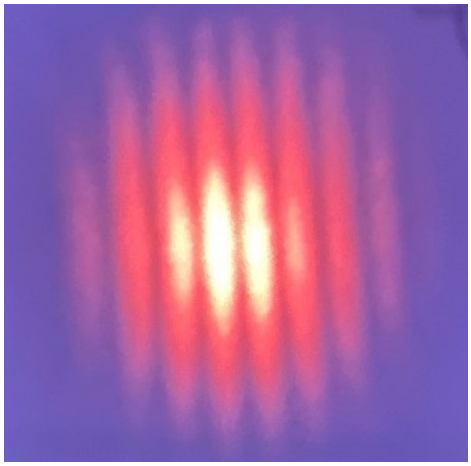

Figure 4.16: Interference pattern observed during the alignment procedure using the interference method.

Our main goal is to determine the arrangement of the mirrors such that the two paths of the Sagnac loop (clockwise and counterclockwise) overlap. The use of the interference method allows for correcting the tilt of the two beams that exit from channel A of the dPBS. However, there are several configurations that enable this overlap, and the method is unable to identify the optimal one. For this reason, the initial alignment phase is carried out using the fiber recoupling method, as it provides a clearer feedback about the correct mirror configuration. Subsequently, a fine-tuning alignment is performed by adjusting the mirrors slightly to correct any residual tilt between the two beams exiting from the dPBS. This fine adjustment procedure must be performed before starting any measurements since even small misalignments caused by thermal changes in the mirror positioning can significantly impact the quality of the generated entangled photons. For this reason, in this setup, we used high-quality POLARIS-K1S4 mirror mounts for the Sagnac loop, which guarantee long-term alignment stability. These mounts provide the necessary stability for precise fine-tuning and maintenance of the entangled photon source's optimal configuration.

4.4.2 Crystal Optimal Positioning

The model used to describe the SPDC process, as discussed in Chap. 2, assumes that the pump beam's waist is centered within the crystal. This assumption becomes crucial in the entangled photon source setup to ensure high performance. To thoroughly characterize the pump beam, a detailed analysis of its free-space propagation is essential, necessitating the extraction of the crystal from its support structure. As explained in Sec. 3.5.3, the position of the free-space waist anticipates the effective waist position of the beam propagating inside the crystal, and this difference is denoted by Δd as shown in Eq. (3.34). This condition is essential for both paths of the Sagnac loop: clockwise (CW) and counterclockwise (CCW).

To achieve this condition, we start by determining the position of the pump focusing lens that allows for a separation of approximately $2\Delta d \approx 8.5$ mm between the CW and CCW beams. Once we find the optimal position for the focusing pump lens, we can then adjust the position of the crystal using the XYZ translation stage. Firstly, we move the crystal along the beam direction to ensure its center coincides with the central point between the positions of the waists of the CW and CCW beams. Then, we adjust the other two degrees of freedom so that the beam passes through the center of the crystal, staying as far as possible from the external surfaces to avoid clipping (this procedure has been described in Sec. 4.1). The crucial point of the entire alignment procedure depends on the precise determination of these two focal point positions.

Knife Edge Method

The prevalent and direct technique for determining the laser beam radius uses CCD sensors, which provide a two-dimensional intensity profile of the beam's cross-section. These data are then fitted with a two-dimensional Gaussian to extract the beam radius. Nonetheless, this method encounters an issue: the CCD can not be positioned on the XYZ translation stage, preventing the establishment of a precise reference system for waist estimation. To address this, we have adopted the knife edge method, a technique that entails traversing a sharp-edged knife through the beam's cross-section and measuring the intensity of light transmitted as a function of the blade position. The main advantage of this approach is that the knife can be inserted into the same support structure of the crystal, thus linking the measured beam radius positions directly to the crystal's center position.

The intensity profile of an ideal Gaussian beam is defined as:

$$I(x,y) = I_0 \exp\left[-2\frac{(x-x_0)^2 + (y-y_0)^2}{w^2}\right] \tag{4.14}$$

Here, we assume symmetry along both the x and y axes (i.e., $w_x = w_y = w$). The knife edge method enables the assessment of the beam radius $w(z)$ at a specific location z along the propagation direction. For each position z, the knife is moved along the x-axis using an electronic micrometric controller connected to the XYZ translation stage. For each position, the photodiode is synchronized to capture the beam's intensity. A visual representation of this approach is provided in Fig. 4.17.

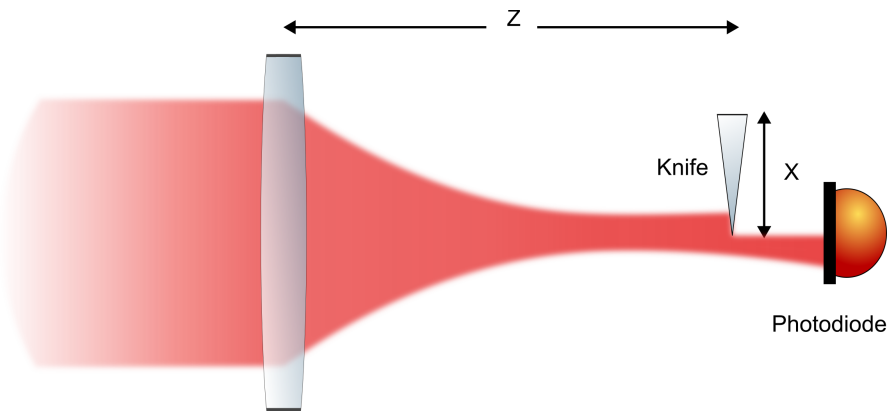

Figure 4.17: Schematic of the knife edge method.

The intensity of the beam, recorded when the blade obstructs the beam until $\bar{x}$, can be calculated using the following expression:

$$I(\bar{x}) = \int_{\bar{x}}^{+\infty} \int_{-\infty}^{+\infty} I(x,y)dxdy = \frac{I_0}{2}\left[1 - \text{erf}\left(\sqrt{2}\frac{(\bar{x}-x_0)}{w}\right)\right] \tag{4.15}$$

where the *error function* is defined as $\text{erf}(x) = \frac{2}{\sqrt{\pi}}\int_0^x e^{-t^2}dt$. The function in Eq. (4.15) forms the foundation for data fitting and for estimating the beam radius. The beam radius and the center of the beam x_0 serve as free parameters for the fitting process. An illustrative example of this fitting procedure is presented in Fig. 4.18. This process can be replicated for varying blade positions along the beam's propagation direction z, enabling the reconstruction of the complete beam profile. To describe the spatial variation of the Gaussian beam radius, the following formula can be employed:

$$w(z) = W_0\sqrt{1 + \left[\frac{(z-z_0)\lambda}{\pi W_0^2}\right]^2} \tag{4.16}$$

While theoretically the focus position z_0 and the waist W_0 could effectively characterize the beam's properties, this was not achievable in this particular case. The knife edge method encounters limitations near the focus, resulting in inaccuracies in determining the waist position. Specifically, the knife edge method failed to provide beam radius values below 70 μm near the waist. Moreover, an asymmetry is evident in the data trend prior to and after the beam focus, probably due to optical imperfections like aberrations and astigmatism. While this effect is relatively small, the fitting function in Eq. (4.16) cannot be applied here. Given that our primary goal is to estimate the focus position z_0, we opted to fit both datasets (CW and CCW) using a generic third-order polynomial function. We systematically scanned the beam radius at multiple positions, subsequently adjusting the pump lens until the separation between the two waists approached approximately $2\Delta d \approx 8.5$ mm (as depicted in Fig. 4.19). At this point, we reintroduced the crystal on the support and we positioned it such that its center coincided with the midpoint of these two waists.

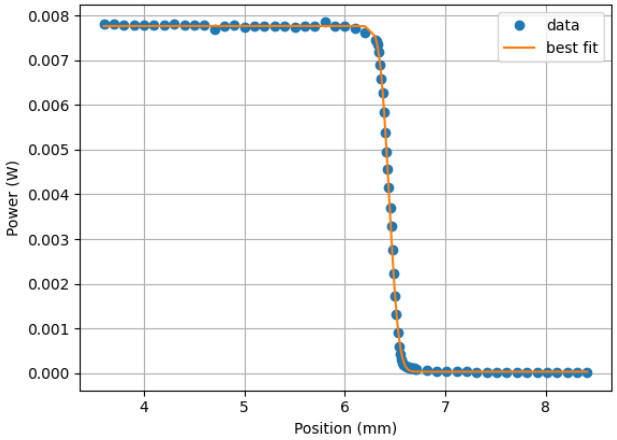

Figure 4.18: Example of fit used in the knife edge method for the estimation of the beam radius.

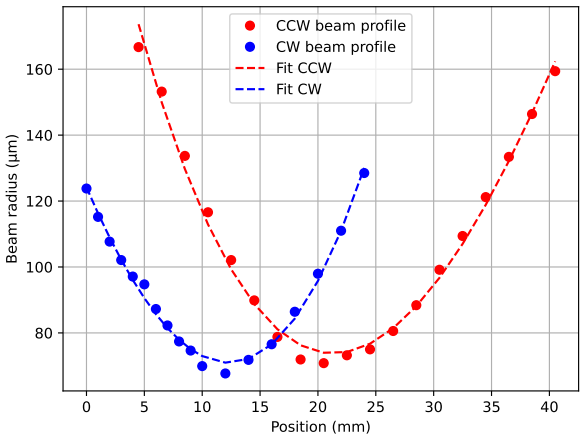

Figure 4.19: CW and CCW laser beam profiles in the optimal configuration of pump lens. These data are fitted with a third-order polynomial function to get the waist positions.

The alignment procedure just described allows for achieving good alignment, but it is affected by the uncertainty due to the knife-edge method. To further improve the alignment of the crystal, it is possible to leverage the symmetry between the CW and CCW beams. When the crystal is perfectly aligned, the CW and CCW beams appear symmetric. To achieve this configuration, we initially proceeded by finely adjusting the crystal's position using the micrometer screw of the XYZ translation

stage to center it within the Sagnac loop (this condition is achieved when the two beams incident on the crystal are symmetric). Subsequently, we precisely adjusted the position of the lens that focuses the pump photons in the crystal until the two beams (CW and CCW) overlap in the entire Sagnac loop.

4.4.3 Downconverted Photons Collection System

The emitted photons from the crystal are directed toward the two outputs of the Sagnac loop, channel A and channel B. These beams are subsequently collimated using the first set of lenses (with long focal lengths) and further guided into a second set of lenses (with short focal lengths), focusing the beams within optical fibers. The pivotal challenge lies in aligning this optical configuration to ensure the efficient collection of downconverted photons.

To achieve this, precise alignment of the two beam paths is essential. The lenses responsible for focusing the collimated beam into the fiber are initially positioned to collimate a 1550nm laser beam introduced through the fiber. The other lenses instead are approximately set at a distance corresponding to their focal length from the crystal center.

The procedure used to align the optical setup is the following:

1. In the context of collinear SPDC, the emitted beams share the same trajectory as the pump beam. This inherent symmetry aids in streamlining the alignment process. While the dichroic mirror in channel B remains fixed (it is used to direct the pump beam in the Sagnac loop), the dichroic mirror and the spectral filters of channel A are temporarily removed. The fast axis of the dHWP is rotated to maximize the intensity of the pump beam traversing channel A (which means that it is parallel to the state $|H\rangle$ or $|V\rangle$ set by the dPBS). This procedure permits the propagation of the 775nm beam up to the fiber of channel A. The initial alignment of channel A entails mirror adjustments to optimize fiber coupling. Notably, the coupling efficiency of the 775nm light is limited since the optics and the single-mode optical fiber are designed for transmitting 1550nm photons. However, this method is useful for obtaining a rough alignment of the setup.

2. An enhancement in alignment is achieved by injecting a 1550nm laser beam through the output fiber of channel A. The back-propagation technique is employed to align the 1550nm beam with its 775nm counterpart.

3. After successfully aligning channel A with the pump beam, the alignment focus shifts to channel B. Exploiting the experimental setup's symmetry, a 1550nm laser beam is injected into channel A's output fiber, maximizing the coupling efficiency of channel B. This procedure aids in achieving optimal alignment, facilitating improved positioning of the lenses with long focal lengths. Proper lens adjustment ensures correct beam focalization within channel B's fiber, thereby optimizing fiber coupling. Additionally, alignment ensures equality of beam radius of CW and CCW beams at the crystal interfaces for both 1550nm and 775nm beams.

4. Fine alignment is executed through the utilization of photon detection feedback. Thus, the output fibers of the source are connected to the SNSPDs, and meticulous adjustment of the QWP and HWP for each channel ensures the detectors' efficiency is maximized. After correctly setting the QWP and HWP, it is possible to proceed with the precise arrangement of the long focal length lenses and iterative mirror adjustments, all aimed at optimizing the collection of photon counts. This alignment procedure is conducted independently for each channel. For each lens position, the photon detection is maximized by manipulating the tip-tilt of the mirrors. Then, the lens is moved slightly to obtain a better coupling. When optimal fiber coupling is attained, even minor mirror adjustments yield a significant impact on photon detection.

5. For precise optimization, the positions of the shorter focal length lenses can be fine-tuned in conjunction with the adjustment of the mirrors in the Sagnac loop.

It is important to ensure during this phase that the beam is not clipped by the crystal. To verify it is sufficient to introduce a 1550nm laser into one of the two outputs and observe the beam in proximity

of the crystal interface. The aforementioned procedure was used for the first alignment of the source. However, it is essential to conduct periodic fine-tuning of mirror positions before any measurements.

4.4.4 Polarization Measurement Station

Performing polarization measurements on the generated biphoton states is essential to evaluate the source's performance. Such measurements enable the determination of entangled state visibilities, Bell tests, and quantum state tomographies. For this purpose, we have developed a polarization measurement station (see Fig. 4.20) comprising a sequence of QWPs, HWPs, and PBSs. These optical elements facilitate the execution of projective measurements on a complete set of mutually unbiased bases (as described in Sec. 1.3.1).

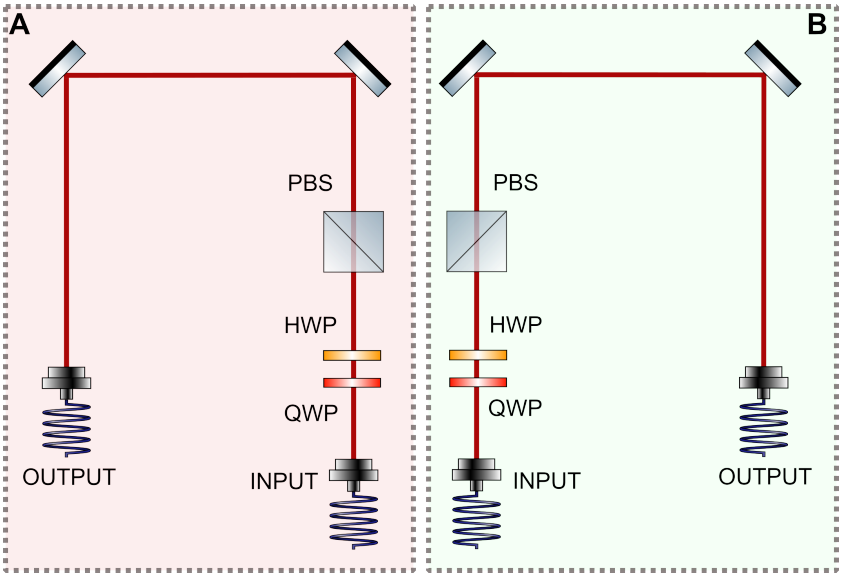

Figure 4.20: Schematic of the polarization measurement station. The two channels are denoted as Alice (A) and Bob (B), in agreement with the convection adopted for the source outputs.

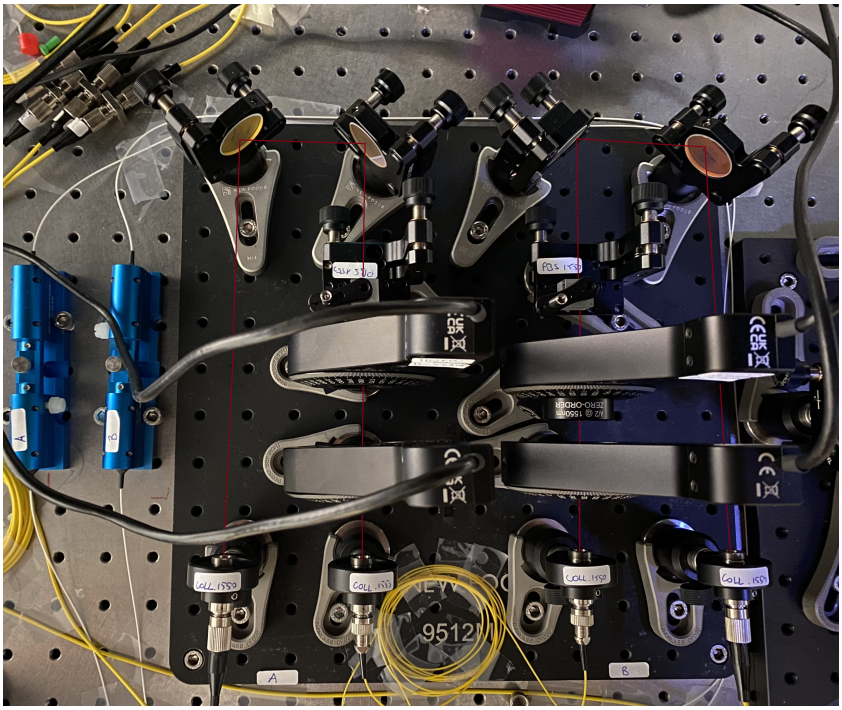

Figure 4.21: Photo of the polarization measurement station.

The photons emitted by the source are collected into single-mode optical fibers and subsequently directed to two 1550nm collimators. These collimators transform the incoming light from optical fibers into collimated beams through integrated lenses. The collimated beams then traverse the waveplates (QWP and HWP) as well as the PBS before being recollected by another set of collimators. Subsequently, the light passes through a polarization controller and is directed toward SNSPDs for measurement. To optimize SNSPD efficiency, polarization controllers are employed. The fiber coupling is maximized using two mirrors (the coupling efficiency, measured with a laser, is approximately $\approx 80\%$).

Depending on the specific application, either HWPs alone or a combination of HWPs and QWPs are employed. The QWPs, in particular, are exclusively used for complete quantum state tomography. In contrast, for assessing the visibilities of $\mathbb{Z}$ and $\mathbb{X}$ bases, as well as conducting Bell tests, only HWPs are utilized.

To simplify measurement operations and reduce statistical errors resulting from manual adjustments, electronic rotation mounts are employed. These mounts can be programmed to rotate to specific positions, while data are collected by the time tagger. When conducting polarization measurements, it is important to accurately determine the angle corresponding to the fast axis. This is achieved by introducing an additional PBS before the waveplate that establishes the $|H\rangle$ polarization. Following this, the waveplate (the same process applies to both HWP and QWP) is finely tuned until the light reflected by the second PBS is minimized. This ensures that the fast axis of the waveplate does not modify the linearly polarized state of the initial PBS, thus confirming proper alignment.

4.4.5 Liquid Crystal Retarder Alignment

In the previous sections, we delved into source alignment techniques that facilitate the generation of entangled photon pairs and optimize brightness and heralding ratio. As discussed in Sec. 3.6, the state of the photons emitted by the source is:

$$|\psi\rangle = \frac{1}{\sqrt{2}}(|HV\rangle + e^{i\phi}|VH\rangle) \tag{4.17}$$

Here, ϕ denotes a relative phase induced by various factors such as the dHWP, disparities between the CW and CCW paths of the Sagnac loop, and the initial relative phase between the $|H\rangle$ and $|V\rangle$ components of the pump beam. These combined phases contribute to a reduction of entanglement. A maximally entangled state is achieved when $\phi = 0$. In the original work by Kim et al. [62], the authors proposed to compensate for this relative phase by properly selecting the pump beam's polarization. However, the pump beam's polarization is also leveraged to balance the $|HH\rangle$ and $|VV\rangle$ states. Even if it is feasible to appropriately configure the pump beam's polarization to establish the correct amplitude and relative phase, this process can be practically intricate. In our setup, we employ the pump solely to achieve suitable balancing between the two components, while compensating for the relative phase utilizing a liquid crystal retarder (LCR).

In this source, we utilized the LCC-1413-C (Thorlabs). The operational principle of a LCR is depicted in Fig. 4.22.

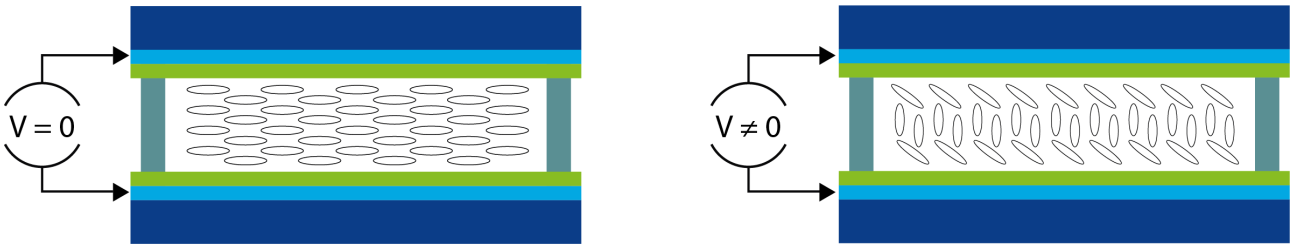

Figure 4.22: Operating principle of the liquid crystal variable retarder. In the absence of an external electric field, the crystal is in the nematic phase (left). The molecules are aligned along an axis that coincides with the optical axis of the LCR. When an external electric field is applied (right), the orientation of the molecules tilts, introducing a distinct phase shift between the optical axis and its orthogonal component.

This device functions by exploiting controlled molecular orientation within a liquid crystal material to modulate the phase of polarized light as it passes through. In the nematic phase (when no voltage is applied), liquid crystal molecules are orderly and exhibit an elongated shape, leading to optical anisotropy. The application of an electric field induces alignment of the molecules with the field, and the degree of birefringence is regulated by the tilting of the liquid crystal molecules. The orientation of these molecules is controlled through applied voltage, allowing dynamic manipulation of the retardance.

The LCR operates as a variable waveplate, introducing a phase denoted as θ, which can be controlled by an external electric field, to the component orthogonal to the fast axis. Acting as a local phase-shift operator within one of the subsystems, when the LCR is positioned in channel A (as illustrated in Fig. 4.14), its effect can be represented as $\hat{\mathcal{O}}_\theta^A \otimes \mathbb{I}^B$, where:

$$\hat{\mathcal{O}}_\theta^A = \begin{pmatrix} 1 & 0 \\ 0 & e^{-i\theta} \end{pmatrix} \tag{4.18}$$

This expression holds when the optical axis of the LCR aligns with the $|H\rangle$ state of the dPBS, which establishes the reference frame for defining the emitted states from the source. Consequently, the application of this local operator to the biphoton state emerging from the dPBS results in:

$$|\psi_\theta\rangle = \begin{pmatrix} 1 & 0 & 0 & 0 \\ 0 & 1 & 0 & 0 \\ 0 & 0 & e^{-i\theta} & 0 \\ 0 & 0 & 0 & e^{-i\theta} \end{pmatrix} \begin{pmatrix} 0 \\ 1 \\ e^{i\phi} \\ 0 \end{pmatrix} = \begin{pmatrix} 0 \\ 1 \\ e^{i(\phi-\theta)} \\ 0 \end{pmatrix} \tag{4.19}$$

Setting the LCR phase to $\theta = \phi$ yields the maximally entangled state $|\psi_\phi\rangle = |\Psi^+\rangle$.

The alignment procedure for the LCR's optical axis with the $|H\rangle$ state emitted by the dPBS is the following:

- A 1550nm laser beam is introduced into the source through output B, and the dHWP within the Sagnac loop is precisely tuned to completely direct the beam towards path A of the dPBS. This configuration enables the light to be transmitted into channel A (where the LCR is placed), and it exhibits linear polarization corresponding to the $|H\rangle$ state of the dPBS..
- The LCR is temporarily removed, and the light collected in path A is transmitted via optical fiber to the polarization measurement station (Fig. 4.20).
- The QWP and HWP of channel A are manipulated to alter the polarization state of the output beam, which then enters the polarization station (comprising only a PBS in this case). The waveplates convert the $|H\rangle$ state of the dPBS in the Sagnac loop into the $|V\rangle$ state selected by the PBS in the polarization measurement station. In this way, the light transmitted by the PBS is minimized.
- The LCR is reinserted, maintaining fixed positions for the QWP and HWP. The LCR is rotated until the intensity of the light collected after the polarization station is minimized. In this configuration, the optical axis of the LCR is parallel to the incoming state and it does not modify the polarization of the incident light.

In the following section, we will describe how the compensation of the relative phase is achieved using the LCR to maximize the quality of the entangled photons.

4.4.6 Generation of the Entangled States

The primary aim of the source is to emit entangled photons. So far, we've explored diverse strategies to optimize brightness and heralding ratio. Here, we present the procedure employed for emitting entangled states. The initial objective of this process is to compensate for polarization changes induced by the fibers and establish the entangled state in relation to the $\{|H\rangle, |V\rangle\}$ states defined by

the PBSs within the polarization measurement station. Subsequently, we need to balance the $|HH\rangle$ and $|VV\rangle$ components of the emitted states, which depend on the polarization state of the pump beam. Finally, compensating for the relative phase using the LCR becomes necessary. In the following, we will delve into the procedure for preparing the Bell state $|\Phi^+\rangle$ (a similar approach can be adapted for emitting other Bell states as well):

1. **Setting a separable state**: Optical fibers modify the polarization state of photons emitted from the source. As an initial step, compensating for the polarization-altering effects induced by the fibers is crucial, ensuring the accurate definition of the entangled state within the polarization measurement system. However, to achieve this, it is advantageous to manipulate separable states, as it simplifies the process by enabling modifications to a subset of the system while leaving the other part unchanged. Consequently, the first step involves configuring the source to emit separable states. This is achieved by adjusting the polarization of the pump beam to enable light circulation along a single path within the Sagnac loop. Typically, this adjustment involves minimizing the light within the transmitted path of the dPBS, which exhibits a higher extinction ratio.

2. **Polarization adjustments**: For this procedure, the HWPs in the polarization measurement station are utilized. The separable state emitted by the source (initially of the form $|V\rangle_A |H\rangle_B$ within the source's reference frame set by the dPBS) needs to be converted to the separable state $|H\rangle_A |H\rangle_B$ within the reference frame of the polarization measurement system, established by the two PBSs. This can be achieved by performing a projective measurement on the state $|H\rangle_A |V\rangle_B$ in the polarization measurement station. Subsequently, the QWP and HWP for channel B of the source are manipulated until the coincidence counting rate is minimized. Similarly, the polarization measurement station can be set to measure the state $|V\rangle_A |H\rangle_B$, followed by minimizing the coincidence counting rates by appropriately adjusting the QWP and HWP for channel A of the source.

3. **Balancing of the entangled state**: Now, the state emitted by the source in the measurement station is $|H\rangle_A |H\rangle_B$. To achieve the maximally entangled state, the polarization of the pump beam is adjusted by manipulating the QWP and HWP of the polarization controller system. This procedure is performed until the coincidence counting rate of the projected state $|H\rangle_A |H\rangle_B$ matches the coincidence rate for measuring the state $|V\rangle_A |V\rangle_B$. In this configuration, coincidence rates for the measured states $|H\rangle_A |V\rangle_B$ and $|V\rangle_A |H\rangle_B$ are still minimized. This brings the emitted state into the form $\left|\tilde{\Phi}^+\right\rangle = \frac{1}{\sqrt{2}}(|H\rangle_A |H\rangle_B + e^{i\phi} |V\rangle_A |V\rangle_B)$.

4. **LCR compensation**: To achieve the maximal entangled state $|\Phi^+\rangle$, the relative phase ϕ between the two components $|H\rangle_A |H\rangle_B$ and $|V\rangle_A |V\rangle_B$ within the emitted state $\left|\tilde{\Phi}^+\right\rangle$ must be removed. This is accomplished by enhancing the visibility in the $\mathbb{X}$-basis. To achieve this, the HWPs of the polarization measurement station can be adjusted so that the projected state is $|D\rangle_A |A\rangle_B$ (or equivalently, $|A\rangle_A |D\rangle_B$), and the applied voltage of the Liquid Crystal Retarder (LCR) is manipulated until the coincidence counting rate of detected photons is minimized.

4.4.7 Lens Replacement Procedure

We conclude this chapter by describing the procedure to replace lenses in the source setup. In general, this procedure is not necessary; however, it was employed for the specific characterization we aimed to perform, focused on quantifying the impact of various lenses on the performance of the SPDC process. Specifically, in this thesis, we have studied how the performance of the source changes as a function of the lenses used to collect the downconverted photons. The comprehensive procedure for replacing both sets of lenses for the 1550nm photons is as follows:

1. Replace one of the two short focal length lenses utilized to focus the collimated 1550nm beam into the fiber (for example, we assume in channel A). During this step, it is necessary to accurately position the lens to ensure proper collimation of the 1550nm beam as it emerges from the optical fiber.

2. Introduce a 1550nm laser beam from the opposite channel (B) and configure the dHWP within the Sagnac loop to direct the light exiting from the interferometer into channel A. This configuration allows us to precisely adjust the mirrors of channel A in order to maximize fiber coupling. It is important to recognize that the focusing lens remains unaltered, resulting in beam focusing within the crystal but with a distinct beam waist in comparison to the beam from the opposite branch. As a consequence, even though the setup is aligned, we cannot obtain high fiber coupling efficiencies.

3. A more accurate approach to align the setup involves directly introducing a 1550nm laser beam into channel A. In this scenario, we can meticulously refine the mirror positions to ensure precise overlap between the pump beam and the 1550nm beam. Assuming the previous step has been executed accurately, this fine-tuning alignment can be rapidly achieved through minor adjustments.

4. Employ the procedure described in steps 1-3 for the replacement of the short focal length lens in the opposite channel. Since channel B alignment relies on channel A alignment, slight misalignments in the latter can also impact the former. As in the previous cases, a meticulous fine adjustment using back-propagation is necessary.

5. Finally, the focusing lenses can be replaced and positioned at a distance corresponding to their respective focal lengths from the crystal. Subsequently, a meticulous fine adjustment can be performed to optimize both the brightness and heralding ratios following the procedure described in Sec. 4.4.3.

Chapter 5

Results

In this chapter, we discuss the main results derived from the source's characterization. We evaluated four distinct optical setups, each presenting a unique configuration for collecting downconverted photons. For each configuration, we present a comprehensive analysis of the source's performance, focusing on brightness, heralding ratio, and visibility of the emitted states through polarization measurements in both the $\mathbb{Z}$ and $\mathbb{X}$ bases. The source has been tested in both the regimes of the pump laser: continuous wave (CW) and pulse modes. Subsequently, the experimental results are compared with simulations of the SPDC process, taking into account the losses of the experimental apparatus. Additionally, the model describing the emitted photon states is validated through a comparison with the results obtained from Bell inequality violations and quantum state tomography of the emitted states. Lastly, we investigate the relationship between emitted photon visibility and pump beam power, a crucial characteristic for specific source applications.

5.1 Analysis of the Coincidences

All the results presented in this chapter are based on the analysis of coincidences among signals acquired from the two channels of the SNSPDs. As outlined in Sec. 4.1, the electrical signals derived from the single photon detections are directed to the time tagger. This instrument records the arrival times of each signal in relation to an internal clock with a temporal resolution of 42 ps (standard deviation jitter). Our program processes the time tags received from each channel, initiating a real-time analysis that provides the single-channel counting rates and the coincidence counting rates. For each pair of events (one from each channel), the temporal difference between the time tags is computed and then visualized in a histogram (see Fig. 4.3). These events follow a Gaussian distribution centered around the mean value of the time differences between events collected in the two channels. This is caused by the distinct optical components and optical fibers used in the two channels to transmit photons from the source to the detectors. Consequently, the photons (which are generated simultaneously in the SPDC process), before being detected, experience a different delay depending on the specific channel in which they are collected. To facilitate the analysis, we introduce a fixed delay to the temporal differences to ensure that the mean of the time differences distribution is centered at zero. At this point, to assess coincidences, the program utilizes a designated coincidence window. Events having a time difference falling within the coincidence window are considered coincident. Given the high temporal resolution of the time tagger, we have chosen a coincidence window of 0.25 ns for the entire experiment.

The count of coincidences may not always provide a comprehensive characterization of events. Particularly, at elevated coincidence counting rates, the single-photon detectors manifest saturation effects, necessitating careful consideration (refer to Eq. (3.2)). These effects arise due to the inherent dead time of SNSPDs (approximately 100 ns).

Another crucial consideration when evaluating the coincidence counting rate is the presence of accidental events. These events arise from the multiple pairs emission of SPDC photons within short time intervals: this leads to considering as events the coincidences between two photons originated from distinct SPDC processes. Given the low interaction probability of this process, these events

become increasingly significant with the increase in pump beam power. The rates of accidental coincidences can be estimated using Eq. (4.2) in CW regime and Eq. (4.3) in pulse mode.

To assess brightness and the heralding ratio (refer to Sec. 5.2), we exclude accidental events, as our focus is on characterizing the SPDC process and comparing it with the theoretical model. However, for visibility measurements (Sec. 5.3), the analysis is conducted using raw coincidence data. This is because removing accidental events would invalidate the results of several relevant experiments, such as Bell-inequality-violation measurements.

5.2 Brightness and Heralding Ratio

In this section, we provide the experimental results for the brightness and heralding ratio measurements in each source configuration. By quantifying the experimental losses for each channel of the source, we can determine the actual values of brightness and heralding ratio. This procedure allows us to conduct a comparison between the experimental results and the simulations.

5.2.1 Losses

When examining experimental results, a pivotal parameter to investigate is the apparatus' level of losses. This factor holds particular significance in evaluating the source's performance. The main contributions are:

- The transmission of the crystal, which is $\eta_{CRY} = 0.937$.
- The optics' transmission efficiency (ϵ_{optics}).
- The optical fibers' efficiency (ϵ_{fibers}).
- The SNSPDs efficiency (ϵ_{SNSPD}), which as detailed in Appendix C is different for each channel.

To assess the losses of the experimental apparatus we followed an approach similar to that described in Sec. 4.1. The transmission efficiencies of each channel are evaluated through Eq. (4.5). The results are presented in Tab. 5.1.

Channel	ϵ_{optics}	ϵ_{fibers}	ϵ_{SNSPD}	$\epsilon_{TOT}^{A/B}$
A	0.698	0.921	0.779	0.485
B	0.727	0.802	0.704	0.397

Table 5.1: Transmission efficiency of the components in the final source experimental setup.

5.2.2 Simulation Results

For each optical configuration of the source, we performed a simulation to estimate the theoretical brightness ($R_{si(th)}$) and the signal/idler heralding ratios ($\eta_{s(th)}$ and $\eta_{i(th)}$), both in CW and pulse regimes of the pump beam. In these simulations, we neglected the losses of the experimental apparatus. The methodology employed is similar to the one described in Sec. 4.2.

$f_1^{s,i}$[mm]	$f_2^{s,i}$[mm]	$R_{si(th)}^{(CW)}$	$\eta_{s(th)}^{(CW)}$	$\eta_{i(th)}^{(CW)}$	$R_{si(th)}^{(pulse)}$	$\eta_{s(th)}^{(pulse)}$	$\eta_{i(th)}^{(pulse)}$
40	250	171056	0.757	0.775	171059	0.757	0.774
50	300	173599	0.760	0.778	173603	0.760	0.778
40	300	149639	0.719	0.732	149644	0.719	0.732
50	250	174926	0.756	0.777	174937	0.756	0.777

Table 5.2: Simulations of brightness and heralding ratio for different source configurations. The pump beam power is fixed to 10 mW.

In this case, the waist values used in these simulations for the pump, signal, and idler photons are

those outlined in Tab. 3.4, which depend on the particular combination of the lenses used to collect the downconverted photons. The pump beam power's reference value is 10 mW.

5.2.3 Experimental Results

The photons emitted in each channel can be found either in the state $|H\rangle$ or $|V\rangle$ based on the Sagnac path (clockwise or counterclockwise) they originate from. This duality poses a challenge in accurately measuring both brightness and the heralding ratio since optimizing the SNSPDs' efficiency to incident photon polarization for both polarization states is not feasible. To achieve precise assessments, it becomes fundamental to establish a separable state wherein the two channels receive photons with predetermined polarization. This necessitates minimizing the light passing through one of the Sagnac loop paths. By reducing the transmitted path of the dPBS, which possesses a higher extinction ratio, we achieved the desired separable state $|V\rangle_A |H\rangle_B$.

Background noise from each channel was subtracted, and only counts without accidental events were considered for count correction. Furthermore, we set the pump beam power to a reference value of 10 mW (this allows us to compare the experimental results with the simulations). The experimental brightness ($R_{si(exp)}$) and the signal/idler heralding ratios ($\eta_{s(exp)}$ and $\eta_{i(exp)}$), both in CW and pulse regimes are presented in Tab. 5.4.

Calculating the uncertainty of these results proves challenging due to multiple factors in addition to statistical fluctuations (which follow Poissonian statistics), such as laser instability, source alignment, and environmental conditions. To assess these contributions, multiple measurements were conducted on different days, providing insights into the repeatability of the measurements. The estimated uncertainties for brightness ($\sigma_{R_{si}}$), single-channel counting rates (σ_{R_s} for signal and σ_{R_i} for idler), and heralding ratios (σ_{η_s} for signal and σ_{η_i} for idler) are: $\sigma_{R_{si}} \approx 1000$ pairs/s, $\sigma_{R_s} \approx \sigma_{R_i} \approx 5000$ pairs/s, and $\sigma_{\eta_s} \approx \sigma_{\eta_i} \approx 0.5\%$.

$f_1^{s,i}$[mm]	$f_2^{s,i}$[mm]	$R_{si(exp)}^{(CW)}$	$\eta_{s(exp)}^{(CW)}$	$\eta_{i(exp)}^{(CW)}$	$R_{si(exp)}^{(pulse)}$	$\eta_{s(exp)}^{(pulse)}$	$\eta_{i(exp)}^{(pulse)}$
40	250	46500	0.262	0.240	45800	0.261	0.239
50	300	37200	0.248	0.203	36500	0.251	0.202
40	300	30200	0.238	0.186	30100	0.237	0.187
50	250	35600	0.205	0.195	33600	0.205	0.195

Table 5.3: Experimental results of brightness and heralding ratio for different source configurations. The pump beam power is fixed to 10 mW.

To compare the experimental results (Tab. 5.3) with the simulations (Tab. 5.2), we need to consider the experimental losses of each channel (Tab. 5.1) which are denoted as ϵ_{TOT}^A (for channel A, where the idler photons are collected) and ϵ_{TOT}^B (for channel B, where the signal photons are collected). They influence both the brightness and the heralding ratio by reducing the experimental performance of the source. For this reason, we estimated the effective experimental performance of the SPDC process (which would be achieved without experimental losses) as follows:

- **Effective brightness**: The experimental brightness is evaluated by the coincidence counting rate of two lossy channels. As a consequence, the effective brightness can be estimated as $R_{si} = \frac{R_{si(exp)}}{\epsilon_{TOT}^A \epsilon_{TOT}^B}$.
- **Effective heralding ratio**: The effective single-channel counting rates are derived by the experimental values, which are solely influenced by the losses in the respective photon-collection channels, as $R_s = \frac{R_{s(exp)}}{\epsilon_{TOT}^B}$ and $R_i = \frac{R_{i(exp)}}{\epsilon_{TOT}^A}$. The effective heralding ratios are estimated by the ratio of the effective brightness and the effective single-channel counting rates: $\eta_s = \frac{\eta_{s(exp)}}{\epsilon_{TOT}^A}$ and $\eta_B = \frac{\eta_{i(exp)}}{\epsilon_{TOT}^B}$.

We can now proceed to compare the experimental results with the simulations (see Figs. 5.1 and 5.2). While the theoretical model provides a general insight into the brightness trends for the second,

third, and fourth configurations, it does not yield precise quantitative outcomes. This inaccuracy can be attributed to various factors, including both approximations within the model and experimental uncertainties. As discussed in Chap. 2, the theoretical model incorporates simplifications, such as assuming an infinitely large transverse area of the crystal in Eq. (2.45), to simplify the spatial mode overlap calculation. Moreover, the model assumes perfectly Gaussian modes. However, our observations, as detailed in Sec. 4.4.2, using the knife-edge method, indicate that optical elements introduce slight modifications to the pump beam. Additionally, it is important to note that the pump beam's spectral density is assumed to conform to a Gaussian distribution which might not be exactly the case in reality.

From an experimental perspective, achieving precise alignment presents a challenge due to the multitude of interdependent parameters at play. These parameters encompass the polarization and wavelength of the pump beam, accurate positioning of lenses, meticulous adjustment of mirrors, and various other contributing factors. While certain alignment procedures can be optimized, the absence of a clear feedback mechanism complicates the determination of when the optimal source condition has been achieved. Furthermore, we cannot accurately estimate the coupling efficiency, a crucial factor influencing both experimental brightness and heralding ratio. By comparing the actual experimental heralding ratios with the simulations (Fig. 5.2), it can be observed that the experimental values fall within the range of 45% to 60%, while the corresponding theoretical values vary between 70% and 80%. This indicates a reduction ranging from 65% to 80% (depending on the specific configuration) of the experimental values compared to the theoretical ones. This factor could be explained by the coupling efficiency, which, as previously observed, would result in a multiplicative factor in the overall transmission efficiency of the individual channel.

We have seen that the model's predictive accuracy is compromised by several uncertainties. In the future, to better comprehend the potentials and limitations of this model, it would be advisable to carry out multiple tests in various configurations. The model can serve as a foundational starting point for developing a more sophisticated framework that accommodates these non-ideal effects.

$f_1^{s,i}$[mm]	$f_2^{s,i}$[mm]	$R_{si}^{(CW)}$	$\eta_s^{(CW)}$	$\eta_i^{(CW)}$	$R_{si}^{(pulse)}$	$\eta_s^{(pulse)}$	$\eta_i^{(pulse)}$
40	250	241000	0.540	0.605	238000	0.539	0.602
50	300	193000	0.511	0.511	190000	0.516	0.507
40	300	157000	0.490	0.469	156000	0.488	0.471
50	250	185000	0.422	0.490	175000	0.422	0.490

Table 5.4: Effective brightness and heralding ratio for various source configurations derived from the experimental results, taking into account the experimental losses.

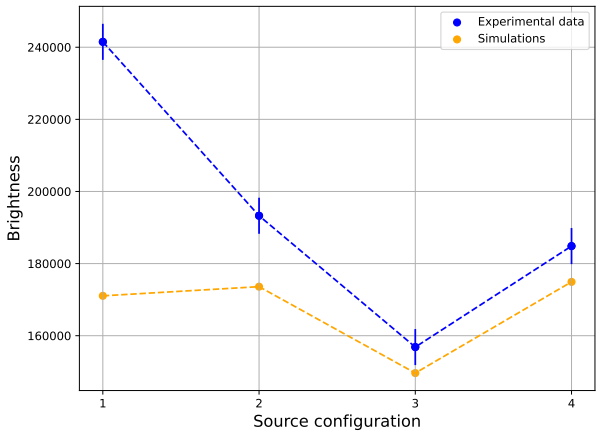

Figure 5.1: Comparison between the expected brightness from simulations and the experimental brightness for each source configuration.

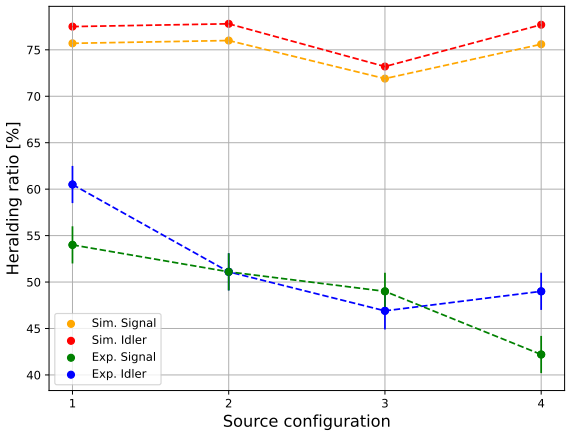

Figure 5.2: Comparison between the simulated heralding ratios and the experimental heralding ratios for each source configuration.

5.3 Measurement of Visibilities

To assess the quality of the produced entangled states, visibilities are measured in the $\mathbb{Z}$ and $\mathbb{X}$ bases for each source configuration. To achieve high-quality entangled states, it is crucial to precisely execute the procedure outlined in Sec. 4.4.3. In this case, we produced the Bell state $|\Phi^+\rangle$. In particular, we expect, based on the crystal characterization (Sec. 4.1.2), that the maximum visibility of the separable state in the $\mathbb{Z}$-basis is approximately 99.7%. This value has been regarded as a target in maximizing the visibility in the $\mathbb{Z}$-basis.

The analysis has been conducted for both CW and pulsed regimes, employing a pump beam power of 10 mW. For this analysis, we did not eliminate the accidental counting rates, as our aim is to characterize the source's properties for practical applications. The outcomes are presented in Tab. 5.5. Figs. 5.3, 5.4, 5.5, and 5.6 illustrate scans depicting how the coincidence counts (with an exposure time of 10 seconds) vary with different polarization angles of one of the two photons while keeping the other fixed (state $|H\rangle$ or $|D\rangle$). These results were obtained in the CW regime, which provides greater stability. The experimental results confirm that the source produces high-quality entangled states (these results will be discussed further in Secs. 5.4 and 5.5).

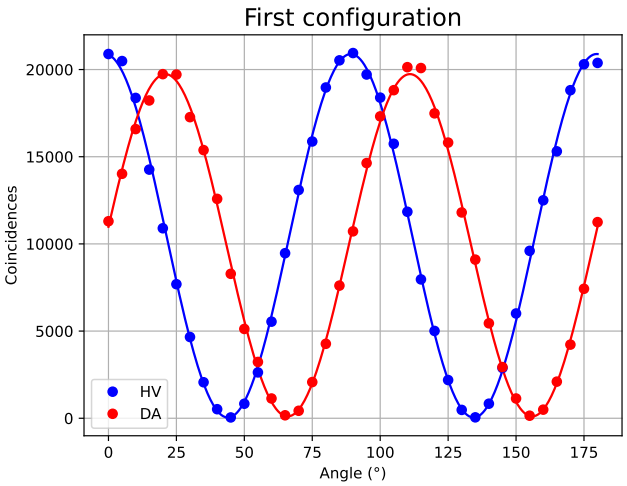

Figure 5.3: Scan of visibility in $\mathbb{Z}$ and $\mathbb{X}$ bases (first configuration): $f_1^{s,i} = 40$ mm, $f_2^{s,i} = 250$ mm.

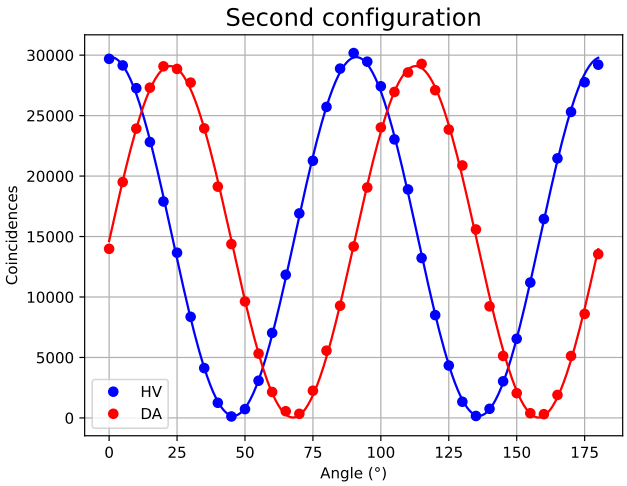

Figure 5.4: Scan of visibility in $\mathbb{Z}$ and $\mathbb{X}$ bases (second configuration): $f_1^{s,i} = 50$ mm, $f_2^{s,i} = 300$ mm.

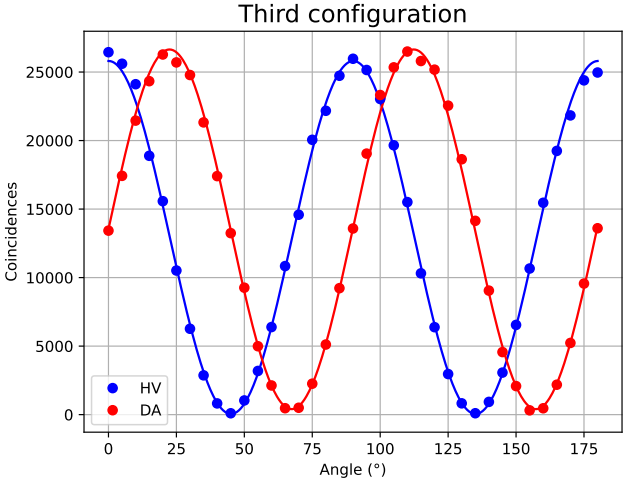

Figure 5.5: Scan of visibility in $\mathbb{Z}$ and $\mathbb{X}$ bases (third configuration): $f_1^{s,i} = 40$ mm, $f_2^{s,i} = 300$ mm.

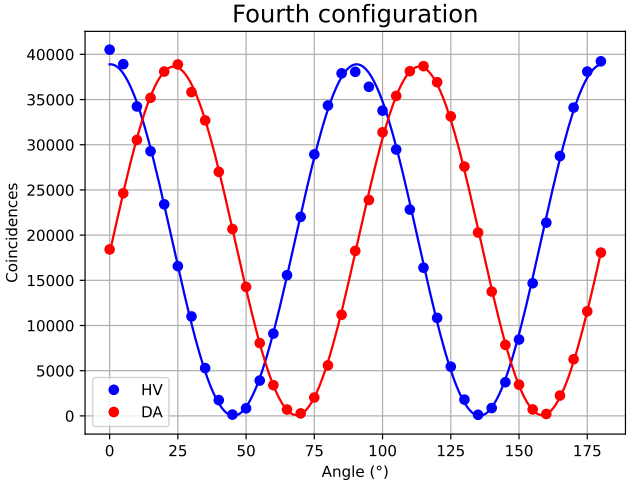

Figure 5.6: Scan of visibility in $\mathbb{Z}$ and $\mathbb{X}$ bases (fourth configuration): $f_1^{s,i} = 50$ mm, $f_2^{s,i} = 250$ mm.

$f_1^{s,i}$[mm]	$f_2^{s,i}$[mm]	$V_{\mathbb{Z}}^{(CW)}$	$V_{\mathbb{X}}^{(CW)}$	$V_{\mathbb{Z}}^{(pulse)}$	$V_{\mathbb{X}}^{(pulse)}$
40	250	$(99.53 \pm 0.03)\%$	$(99.10 \pm 0.04)\%$	$(98.48 \pm 0.06)\%$	$(97.38 \pm 0.08)\%$
50	300	$(99.34 \pm 0.02)\%$	$(98.79 \pm 0.03)\%$	$(98.16 \pm 0.03)\%$	$(97.60 \pm 0.04)\%$
40	300	$(99.21 \pm 0.03)\%$	$(98.29 \pm 0.05)\%$	$(98.02 \pm 0.05)\%$	$(97.14 \pm 0.06)\%$
50	250	$(99.38 \pm 0.02)\%$	$(98.79 \pm 0.03)\%$	$(98.39 \pm 0.04)\%$	$(97.21 \pm 0.06)\%$

Table 5.5: Visibilities measured in $\mathbb{Z}$ and $\mathbb{X}$ bases. These values were estimated from the maximum and minimum coincidence counts measured in the $\mathbb{Z}$ and $\mathbb{X}$ bases (as described in Sec. 1.5.1). The uncertainties were evaluated by propagation, assuming Poisson error on photon counts.

The visibilities measured in the $\mathbb{Z}$-basis are slightly higher than those obtained in the $\mathbb{X}$-basis. This suggests that a slight distinguishability between the two paths of the Sagnac loop remains. Moreover, the results in pulse mode reveal that the raw visibilities in both bases are consistently lower than those in CW. This difference arises due to the increased occurrence of accidental coincidences in the pulse mode, resulting in higher counting rates in the minima (a comprehensive analysis of how visibility is affected by accidental counts is presented in Sec. 5.6). Furthermore, we observe that there is no evident dependence of the visibilities on the source configuration. Discrepancies in the results can be attributed to the precision of the apparatus alignment, such as the Sagnac loop and the waveplates used to set the state in the polarization measurement station.

5.4 Quantum State Reconstruction

The states emitted by the source deviate from the ideal one $|\Phi^+\rangle$ due to numerous factors, such as decoherence and depolarization. A characterization of the states effectively emitted by the source holds significant importance, as it enables us to quantitatively assess the extent of these phenomena. In Sec. 1.6.2, we introduced a model to describe the experimental states. In this model, the effective state of the emitted photons is represented as a mixed state defined by two parameters, p and c (see Eq. (1.93)). These parameters can be directly deduced from the visibilities in the $\mathbb{Z}$ and $\mathbb{X}$ bases (Eq. (1.98)). The results are presented in Tab. 5.6.

$f_1^{s,i}$[mm]	$f_2^{s,i}$[mm]	$p^{(CW)}$	$c^{(CW)}$	$p^{(pulse)}$	$c^{(pulse)}$
40	250	0.0047 ± 0.0003	0.0043 ± 0.0005	0.0090 ± 0.0006	0.011 ± 0.001
50	300	0.0066 ± 0.0002	0.0055 ± 0.0004	0.0184 ± 0.0003	0.0056 ± 0.0005
40	300	0.0079 ± 0.0003	0.0092 ± 0.0006	0.0171 ± 0.0005	0.0088 ± 0.0008
50	250	0.0062 ± 0.0002	0.0059 ± 0.0004	0.0121 ± 0.0004	0.0118 ± 0.0007

Table 5.6: Experimental estimation of the p-c parameters used for the characterization of the emitted states.

From these values, we can reconstruct the quantum state of the photons emitted by the source using the p-c model, and specifically, we can estimate the fidelity between these states and the ideal Bell state $|\Phi^+\rangle\langle\Phi^+|$ (Eq. (1.77)), as well as an estimate of the concurrence (Eq. (1.81)).

$f_1^{s,i}$[mm]	$f_2^{s,i}$[mm]	$F^{(CW)}$	$C^{(CW)}$	$F^{(pulse)}$	$C^{(pulse)}$
40	250	0.9972 ± 0.0002	0.9887 ± 0.0007	0.9939 ± 0.0003	0.976 ± 0.001
50	300	0.9961 ± 0.0001	0.9846 ± 0.0005	0.9917 ± 0.0001	0.9668 ± 0.0006
40	300	0.9947 ± 0.0002	0.9790 ± 0.0006	0.9914 ± 0.0003	0.966 ± 0.001
50	250	0.9962 ± 0.0001	0.9848 ± 0.0005	0.9925 ± 0.0002	0.9700 ± 0.0009

Table 5.7: Estimation of the Bell-state fidelity (F) and concurrence (C) of the experimental quantum states. Uncertainties are determined using a Monte Carlo simulation involving 100 iterations.

Using the experimental visibilities, we can also derive lower bounds for the fidelity (Eq. (1.80)) and for the concurrence (Eq. (1.84)) of the emitted states, without making assumptions about their specific expression.

$f_1^{s,i}$[mm]	$f_2^{s,i}$[mm]	$F_{min}^{(CW)}$	$C_{min}^{(CW)}$	$F_{min}^{(pulse)}$	$C_{min}^{(pulse)}$
40	250	0.9932 ± 0.0003	0.9863 ± 0.0005	0.9793 ± 0.0005	0.959 ± 0.001
50	300	0.9907 ± 0.0002	0.9813 ± 0.0004	0.9788 ± 0.0003	0.9576 ± 0.0005
40	300	0.9875 ± 0.0003	0.975 ± 0.0006	0.9758 ± 0.0004	0.9516 ± 0.0008
50	250	0.9909 ± 0.0002	0.9817 ± 0.0004	0.9780 ± 0.0004	0.9560 ± 0.0007

Table 5.8: Estimation of lower bounds for the fidelity and concurrence of the experimental quantum states.

5.4.1 Quantum State Tomography

The effective *p-c* model employed for reconstructing the quantum state of the emitted photons relies exclusively on visibility measurements in the $\mathbb{Z}$ and $\mathbb{X}$ bases. For a comprehensive characterization of the quantum state of the emitted photons, a complete Quantum State Tomography (QST) is useful (see Sec. 1.6). Achieving a full QST for a two-qubit system involves 16 measurements and requires a polarization measurement setup that incorporates both QWPs and HWPs (refer to Appendix B for further details). This procedure presents greater challenges compared to estimating the sole visibilities due to uncertainties related to QWP positioning, potential experimental setup instability during extended measurements, and uncertainties linked to the maximum likelihood method. Nonetheless, it is interesting to reconstruct the state using this method and then compare it with the theoretical effective model. The state of the emitted photons can be represented in the density matrix formalism as:

$$\hat{\rho} = \begin{pmatrix} \rho_{11} & \rho_{12} & \rho_{13} & \rho_{14} \\ \rho_{21} & \rho_{22} & \rho_{23} & \rho_{24} \\ \rho_{31} & \rho_{32} & \rho_{33} & \rho_{34} \\ \rho_{41} & \rho_{42} & \rho_{43} & \rho_{44} \end{pmatrix} \tag{5.1}$$

We performed a QST on the states emitted by the source in the initial source configuration in the CW regime. The coefficients of the density matrix reconstructed through the QST are presented in Tab. 5.9, while a visual representation is depicted in Fig. 5.7. Uncertainties are determined using a Monte Carlo simulation involving 100 iterations (Sec. 1.6.1).

Matrix element	Estimated value
ρ_{11}	0.491 ± 0.006
ρ_{22}	0.007 ± 0.002
ρ_{33}	0.009 ± 0.002
ρ_{44}	0.493 ± 0.006
$\rho_{21} = \rho_{12}^*$	$(-0.01 \pm 0.01) - i(0.03 \pm 0.03)$
$\rho_{31} = \rho_{13}^*$	$(0.006 \pm 0.01) + i(0.061 \pm 0.008)$
$\rho_{32} = \rho_{23}^*$	$(-0.003 \pm 0.003) - i(0.001 \pm 0.002)$
$\rho_{41} = \rho_{14}^*$	$(0.459 \pm 0.007) + i(0.02 \pm 0.02)$
$\rho_{42} = \rho_{24}^*$	$(-0.012 \pm 0.009) + i(0.03 \pm 0.03)$
$\rho_{43} = \rho_{34}^*$	$(0.01 \pm 0.01) - i(0.07 \pm 0.08)$

Table 5.9: Coefficients of the density matrix reconstructed through the quantum state tomography. Note that the ideal state $|\phi^+\rangle\langle\phi^+|$ has $\rho_{11} = \rho_{44} = \rho_{14} = \rho_{41} = 0.5$.

The fidelity between the state reconstructed through QST, $\hat{\rho}_{QST}$, and the ideal state $|\phi^+\rangle\langle\phi^+|$ is:

$$F(\hat{\rho}_{QST}, |\phi^+\rangle\langle\phi^+|) = 0.975 \pm 0.004 \tag{5.2}$$

Notably, we observe that the coefficients ρ_{14} and ρ_{41}, corresponding to the components $|HH\rangle\langle VV|$ and $|VV\rangle\langle HH|$ of the density matrix, are lower than their diagonal counterparts ρ_{11} and ρ_{44}. This discrepancy can be interpreted as a manifestation of decoherence in the quantum states, possibly arising from a distinguishability introduced between the clockwise and counterclockwise components of the Sagnac loop due to a non-optimal alignment of the setup. This term is also considered in the effective model (where it is regulated by the coefficient *c*). Comparing the effective model with the QST outcomes provides valuable insights.

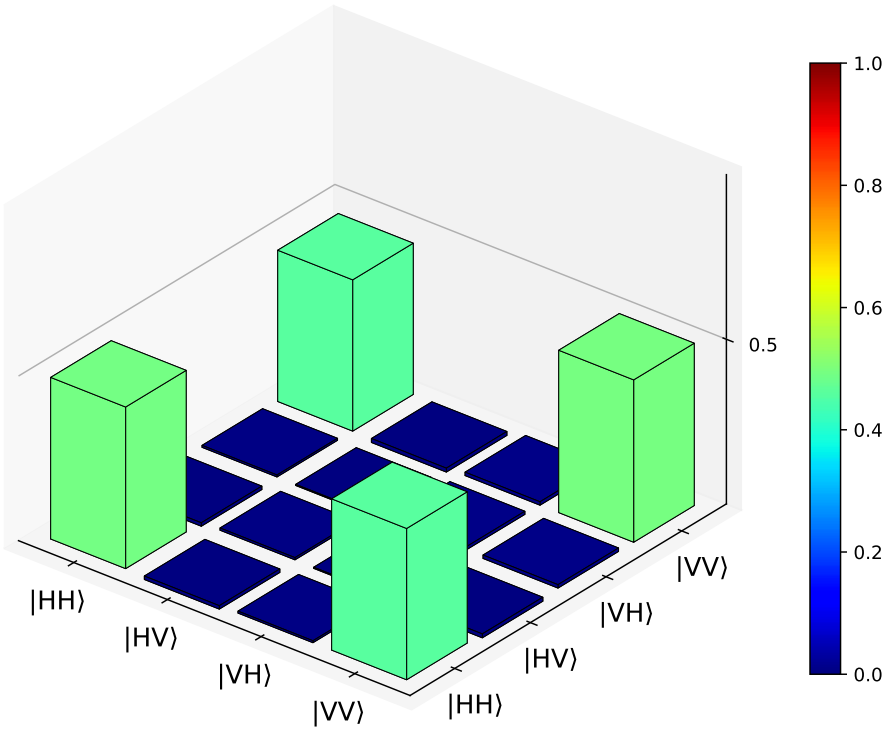

Figure 5.7: Graphical representation of the real part of the density matrix of the emitted states as estimated by quantum state tomography.

The visibilities measured before conducting this test are as follows[1]:

$$V_{\mathbb{Z}} = (99.29 \pm 0.02)\% \qquad V_{\mathbb{X}} = (98.74 \pm 0.03)\% \tag{5.3}$$

Using these visibilities, it is possible to estimate the state $\hat{\rho}_{pc}$ with the *p-c* model:

$$p = 0.0071 \pm 0.0002 \qquad c = 0.0055 \pm 0.0004 \qquad F(\hat{\rho}_{pc}, |\phi^+\rangle\langle\phi^+|) = 0.9959 \pm 0.0001 \tag{5.4}$$

The fidelity between the state obtained from QST and the one reconstructed from the visibilities $V_{\mathbb{Z}}$ and $V_{\mathbb{X}}$ is approximately $F(\hat{\rho}_{QST}, \hat{\rho}_{pc}) \approx 0.986$, indicating a strong agreement between full tomography and the effective model. Nonetheless, the effective model is generally more practical, as it offers two advantages: it involves only 8 measurements and ensures a higher precision by exclusively employing HWPs.

5.5 Bell Test

Another testing approach employed to assess the quality of the generated entangled states is the Bell test (Sec. 1.4.1). This type of test holds fundamental significance in physics, as it provides the experimental verification of the nonlocality of quantum mechanics. The experimental setup employed to conduct the Bell test closely resembles the one proposed by A. Aspect in 1982 [65]. From an experimental perspective, this test necessitates 16 measurements, which are employed to estimate the value of S in the CHSH inequality, where $S \leq 2$ for any non-entangled state (in these measurements the accidental events have not been subtracted). The maximum violation of this inequality $S = 2\sqrt{2} \approx 2.828$, is achieved for maximally entangled Bell states (such as the state $|\Phi^+\rangle$). These measurements are carried out using only HWPs in the polarization measurement setup (a more detailed explanation of this method is available in Appendix A).

[1] These results are different from those reported in Tab. 5.5 because this test was conducted on another day.

We can also estimate the value of S using the effective model through the measurement of visibilities (Eq. (1.100)). The results depicting the experimental and theoretical values of S are presented in Tab. 5.10, for both CW and pulse regimes.

$f_1^{s,i}$[mm]	$f_2^{s,i}$[mm]	$S_{exp}^{(CW)}$	$S_{exp}^{(pulse)}$	$S_{th}^{(CW)}$	$S_{th}^{(pulse)}$
40	250	2.803 ± 0.003	2.765 ± 0.005	2.8090 ± 0.0007	2.770 ± 0.001
50	300	2.815 ± 0.003	2.780 ± 0.004	2.8019 ± 0.0006	2.7684 ± 0.0007
40	300	2.801 ± 0.004	2.750 ± 0.004	2.7931 ± 0.0008	2.760 ± 0.001
50	250	2.802 ± 0.003	2.760 ± 0.003	2.8026 ± 0.0006	2.766 ± 0.001

Table 5.10: Comparison between the experimentally estimated CHSH inequality and the corresponding value predicted by the effective model of the emitted states for each source configuration. The uncertainties were evaluated by the propagation of the Poisson error on the coincidence photon counts.

The achieved results are remarkable, particularly in the continuous wave (CW) regime, where nearly maximal violations of the Bell inequality have been observed. These violations provide an extremely high confidence level (over 300 σ) in the validity of quantum mechanics predictions. These results are significant, not only from a fundamental perspective but also in terms of practical applications. The Bell test is used to ensure the security of specific protocols of quantum key distribution and quantum random generators.

It is noteworthy that in pulsed mode, the values of S are lower than those in the CW mode. This reduction can be attributed, as observed in the case of visibilities, to a higher occurrence of accidental coincidences. Additionally, the estimated values of S from the effective model of the emitted states closely align with the experimental results. This result provides further substantiation for the model's validity in accurately describing these states.

5.6 Measuring Accidental Coincidences

The influence of accidental coincidences, as demonstrated in the previous sections, significantly affects the quality of the emitted entangled photons by introducing spurious signals that do not correspond to actual entangled photon events. Our analysis of visibilities (Sec. 5.3) and Bell tests (Sec. 5.5) has revealed that this phenomenon manifests differently depending on whether we are considering the CW regime or the pulse regime. We have seen in Sec. 3.4 (for more details, also refer to the Appendix D) that there are two distinct formulas for calculating the counting rates of accidental coincidences, depending on the operational mode of the laser. While subtracting these coincidences from the raw data is not feasible for some practical applications of the source, it remains crucial to assess the performance in the pulse mode (which will be the primary mode of operation for this source). This enables us to ascertain whether the reduction in visibility is solely attributable to accidental coincidences and to verify the accuracy of our estimation of these coincidence rates. To achieve this, we conducted measurements of visibility in the $\mathbb{Z}$ and $\mathbb{X}$ bases, both in CW and pulse modes, while varying the pump beam power. Furthermore, we utilized the theoretical formulas (Eqs. (4.2) and (4.3)) to evaluate the impact of accidental coincidences and subsequently subtracted them. A comparison between raw and accidental-subtracted visibilities is depicted in Figs. 5.8, 5.9, 5.10, and 5.11.

The impact of accidental coincidences in the CW mode is small compared to the pulse case. The disparity in visibility between raw and accidental-subtracted data is approximately 0.05%. As a result in CW mode, we have achieved high performance in terms of visibilities and Bell inequality violations. This achievement can be attributed to the utilization of an extremely narrow coincidence window Δt_c, effectively filtering out the majority of accidental events. Nevertheless, in the pulse mode, the results are different. The subtraction of accidental coincidences proves effective for the $\mathbb{Z}$-basis, yielding consistent and relatively constant values. However, this approach fails to fully elucidate the decline in visibility in the $\mathbb{X}$-basis (Fig. 5.11). This disparity might come from a reduction in the indistinguishability between the emitted photons. Importantly, this effect leaves the visibility in the $\mathbb{Z}$-basis unaffected while exclusively impacting the $\mathbb{X}$-basis, leading to a reduction in its visibility. This effect

must be taken into account in source applications: increasing the pump beam power leads to higher brightness but a decrease in visibility.

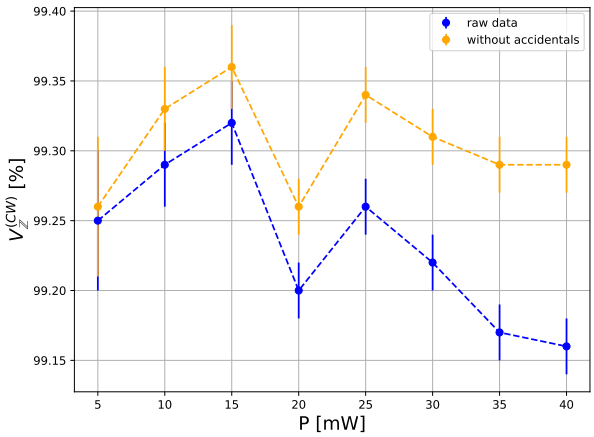

Figure 5.8: Visibility $V_{\mathbb{Z}}^{(CW)}$ as a function of pump power in CW mode: raw data (blue), accidental-subtracted (orange).

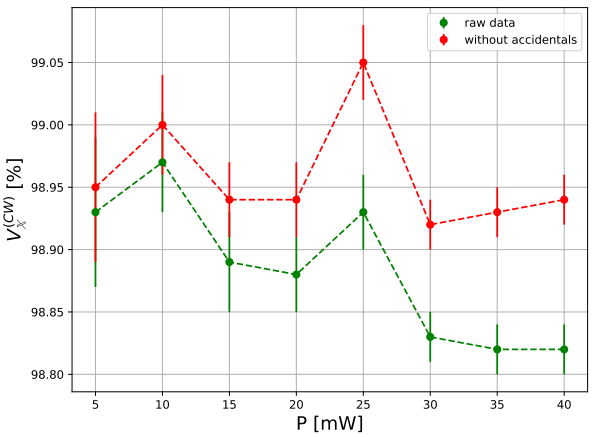

Figure 5.9: Visibility $V_{\mathbb{X}}^{(CW)}$ as a function of pump power in CW mode: raw data (green), accidental-subtracted (red).

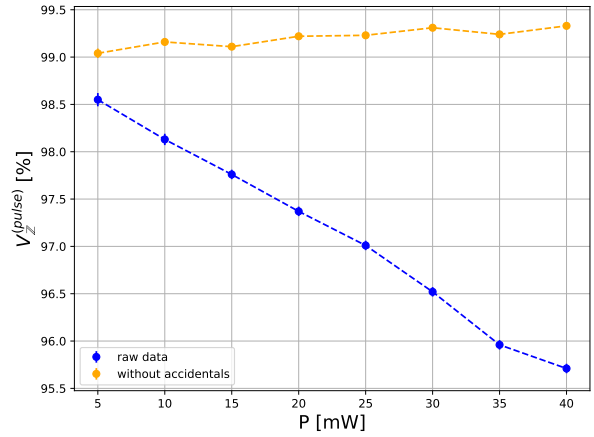

Figure 5.10: Visibility $V_{\mathbb{Z}}^{(pulse)}$ as a function of pump power in pulse mode: raw data (blue), accidental-subtracted (orange).

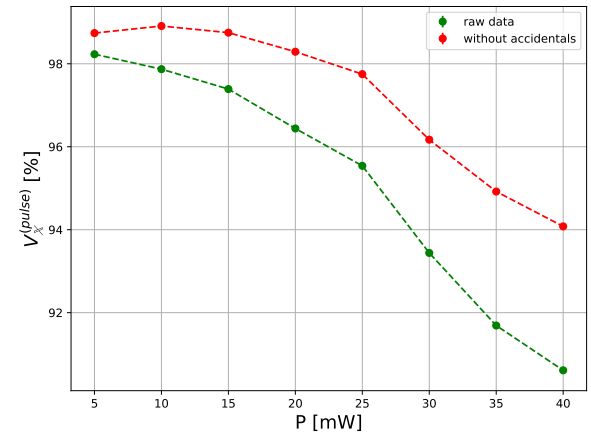

Figure 5.11: Visibility $V_{\mathbb{X}}^{(pulse)}$ as a function of pump power in pulse mode: raw data (green), accidental-subtracted (red).

Conclusion and Future Perspectives

In this thesis, I have discussed the design and implementation of a polarization-entangled photon source operating at 1550 nm based on a type-II SPDC within a PPKTP crystal. I started by presenting an effective model for the description of the SPDC process in the crystal, enabling us to understand how brightness and heralding ratios change in response to alterations in pump, signal, and idler beam focusing conditions. Based on this theoretical model, I devised and constructed an optical configuration for the source in order to achieve the optimal conditions outlined by the model. Furthermore, I conducted additional tests, varying the optical configuration of the source, to verify the predictivity of the model.

The experimental results reveal some discrepancies compared to the theoretical predictions, which can be attributed to various factors. From an experimental perspective, achieving the optimal alignment is a complex procedure, entailing the fulfillment of multiple requisites, which proves challenging to optimize. This involves the simultaneous optimization of several parameters, which include precise pump beam focusing at the crystal's center, alignment of the Sagnac loop, and accurate positioning of mirrors for effective fiber coupling. Moreover, the stability of the source can be susceptible to fluctuations in temperature, as well as variations in the intensity or wavelength of the pump beam due to laser instability. This intricate relation between different parameters frequently complicates the search for the optimal condition that maximizes source performance. Enhancing certain parameters might unavoidably lead to the worsening of others. This highlights the crucial role of the operator's experience in achieving precise alignment. As my experience grew, I gradually attained more refined alignments, which ultimately led to improved results. Additionally, it's crucial to acknowledge that the theoretical model relies on certain approximations, such as the thin crystal limit. Moreover, this treatment assumes ideal Gaussian beams and a Gaussian pump spectral distribution. The extent to which these approximations impact the model's predictions remains unclear. One solution is to develop a more accurate model that accounts for these non-ideal effects.

The practical challenges encountered in optimizing the source are a well-known aspect in the literature and constitute one of the reasons why obtaining accurate and repeatable experimental results is a difficult task. For this reason, in this thesis, I have provided a detailed description of the procedure employed for the alignment of the source. However, to ensure a more robust evaluation of the model's accuracy, analyzing more source configurations can help. It will be important to expand the study of the model to additional source configurations, changing both the set of lenses used for collecting downconverted photons and focusing the pump photons into the crystal.

There are several critical aspects that determine the performance of this source. One of these is the two-lens system employed to focus the pump photons into the crystal and collect the entangled photons. This system enables precise selection of the Gaussian modes of the pump, signal, and idler beams, which, as demonstrated, significantly influence the brightness and heralding ratio. This approach offers enhanced precision and practical control compared to setups reliant on a single lens. Additionally, the experimental setup is compact and robust due to the rigid mounts which sustain the optical components. These mounts not only enhance the positional accuracy of the optical components but also simplify alignment and lens replacement procedures. Another important aspect is the utilization of an XYZ translation stage, which proved valuable for fine-positioning the crystal. These distinctive features set this source apart from many others presented in the literature, including the one already existing in the laboratory, resulting in achieving high performance. In the optimal configuration, a brightness of approximately 4600 pairs/s/mW and heralding ratios of around 25%

are attained. The most noteworthy feature, however, is the quality of the emitted entangled photons. Particularly, in the CW regime, the achieved visibilities are remarkable, with $V_{\mathbb{Z}}^{(CW)} \approx 99.5\%$ and $V_{\mathbb{X}}^{(CW)} \approx 99.1\%$. This aspect is further validated through Bell tests, showcasing the feasibility of generating almost maximally entangled states. The highest violation recorded was 2.815. In pulse mode, we observed a slight reduction in the quality of entangled states due to increased multiple pair emissions which increase the accidental events. We have, thus, examined how the visibilities in the $\mathbb{Z}$ and $\mathbb{X}$ bases vary with the power of the pump beam. Specifically, at a pump power of 10 mW, we achieved visibilities of $V_{\mathbb{Z}}^{(pulse)} \approx 98.5\%$ and $V_{\mathbb{X}}^{(pulse)} \approx 97.4\%$. Lastly, among the accomplished results, it's notable to emphasize the effectiveness of a model that accurately characterizes the states emitted by the source. This model particularly emphasizes the contributing factors that reduce the quality of entangled photons, including decoherence and depolarization, providing insights into factors that affect the source's performance.

One of the future goals will be to further increase the source's performance, especially in terms of brightness and heralding ratio. On one hand, this goal can be achieved by replacing certain components, such as optics and lossy fibers, with others that offer better performance. On the other hand, the improvement of the theoretical model could highlight configurations with higher performance. The model and the built source will serve as useful tools for several future research activities, like quantum teleportation, device-independent QKD, and device-independent QRNG.

Appendix A

CHSH Experimental Measurement

In Sec. 1.4, we have discussed the experimentally accessible quantity S through which it is possible to distinguish correlations achievable through local hidden variable theories ($S \leq 2$) from those predicted by quantum mechanics ($S \leq 2\sqrt{2}$). S is defined as:

$$S = \langle \hat{S} \rangle = \langle \hat{A}_0 \otimes \hat{B}_0 \rangle + \langle \hat{A}_1 \otimes \hat{B}_0 \rangle + \langle \hat{A}_0 \otimes \hat{B}_1 \rangle - \langle \hat{A}_1 \otimes \hat{B}_1 \rangle \tag{A.1}$$

We have seen that the maximum violation of the CHSH inequality ($S = 2\sqrt{2}$) can be achieved, in the framework of quantum mechanics, only for specific choices of the local operators acting on each subsystem. For example, in the case of $|\Phi^+\rangle$, we have demonstrated that a possible choice of these local operators (represented in their matrix form) is as follows:

$$\hat{A}_0 = \hat{\sigma}_z = \begin{pmatrix} 1 & 0 \\ 0 & -1 \end{pmatrix} \qquad \hat{A}_1 = \hat{\sigma}_x = \begin{pmatrix} 0 & 1 \\ 1 & 0 \end{pmatrix} \tag{A.2}$$

$$\hat{B}_0 = \frac{\hat{\sigma}_z + \hat{\sigma}_x}{\sqrt{2}} = \frac{1}{\sqrt{2}} \begin{pmatrix} 1 & 1 \\ 1 & -1 \end{pmatrix} \qquad \hat{B}_1 = \frac{\hat{\sigma}_z - \hat{\sigma}_x}{\sqrt{2}} = \frac{1}{\sqrt{2}} \begin{pmatrix} 1 & -1 \\ -1 & -1 \end{pmatrix} \tag{A.3}$$

Our goal is to determine their spectral decomposition (see Eq. (1.28)) and subsequently identify a set of projective measurements that allow us to implement these kinds of operations. Then, we will explain how to relate the experimental results with the value of S.

Each operator has two eigenvalues, namely ± 1, corresponding to orthogonal eigenvectors. By convention (the same one adopted in Sec. 1.4.1), we denote the polarization state of a photon after a projective measurement corresponding to the eigenvalue +1 as θ, and the state corresponding to the eigenvalue -1 as $\theta^\perp$. The eigenvectors of $\hat{A}_0$ are $\{|H\rangle, |V\rangle\}$, which correspond to the angles $\theta_1 = 0°$ and $\theta_1^\perp = 90°$, respectively. The eigenvectors of $\hat{A}_1$, are $\{|D\rangle, |A\rangle\}$, corresponding to the angles $\theta_1' = 45°$ and $\theta_1'^\perp = 135°$. Similarly, the eigenvectors of $\hat{B}_0$ and $\hat{B}_1$ are:

$$\vec{b}_0^{(+)} = \begin{pmatrix} \frac{1+\sqrt{2}}{\sqrt{1+(1+\sqrt{2})^2}} \\ \frac{1}{\sqrt{1+(1+\sqrt{2})^2}} \end{pmatrix} \qquad \vec{b}_0^{(-)} = \begin{pmatrix} \frac{1-\sqrt{2}}{\sqrt{1+(-1+\sqrt{2})^2}} \\ \frac{1}{\sqrt{1+(-1+\sqrt{2})^2}} \end{pmatrix} \tag{A.4}$$

$$\vec{b}_1^{(+)} = \begin{pmatrix} \frac{-1-\sqrt{2}}{\sqrt{1+(1+\sqrt{2})^2}} \\ \frac{1}{\sqrt{1+(1+\sqrt{2})^2}} \end{pmatrix} \qquad \vec{b}_1^{(-)} = \begin{pmatrix} \frac{-1+\sqrt{2}}{\sqrt{1+(-1+\sqrt{2})^2}} \\ \frac{1}{\sqrt{1+(-1+\sqrt{2})^2}} \end{pmatrix} \tag{A.5}$$

These eigenvectors correspond to polarization measurements at the angles $\{\theta_2, \theta_2^\perp\} = \{22.5°, 112.5°\}$ for $\hat{B}_0$ and $\{\theta_2', \theta_2'^\perp\} = \{157.5°, 67.5°\}$ for $\hat{B}_1$. The measurements performed by Bob are equivalent to those performed by Alice, but with an additional rotation of 22.5°.

The experimentally accessible quantities are the expectation values of the combined polarization measurements on the bipartite system, which can be written as:

$$\langle \hat{A}_x \otimes \hat{B}_y \rangle = \sum_{a,b \in \{\pm 1\}} ab\, p(ab|xy) \tag{A.6}$$

where $a, b \in \{\pm 1\}$ denote the eigenvalue of each local operator. The probabilities, for each combination of the local operators (x, y), must satisfy the normalization condition:

$$\sum_{a,b\in\{\pm1\}} p(ab|xy) = 1 \qquad \text{with} \quad x, y \in \{0, 1\} \tag{A.7}$$

What is experimentally measured, for each choice of the projective measurement denoted as $(\theta_x^{(a)}, \theta_y^{(b)})$, is the number of coincidence events recorded by Alice and Bob, referred to as $N_c(\theta_x^{(a)}, \theta_y^{(b)})$ which is proportional to the probability $p(ab|xy)$. From these experimental values, we can calculate the corresponding probabilities (which must satisfy the normalization condition in Eq. (A.7)) as follows:

$$p(a, b|x, y) = \frac{N_c(\theta_x^{(a)}, \theta_y^{(b)})}{N_{TOT}} \qquad \text{with} \quad N_{TOT} = \sum_{a,b\in\{\pm1\}} N_c(\theta_x^{(a)}, \theta_y^{(b)}) \tag{A.8}$$

Following this approach, we are able to estimate all the expectation values in Eq. (A.6):

$$\begin{aligned}\langle \hat{A}_0 \hat{B}_0 \rangle = E(\theta_1, \theta_2) = p(+1,+1|0,0) + p(-1,-1|0,0) - p(+1,-1|0,0) - p(-1,+1|0,0) = \\ = \frac{N_c(\theta_1, \theta_2) + N_c(\theta_1^\perp, \theta_2^\perp) - N_c(\theta_1^\perp, \theta_2) - N_c(\theta_1, \theta_2^\perp)}{N_c(\theta_1, \theta_2) + N_c(\theta_1^\perp, \theta_2^\perp) + N_c(\theta_1^\perp, \theta_2) + N_c(\theta_1, \theta_2^\perp)}\end{aligned} \tag{A.9}$$

$$\begin{aligned}\langle \hat{A}_1 \hat{B}_0 \rangle = E(\theta_1', \theta_2) = p(+1,+1|1,0) + p(-1,-1|1,0) - p(+1,-1|1,0) - p(-1,+1|1,0) = \\ = \frac{N_c(\theta_1', \theta_2) + N_c(\theta_1'^\perp, \theta_2^\perp) - N_c(\theta_1'^\perp, \theta_2) - N_c(\theta_1', \theta_2^\perp)}{N_c(\theta_1', \theta_2) + N_c(\theta_1'^\perp, \theta_2^\perp) + N_c(\theta_1'^\perp, \theta_2) + N_c(\theta_1', \theta_2^\perp)}\end{aligned} \tag{A.10}$$

$$\begin{aligned}\langle \hat{A}_0 \hat{B}_1 \rangle = E(\theta_1, \theta_2') = p(+1,+1|0,1) + p(-1,-1|0,1) - p(+1,-1|0,1) - p(-1,+1|0,1) = \\ = \frac{N_c(\theta_1, \theta_2') + N_c(\theta_1^\perp, \theta_2'^\perp) - N_c(\theta_1^\perp, \theta_2') - N_c(\theta_1, \theta_2'^\perp)}{N_c(\theta_1, \theta_2') + N_c(\theta_1^\perp, \theta_2'^\perp) + N_c(\theta_1^\perp, \theta_2') + N_c(\theta_1, \theta_2'^\perp)}\end{aligned} \tag{A.11}$$

$$\begin{aligned}\langle \hat{A}_1 \hat{B}_1 \rangle = E(\theta_1', \theta_2') = p(+1,+1|1,1) + p(-1,-1|1,1) - p(+1,-1|1,1) - p(-1,+1|1,1) = \\ = \frac{N_c(\theta_1', \theta_2') + N_c(\theta_1'^\perp, \theta_2'^\perp) - N_c(\theta_1'^\perp, \theta_2') - N_c(\theta_1', \theta_2'^\perp)}{N_c(\theta_1', \theta_2') + N_c(\theta_1'^\perp, \theta_2'^\perp) + N_c(\theta_1'^\perp, \theta_2') + N_c(\theta_1', \theta_2'^\perp)}\end{aligned} \tag{A.12}$$

Polarization measurements on each subsystem are conducted through a combination of an HWP and a PBS. The specific angles for Alice and Bob's HWPs are listed in Tab. A.1.

Alice	Bob	θ_A	θ_B
$\|\theta_1\rangle$	$\|\theta_2\rangle$	0°	11.25°
$\|\theta_1\rangle$	$\|\theta_2^\perp\rangle$	0°	56.25°
$\|\theta_1\rangle$	$\|\theta_2'\rangle$	0°	78.75°
$\|\theta_1\rangle$	$\|\theta_2'^\perp\rangle$	0°	33.75°
$\|\theta_1^\perp\rangle$	$\|\theta_2\rangle$	45°	11.25°
$\|\theta_1^\perp\rangle$	$\|\theta_2^\perp\rangle$	45°	56.25°
$\|\theta_1^\perp\rangle$	$\|\theta_2'\rangle$	45°	78.75°
$\|\theta_1^\perp\rangle$	$\|\theta_2'^\perp\rangle$	45°	33.75°
$\|\theta_1'\rangle$	$\|\theta_2\rangle$	22.5°	11.25°
$\|\theta_1'\rangle$	$\|\theta_2^\perp\rangle$	22.5°	56.25°
$\|\theta_1'\rangle$	$\|\theta_2'\rangle$	22.5°	78.75°
$\|\theta_1'\rangle$	$\|\theta_2'^\perp\rangle$	22.5°	33.75°
$\|\theta_1'^\perp\rangle$	$\|\theta_2\rangle$	67.5°	11.25°
$\|\theta_1'^\perp\rangle$	$\|\theta_2^\perp\rangle$	67.5°	56.25°
$\|\theta_1'^\perp\rangle$	$\|\theta_2'\rangle$	67.5°	78.75°
$\|\theta_1'^\perp\rangle$	$\|\theta_2'^\perp\rangle$	67.5°	33.75°

Table A.1: Set of the HWP angles used in Bell test.

Appendix B

Quantum Tomography Measurements

Quantum state tomography enables a complete reconstruction of a quantum state through a set of measurements. For two-qubit systems, the density matrix requires 16 parameters to be fully characterized. Here, we provide a set of 16 linearly independent projectors in the space of 4×4 complex matrix space. These projectors correspond to experimental measurements that can be conducted on the biphoton quantum state.

$$\hat{\Pi}_{HH} = \begin{pmatrix} 1 & 0 & 0 & 0 \\ 0 & 0 & 0 & 0 \\ 0 & 0 & 0 & 0 \\ 0 & 0 & 0 & 0 \end{pmatrix} \qquad \hat{\Pi}_{HV} = \begin{pmatrix} 0 & 0 & 0 & 0 \\ 0 & 1 & 0 & 0 \\ 0 & 0 & 0 & 0 \\ 0 & 0 & 0 & 0 \end{pmatrix}$$

$$\hat{\Pi}_{VV} = \begin{pmatrix} 0 & 0 & 0 & 0 \\ 0 & 0 & 0 & 0 \\ 0 & 0 & 0 & 0 \\ 0 & 0 & 0 & 1 \end{pmatrix} \qquad \hat{\Pi}_{VH} = \begin{pmatrix} 0 & 0 & 0 & 0 \\ 0 & 0 & 0 & 0 \\ 0 & 0 & 1 & 0 \\ 0 & 0 & 0 & 0 \end{pmatrix}$$

$$\hat{\Pi}_{RH} = \frac{1}{2}\begin{pmatrix} 1 & 0 & -i & 0 \\ 0 & 0 & 0 & 0 \\ i & 0 & 1 & 0 \\ 0 & 0 & 0 & 0 \end{pmatrix} \qquad \hat{\Pi}_{RV} = \frac{1}{2}\begin{pmatrix} 0 & 0 & 0 & 0 \\ 0 & 1 & 0 & -i \\ 0 & 0 & 0 & 0 \\ 0 & i & 0 & 1 \end{pmatrix}$$

$$\hat{\Pi}_{DV} = \frac{1}{2}\begin{pmatrix} 0 & 0 & 0 & 0 \\ 0 & 1 & 0 & 1 \\ 0 & 0 & 0 & 0 \\ 0 & 1 & 0 & 1 \end{pmatrix} \qquad \hat{\Pi}_{DH} = \frac{1}{2}\begin{pmatrix} 1 & 0 & 1 & 0 \\ 0 & 0 & 0 & 0 \\ 1 & 0 & 1 & 0 \\ 0 & 0 & 0 & 0 \end{pmatrix}$$

$$\hat{\Pi}_{DL} = \frac{1}{4}\begin{pmatrix} 1 & i & 1 & i \\ -i & 1 & -i & 1 \\ 1 & i & 1 & i \\ -i & 1 & -i & 1 \end{pmatrix} \qquad \hat{\Pi}_{DD} = \frac{1}{4}\begin{pmatrix} 1 & 1 & 1 & 1 \\ 1 & 1 & 1 & 1 \\ 1 & 1 & 1 & 1 \\ 1 & 1 & 1 & 1 \end{pmatrix}$$

$$\hat{\Pi}_{RD} = \frac{1}{4}\begin{pmatrix} 1 & 1 & -i & -i \\ 1 & 1 & -i & -i \\ i & i & 1 & 1 \\ i & i & 1 & 1 \end{pmatrix} \qquad \hat{\Pi}_{HD} = \frac{1}{2}\begin{pmatrix} 1 & 1 & 0 & 0 \\ 1 & 1 & 0 & 0 \\ 0 & 0 & 0 & 0 \\ 0 & 0 & 0 & 0 \end{pmatrix}$$

$$\hat{\Pi}_{VD} = \frac{1}{2}\begin{pmatrix} 0 & 0 & 0 & 0 \\ 0 & 0 & 0 & 0 \\ 0 & 0 & 1 & 1 \\ 0 & 0 & 1 & 1 \end{pmatrix} \qquad \hat{\Pi}_{VR} = \frac{1}{2}\begin{pmatrix} 0 & 0 & 0 & 0 \\ 0 & 0 & 0 & 0 \\ 0 & 0 & 1 & -i \\ 0 & 0 & i & 1 \end{pmatrix}$$

$$\hat{\Pi}_{HR} = \frac{1}{2}\begin{pmatrix} 1 & -i & 0 & 0 \\ i & 1 & 0 & 0 \\ 0 & 0 & 0 & 0 \\ 0 & 0 & 0 & 0 \end{pmatrix} \qquad \hat{\Pi}_{RR} = \frac{1}{4}\begin{pmatrix} 1 & -i & -i & -1 \\ i & 1 & 1 & -i \\ i & 1 & 1 & -i \\ -1 & i & i & 1 \end{pmatrix}$$

The measurement system is constructed using a combination of optical elements: a QWP, a HWP, and a PBS. The QWP's fast axis is rotated by an angle ϕ, while the HWP's fast axis is rotated by an angle θ. The specific experimental configurations required for performing the projective measurements mentioned above are summarized in Tab. B.1.

Alice	Bob	θ_A	ϕ_A	θ_B	ϕ_B
$\|H\rangle$	$\|H\rangle$	0°	0°	0°	0°
$\|H\rangle$	$\|V\rangle$	0°	0°	45°	0°
$\|V\rangle$	$\|H\rangle$	45°	0°	0°	0°
$\|R\rangle$	$\|H\rangle$	45°	45°	0°	0°
$\|R\rangle$	$\|V\rangle$	45°	45°	45°	0°
$\|D\rangle$	$\|V\rangle$	22.5°	45°	45°	0°
$\|D\rangle$	$\|H\rangle$	22.5°	45°	0°	0°
$\|D\rangle$	$\|L\rangle$	22.5°	45°	45°	−45°
$\|D\rangle$	$\|D\rangle$	22.5°	45°	22.5°	45°
$\|R\rangle$	$\|D\rangle$	45°	45°	22.5°	45°
$\|H\rangle$	$\|D\rangle$	0°	0°	22.5°	45°
$\|V\rangle$	$\|D\rangle$	45°	0°	22.5°	45°
$\|V\rangle$	$\|R\rangle$	45°	0°	45°	45°
$\|H\rangle$	$\|R\rangle$	0°	0°	45°	45°
$\|R\rangle$	$\|R\rangle$	45°	45°	45°	45°

Table B.1: Set of the waveplates angles used in quantum state tomography.

Appendix C

Efficiency of Single-Photon Detectors

A fundamental parameter for evaluating the performance of a detector is efficiency. Typically, this quantity is assessed by the ratio between the number of recorded photons and the number of incident ones. However, SNSPDs are extremely sensitive instruments, capable of registering a maximum photon rate of approximately 10^7 events per second, corresponding to a maximum incident radiation power of around 10^{-12}W. This makes the calibration of such instruments challenging, as there are no photon sources or other measuring instruments in the laboratory that operate at such low power levels. For this reason, we have adopted a specific approach to calibrate the single-photon detectors.

For this purpose, we employed a fiber beam splitter (BS) with a 90:10 division ratio. This device separates the light from a laser beam (at 1550nm in this case) into two paths. The intensity of the light in the path receiving 10% of the incident light is attenuated by 50dB using passive fiber attenuators. The idea is that we can take the light from the 90% path as a reference value for the incident light power on the SNSPD located in the opposite path. Specifically, the power of the photons incident on the SNSPD is related to the power measured by a standard photodetector (PD): $P_{SNSPD} = k \cdot P_{PD}$. Here, k represents an attenuation factor that allows us to estimate the intensity of the light incident on the SNSPD based on the value measured by the PD. To ensure laser stability, achievable when the laser is set to emit light at a power of several mW, an additional 50dB attenuator is introduced before the BS. An optical schematic of the experimental setup is depicted in Fig. C.1.

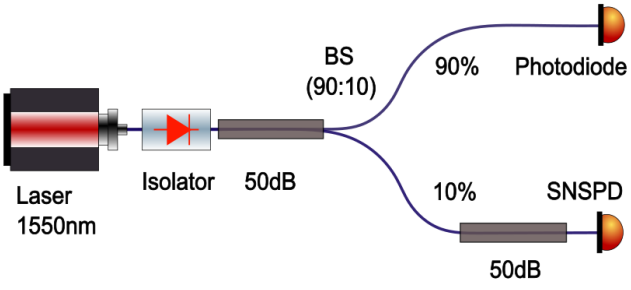

Figure C.1: Experimental setup used for measuring SNSPDs' efficiency.

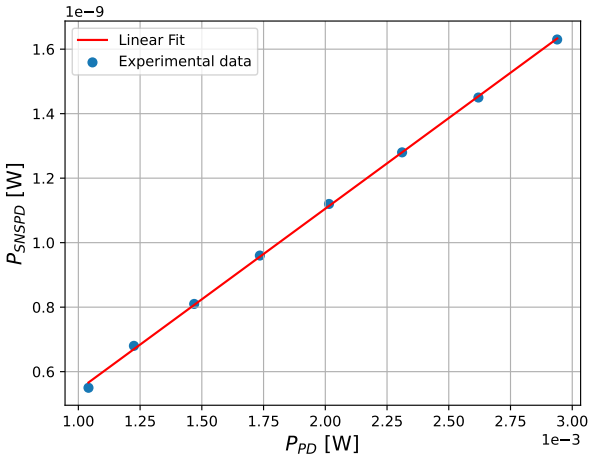

Figure C.2: Plot of the power measured at the ends of the fiber BS to estimate the attenuation factor between the two paths.

The first step in estimating the detector efficiency (ϵ) consists in determining the attenuation factor (k) based solely on the ratio of power at the end of the paths. To achieve this, we temporarily removed the 50dB attenuator positioned before the BS. We measured the power in both branches of the BS, P_{PD} and P_{SNSPD}, using the same photodiode, to eliminate different scale factors arising from the use of different photodetectors. From the slope of the linear fit of P_{SNSPD} as a function of P_{PD} (refer to Fig.

C.2), we determined the attenuation factor as $k = (5.62 \pm 0.05) \times 10^{-7}$. Then, we reinserted the 50dB attenuation before the BS and we proceeded with estimating the efficiency of the detectors.

In the laboratory, there are seven available channels each corresponding to a different detector with a distinct efficiency. However, throughout my thesis work, we consistently used only two channels: Channel 5 and Channel 8. Therefore, in this analysis, we present the results obtained only for these two channels. Initially, we determined the range of powers within which the laser can operate without the risk of exceeding the damage threshold of the SNSPDs. Subsequently, we conducted a series of measurements by varying the emitted light intensity from the laser, recording both the power measured by the photodiode (P_{PD}) and the output counting rate of the detector (N_{out}). We estimated the power incident on the SNSPD through the values measured by the PD as $P_{SNSPD} = k \cdot P_{PD}$. The effective counting rates were then corrected using the formula in Eq. (3.2), which takes into account the detectors saturation at high counting rates. From this correction, we determined the effective rate of measurable photons (N_{meas}) and its corresponding power $P_{meas} = N_{meas} \cdot h\nu$ (where ν denotes the frequency of the photons and h represents the Planck constant).

In this way, we have understood how the power measured by the SNSPD (P_{meas}) varies with the incident power (P_{SNSPD}). Through two linear fits (see Figs. C.3 and C.4), we have estimated the efficiency of each channel:

$$\epsilon_{ch5} = 0.703 \pm 0.001 \qquad \epsilon_{ch8} = 0.779 \pm 0.02$$

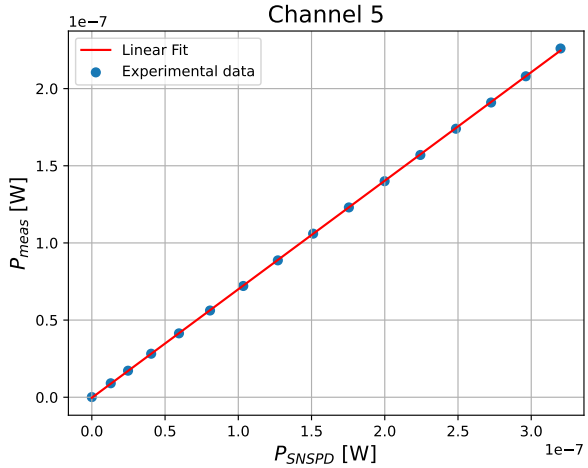

Figure C.3: Linear fit of the power measured in Channel 5 P_{meas} as a function of the estimated incident power P_{SNSPD}.

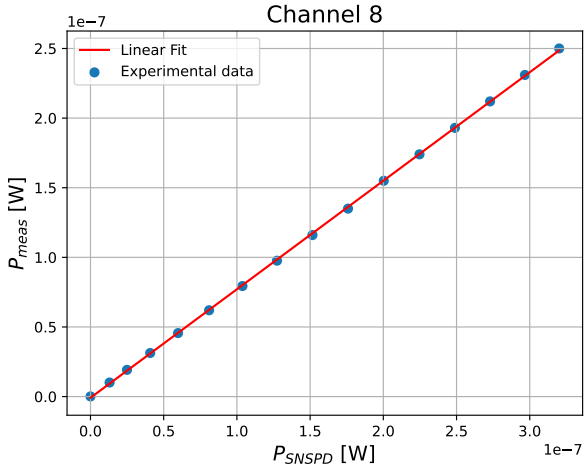

Figure C.4: Linear fit of the power measured in Channel 8 P_{meas} as a function of the estimated incident power P_{SNSPD}.

Appendix D

Accidental Coincidences

When evaluating the performance of an entangled photon source, the quantum states are detected using a coincidence system. This is because photon pairs are emitted simultaneously within the crystal. In this context, it becomes crucial to consider the impact of accidental coincidences. These coincidences, indeed, do not represent actual signals and they degrade the quality of the results. The ability to accurately quantify the occurrence of such coincidences holds fundamental significance in characterizing the overall performance of the source. In this chapter, we will provide a straightforward demonstration of the expected accidental counting rates for both CW and pulse modes.

Accidental Coincidences in CW Mode

To derive the formula for the expected rate of accidental coincidences in the CW regime, denoted as $R_{\text{acc}}^{(\text{CW})}$, which occur within a coincidence time interval Δt_c, we start by assuming that the average signal rates for channel A and channel B are respectively R_A and R_B. The approach is based on subdividing the acquisition time interval Δt into smaller time intervals. In each of these intervals, we expect an average number of events μ. The probability of observing n events follows from the Poisson statistics and is given by:

$$\mathcal{P}(\mu; n) = \frac{\mu^n e^{-\mu}}{n!} \tag{D.1}$$

Let us consider an infinitesimal time interval $[t, t + dt]$. The probability of detecting an event in channel A within this time interval is described by the Poisson probability distribution: $p_A(t, dt) = \mathcal{P}(\mu = R_A dt; 1) = R_A dt e^{-R_A dt} \approx R_A dt$. In the last step, we neglect the exponential term $e^{-R_A dt}$ which, as dt approaches zero in the infinitesimal limit, tends to 1. In this limit, we can treat the process through the Bernoulli statistics since we are neglecting the possibility that two or more events happen within the same infinitesimal time interval.

Let's now introduce the coincidence time window Δt_c. Two events that are recorded in channel A (at time t) and channel B (at time t_B) are considered coincident if their time difference is $|\Delta t| = |t - t_B| \leq \Delta t_c$. Our objective is to assess the probability of detecting at least one event in channel B within the time interval $[t - \Delta t_c, t + \Delta t_c]$. This can be formulated using the Poisson probability distribution as follows:

$$p_B(t, dt) = \mathcal{P}(2R_B \Delta t_c; n > 0) = 1 - \mathcal{P}(2R_B \Delta t_c; n = 0) = 1 - e^{-2R_B \Delta t_c} \approx 2R_B \Delta t_c \tag{D.2}$$

The last approximation holds when $R_B \Delta t_c \ll 1$, and it's applicable in our case since $\Delta t_c = 0.25$ ns, while the signal rates in both channels are approximately 10^5 Hz. Notably, if $R_B \Delta t_c \ll 1$ we can treat the detection of an event in channel B as a Bernoulli process with probability $p_B(t, dt)$.

The probability of an accidental coincidence occurring within the infinitesimal time interval $[t, t + dt]$ for channel A, considering a coincidence window Δt_c, can be expressed as:

$$p_{\text{coinc}}(t, dt) = p_A(t, dt) p_B(t, dt) = 2R_A R_B \Delta t_c dt \tag{D.3}$$

This quantity corresponds to the probability of the combined Bernoulli process. As a consequence, the coincidence probability in the time interval $[t, t+dt]$ is equal to the expected number of accidental coincidences $dN_{\text{coinc}}(t)$ recorded in that interval.

The expected accidental coincidences occurring within an arbitrary time interval Δt are computed by integrating the infinitesimal number of coincidences $dN_{\text{coinc}}(t)$ over t: $N_{\text{coinc}}(\Delta t) = 2R_A R_B \Delta t_c \Delta t$. Eventually, the expected rate of accidental coincidences can be deduced by dividing the total number of accidental coincidences for the time interval Δt. Consequently, the final expression for the accidental coincidence rate in the CW mode is:

$$R_{\text{acc}}^{(CW)} = 2R_A R_B \Delta t_c \tag{D.4}$$

Accidental Coincidences in Pulse Mode

Let us now explore a scenario where both channels emit signals in the form of pulses, each with a duration of τ_p, and these pulses are separated by a temporal interval Δt_p. The pulse rate, commonly referred to as the repetition rate, is represented by $r = 1/\Delta t_p$. We will concentrate on the specific situation where $\tau_p \ll \Delta t_c \ll \Delta t_p$, an assumption based on the experimental parameters: $\tau_p \approx 2$ ps, $\Delta t_c = 0.25$ ns, and $\Delta t_p \approx 13.2$ ns.

In this situation, the application of the coincidence window is not eliminating signals within a pulse (because $\tau_p \ll \Delta t_c$) nor considering signals coming from different pulses (because $\Delta t_c \ll \Delta t_p$). Furthermore, we make the assumption that, owing to the extended dead time of the single-photon detectors (100 ns, which greatly exceeds τ_p), each pulse can yield at most one detection per channel. We observe that for each pulse, each channel has a specific probability of either not receiving or receiving only one signal. This statistical behavior can be described as a Bernoulli process. The probability of having a detection in a single pulse in channel A is given by $p_A = \frac{R_A}{r}$, and similarly, in channel B, it is given by $p_B = \frac{R_B}{r}$. Importantly, this same statistical process is applicable to the coincidences observed between events recorded in the two channels (combination of two Bernoulli processes). In this scenario, the probability of a coincidence occurring within a pulse can be expressed as follows:

$$p_{\text{coinc}}^{(pulse)} = p_A p_B = \frac{R_A R_B}{r^2} \tag{D.5}$$

If we consider an arbitrary time interval Δt containing $N_{\text{pulses}} = r\Delta t$ pulses, the average number of expected coincident events, consistent with Bernoulli statistics, is calculated as follows:

$$N_{\text{acc}} = N_{pulses} p_{\text{coinc}}^{(pulse)} = \frac{R_A R_B}{r} \Delta t \tag{D.6}$$

Finally, by dividing N_{acc} by Δt, we obtain the rate of accidental coincidences in pulse mode:

$$R_{\text{acc}}^{(pulse)} = \frac{R_A R_B}{r} \tag{D.7}$$

Bibliography

[1] A. Einstein, B. Podolsky and N. Rosen, *Can Quantum-Mechanical Description of Physical Reality Be Considered Complete?*, Phys. Rev., vol. 47, no. 10, pp. 777—780 (1935).

[2] J. S. Bell, *On the Einstein Podolsky Rosen paradox*, Physics Physique Fizika 1, 195 (1964).

[3] S. J. Freedman and J. F. Clauser, *Experimental Test of Local Hidden-Variable Theories*, Phys. Rev. Lett. 28, 938 (1972).

[4] A. Aspect, J. Dalibard, and G. Roger, *Experimental Test of Bell's Inequalities Using Time-Varying Analyzers*, Phys. Rev. Lett. 49, 1804 (1982).

[5] W. Rojpattanakul et al., *Simple experimental setup for producing polarization-entangled photons* , J. Phys. Conf. Ser. 1380 012023 (2019).

[6] A. S. Solntsev, A. A. Sukhorukov, *Path-entangled photon sources on nonlinear chips*, Rev. in Phys. Volume 2, pp. 19-31 (2017).

[7] S. Dong, Q. Zhou, W. Zhang, Y. He, W. Zhang, L. You, Y. Huang, and J. Peng, *Energy-time entanglement generation in optical fibers under CW pumping*, Vol. 22, Issue 1, pp. 359-368 (2014).

[8] B. Sangshekan, M. Sahrai, S.H. Asadpour et al., *Controllable atom-photon entanglement via quantum interference near plasmonic nanostructure*, Sci. Rep. 12, 677 (2022).

[9] V. Scarani, H. Bechmann-Pasquinucci, N. J. Cerf, M. Dusek, N. Lutkenhaus, and M. Peev, *The security of practical quantum key distribution*, Rev. Mod. Phys. 81, 1301 (2009).

[10] S. Pirandola, U. L. Andersen, L. Banchi, M. Berta, D. Bunandar, R. Colbeck, D. Englund, T. Gehring, 13 C. Lupo, C. Ottaviani, et al., *Advances in quantum cryptography*, Advances in optics and photonics 12, 1012 (2020).

[11] T. Jennewein, C. Simon, G. Weihs, H. Weinfurter, and A. Zeilinger, *Quantum Cryptography with Entangled Photons*, Phys. Rev. Lett. 84, 4729 (2000).

[12] D. Bouwmeester, J.-W. Pan, K. Mattle, M. Eibl, H. Weinfurter, and A. Zeilinger, *Experimental quantum teleportation*, Nature 390, 575 (1997).

[13] J. L. O'brien, *Optical quantum computing*, Science 318, 1567 (2007).

[14] M. A. Broome, A. Fedrizzi, S. Rahimi-Keshari, J. Dove, S. Aaronson, T. C. Ralph, and A. G. White, *Photonic boson sampling in a tunable circuit*, Science 339, 794 (2013).

[15] C. Lindner, Jachin Kunz, Simon J. Herr, J. Kießling, S. Wolf, F. Kühnemann, *High-sensitivity quantum sensing with pump-enhanced spontaneous parametric down-conversion*, APL Photonics 8, 051301 (2023)

[16] P. A. M. Dirac, *The principles of quantum mechanics*, 4th ed. Oxford (1930).

[17] M. A. Nielsen and I. L. Chuang, *Quantum Computation and Quantum Information*, Cambridge University Press (2010).

[18] U. Leonhardt, *Measuring the Quantum State of Light*, Cambridge University press (1997).

[19] E. Schrödinger, *Quantisierung als Eigenwertproblem*, Annalen der Physik 81 p. 734 (1926).

[20] K. Kraus, A. Böhm, J. D. Dollard, W. H. Wootters, *States, Effects, and Operations Fundamental Notions of Quantum Theory*, volume 190 of Lecture Notes in Physics, Springer (1983).

[21] A. Vianello, *Componentlibrary*, the reference figure has been made using this library.

[22] J. F. Clauser, M. A. Horne, A. Shimony, and R. A. Holt, *Proposed Experiment to Test Local Hidden-Variable Theories*Phys. Rev. Lett. 23, 880 (1969).

[23] N. Brunner, D. Cavalcanti, S. Pironio, V. Scarani, and S. Wehner, *Bell nonlocality*, Rev. Mod. Phys. 86, 839 (2014).

[24] B. S. Cirel'son, *Quantum generalizations of Bell's inequality*, Lett Math Phys 4, 93–100 (1980).

[25] I. Šupić and J. Bowles, *Self-testing of quantum systems: a review*, Quantum 4, 337 (2020).

[26] A. Anwar, C. Perumangatt, F. Steinlechner, et al., *Entangled photon-pair sources based on three-wave mixing in bulk crystals*, Rev. Sci. Instrum. 92, 041101 (2021).

[27] O. Gühne and G. Tóth, *Entanglement detection*, Phys. Rep. 474, 1 (2009).

[28] T. Jennewein, R. Ursin, M. Aspelmeyer, and A. Zeilinger, *Performing high-quality multi-photon experiments with parametric down-conversion*, J. Phys. B: At., Mol. Opt. Phys. 42, 114008 (2009).

[29] F. Steinlechner, S. Ecker, M. Fink, B. Liu, J. Bavaresco, M. Huber, T. Scheidl, and R. Ursin, *Distribution of high-dimensional entanglement via an intra-city free-space link*, Nat Commun 8, 15971 (2017).

[30] S. A. Hill and W. K. Wootters, *Entanglement of a Pair of Quantum Bits* , Phys. Rev. Lett. 78, 5022 (1997).

[31] D. F. V. James, P. G. Kwiat, W. J. Munro, and A. G. White, *Measurement of qubits*, Phys. Rev. A, vol. 64, art. 052312, (2001).

[32] J. D. Jackson, *Classical Electrodynamics 3rd Ed.*, New York: J. Wiley and Sons (1999).

[33] R. W. Boyd, *Nonlinear Optics (Fourth Edition)*, Academic Press, Elsevier (2020).

[34] B. E. A. Saleh and M. C. Teich, *Fundamentals of Photonics*, Wiley (2007).

[35] M. Born and L. Infeld, *On the quantization of the new field equations I*, Proc. R. Soc. London, Ser. A 147, 522 (1934).

[36] N. Quesada and J. E. Sipe, *Why you should not use the electric field to quantize in nonlinear optics*, Opt. Lett. 42, 3443 (2017).

[37] R. J. Glauber, *The Quantum Theory of Optical Coherence*, Phys. Rev. 130, 2529 (1963).

[38] S. Karan, S. Aarav, H. Bharadhwaj, L. Taneja, A. De, G. Kulkarni, N. Meher, and A. K. Jha, *Phase matching in β-barium borate crystals for spontaneous parametric down-conversion*, Journal of Optics 22, 083501 (2020).

[39] R. S. Bennink, *Optimal collinear gaussian beams for spontaneous parametric down-conversion*, Phys. Rev. A 81, 053805 (2010).

[40] J. Schneeloch, S. H. Knarr, D. F. Bogorin, M. L. Levangie, C. C. Tison, R. Frank, G. A. Howland, M. L. Fanto, and P. M. Alsing, *Introduction to the absolute brightness and number statistics in spontaneous parametric down-conversion*, Journal of Optics 21, 043501 (2019).

[41] J. E. Midwinter and J. Warner, *The effects of phase matching method and of uniaxial crystal symmetry on the polar distribution of second-order non-linear optical polarization*, Br. J. Appl. Phys. 16 1135 (1965).

[42] P. Kolenderski, W. Wasilewski, and K. Banaszek, *Modeling and optimization of photon pair sources based on spontaneous parametric down-conversion*, Phys. Rev. A 80, 013811 (2009).

[43] G. Vallone, *Role of beam waist in Laguerre–Gauss expansion of vortex beams*, Opt. Lett. 42, 1097 (2017).

[44] C.Y. Lu, X. Q. Zhou, O. Gühne et al., *Experimental entanglement of six photons in graph states*, Nature Phys. 3, 91–95 (2007).

[45] C. K. Hong, Z. Y. Ou, L. Mandel, *Measurement of subpicosecond time intervals between two photons by interference*, Phys. Rev. Lett. 59, 2044 (1987).

[46] M. Michler, K. Mattle, H. Weinfurter, and A. Zeilinger, *Interferometric Bell-state analysis*, Phys. Rev. A 53, R1209(R) (1996).

[47] C. K. Law, I. A. Walmsley, and J. H. Eberly, *Continuous Frequency Entanglement: Effective Finite Hilbert Space and Entropy Control*, Phys. Rev. Lett. 84, 5304 (2000).

[48] W. E. Lamb Jr, *Theory of an optical maser*, Phys. Rev. 134, A1429 (1964).

[49] J. Lein,*Spectral linewidth and coherence*, Master's thesis in physics, University of Oslo (2010).

[50] T. Brabec, Ch. Spielmann, P. F. Curley, and F. Krausz, *Kerr lens mode locking*, Opt. Lett. 17, 1292-1294 (1992).

[51] D. Marcuse, *Loss analysis of single-mode fiber splices*, The Bell System Technical Journal, vol. 56, no. 5, pp. 703-718, (1977).

[52] G. N. Gol'tsman, O. Okunev, G. Chulkova, A. Lipatov, A. Semenov, K. Smirnov, B. Voronov, A. Dzardanov, C. Williams and R. Sobolewski *Picosecond superconducting single-photon optical detector*, Appl. Phys. Lett. 79 705-707 (2001).

[53] A. D. Semenov, G. N. Gol'tsman, and A. A. Korneev, *Quantum detection by current carrying superconducting film*, Physica C 351 349-56 (2001).

[54] J. K. W. Yang, A. J. Kerman, E. A. Dauler, V. Anant, K. M. Rosfjord, and K. K. Berggren, *Modeling the electrical and thermal response of superconducting nanowire single-photon detectors*, IEEE T. Appl. Supercon. 17 581-5 (2007).

[55] C. M. Natarajan, M. G. Tanner, R. H. Hadfield, *Superconducting nanowire single-photon detectors: Physics and applications*, Supercond. Sci. Technol. 25 063001 (2012).

[56] J. A. Armstrong, N. Bloembergen, J. Ducuing, and P. S. Pershan, *Interactions between Light Waves in a Nonlinear Dielectric*, Phys. Rev. 127, 1918 (1962).

[57] M. Yamada, N. Nada, M. Saitoh, and K. Watanabe, *First-order quasi-phase matched LiNbO3 waveguide periodically poled by applying an external field for efficient blue second-harmonic generation*, Appl. Phys. Lett. 62, 435 (1993).

[58] K. Fradkin, A. Arie, A. Skliar, G. Rosenman, *Tunable midinfrared source by difference frequency generation in bulk periodically poled $KTiOPO_4$*, Appl. Phys. Lett., 74, 914–916 (1999).

[59] F. König, F. N. C. Wong, *Extended phase matching of second-harmonic generation in periodically poled $KTiOPO_4$ with zero group-velocity mismatch*, Appl. Phys. Lett., 84, 1644–1646 (2004).

[60] S. Emanueli and A. Arie, *Temperature-dependent dispersion equations for $KTiOPO_4$ and $KTiOAsO_4$*, Appl. Opt. 42, 6661-6665 (2003).

[61] A. Franzen, *Componentlibrary*, Albert Einstein Institution, Hannover, Germany, (2006). This figure and many others throughout the thesis use ComponentLibrary to draw optical components.

[62] T. Kim, M. Fiorentino, and F. N. C. Wong, *Phase-stable source of polarization-entangled photons using a polarization Sagnac interferometer*, Phys. Rev. A, 73, 012316 (2006).

[63] P. G. Kwiat, E. Waks, A. G. White, I. Appelbaum, and P. H. Eberhard, *Ultrabright source of polarization-entangled photons*, Phys. Rev. A 60, R773(R) (1999).

[64] G. H. Wagnière, S. Woźniak, *Nonlinear Optical Properties*, Encyclopedia of Spectroscopy and Spectrometry (Third Edition), Academic Press, p. 375-387 (2017).

[65] A. Aspect, Philippe Grangier, and Gérard Roger, *Experimental Realization of Einstein-Podolsky-Rosen-Bohm Gedankenexperiment: A New Violation of Bell's Inequalities*, Phys. Rev. Lett. 49, 91 (1982).

Acknowledgments

Desidero esprimere un sincero ringraziamento a Giulio Foletto, Lorenzo Coccia e Matteo Padovan, non solo per il loro fondamentale sostegno durante l'intero progetto, ma anche per la loro eccezionale disponibilità dimostrata in ogni occasione, persino durante le ferie estive.

Ringrazio il Professore Giuseppe Vallone per avermi concesso l'opportunità di svolgere questo lavoro di tesi e per tutti i preziosi consigli che hanno contribuito in modo determinante alla mia crescita personale, ma anche, e soprattutto, per avermi fatto scoprire e appassionare al mondo delle comunicazioni quantistiche.

Desidero esprimere inoltre il mio ringraziamento a tutto il gruppo QuantumFuture, che mi ha accolto calorosamente e ha condiviso preziose conoscenze e consigli.

Infine, vorrei dedicare un ringraziamento speciale alla mia famiglia, che in tutti questi anni di studio mi ha sostenuto e ha sempre creduto in me.